TURRET OPTIMIZATION USING PASSIVE FLOW CONTROL TO MINIMIZE AERO-OPTIC EFFECTS

A Dissertation

Submitted to the Graduate School

of the University of Notre Dame

in Partial Fulfillment of the Requirements

for the Degree of

Doctor of Philosophy

by

Grady C. Crahan

_____

Dr. R. Mark Rennie, Co-Director

_____

Dr. Eric Jumper, Co-Director

Graduate Program in Aerospace and Mechanical Engineering

Notre Dame, Indiana

April 2014

TURRET OPTIMIZATION USING PASSIVE FLOW CONTROL TO MINIMIZE AERO-OPTIC EFFECTS

Abstract

by

Grady C. Crahan

Over the past several decades, optical systems have begun to be deployed regularly on aircraft that fly at compressible flow speeds. During this time, these optical systems have also moved towards shorter operating wavelengths that can deliver a higher peak irradiance in the focused spot on a distant target, and the assumption is that future systems will use even shorter-wavelength lasers.

As this trend towards short-wavelength systems continues, the need to take into account the effect of flow-induced, or “aero-optic,” aberrations that occur in the vicinity of the parent aircraft has become progressively more important. The conventional method for mounting an optical system is to place it in a hemispherical turret; however, from an aero-optic standpoint, there are two problems with this mounting arrangement. First, shocks begin to form on the surface of a sphere (or hemisphere) at a critical Mach number of only around 0.55. Furthermore, a shear layer is produced due

to flow separation on the aft side of the sphere; both of these flows, shocks and separated shear layers, involve strong index-of-refraction variations in the flow that would severely aberrate the outgoing beam.

One approach to the problem would be to employ adaptive-optic (AO) methods in which the conjugate of the aberration is applied to the outgoing beam before it transmits through the aero-optic flow; however, state-of-the-art AO systems are generally unable to match the high temporal frequencies associated with aero-optic flows. As such, there is a need for innovative mounting strategies for optical systems that avoid or mitigate the formation of optically-aberrating flows in the first place.

This dissertation outlines an investigation into aerodynamic shaping of turrets to mitigate the aero-optic aberrations produced by shock waves and shear layers. Specifically, a computational and experimental investigation into the "virtual duct" concept, which is a passive flow-control approach to mitigating aero-optic effects on spherical turrets, is described. The aerodynamic features associated with the problem are investigated, and the performance of different turret configurations as a function of the design parameters is explored. By the use of optimization techniques along with experimental validation, it is shown that significant increases of delaying flow separations up to an elevation angle of 162.4° while maintaining a critical Mach number over 0.7 can be attained on a hemispherical turret without a downstream fairing. The investigation shows that the virtual duct technique is an effective passive flow-control approach for dealing with aero-optic flows on spherical turrets in subsonic to transonic flows.

CONTENTS

Figures v

Acknowledgments xii

Nomenclature xiii

Chapter 1: Introduction 1
1.1 Introductory Comments 1
1.2 Advantages and Disadvantages of Spherical Turrets 7
1.2.1 Critical Mach Number Issues 9
1.2.2 Flow Separation 13
1.2.2.1 Shear Layers 14
1.2.2.2 Adaptive-Optic Corrections 16
1.3 Summary of Spherical Turret Performance 20

Chapter 2: A Passive Approach to The Mitigation of Aero-Optic Flows 21
2.1 Introduction 21
2.2 Underwing Pod 21
2.2.1 Fairing Work 22
2.2.2 Virtual Duct Concept 25
2.2.3 Experimental Validation of the Virtual Duct Approach 29
2.3 Concluding Remarks 37

Chapter 3: The Canonical Turret with Virtual Duct 39
3.1 Introduction 39
3.2 Experiments on Canonical Hemisphere-on-Cylinder Turret 40
3.3 Experimental Investigation of Virtual Duct on Hemisphere-on-Cylinder Turret 43
3.3.1 Virtual Duct with Low Curvature 44
3.3.2 Virtual Ducts with Medium and High Curvature 47
3.4 Tuft Study 51
3.5 CFD Computations of Virtual Duct on Hemisphere-on-Cylinder Turret 52
3.5.1 Hemisphere-on-Cylinder Turret 53
3.5.2 CFD Study of Low-Curvature Virtual Duct 54
3.6 Concluding Remarks 56

Chapter 4: Secondary Flow Effects in the Virtual Duct 58

4.1 Introduction 58
4.2 Particle Image Velocimetry (PIV) Study 59
4.3 Curved Open-Channel Flow 62
4.3.1 Implications to Virtual-Duct Performance and Organization of this Chapter 63
4.4 Validation of Computational Approach 66
4.4.1 DES Modeling of PIV Experiment 68
4.5 DES Modeling of Virtual Duct 69
4.6 Scaling of Corner Vortex Parameters 75
4.6.1 Open-Channel Flow Studies 75
4.6.2 Testing of Open-Channel Scaling Approach 77
4.7 Estimation of Aero-Optic Effect of Corner Vortices 81
4.8 Conclusions 94

Chapter 5: Geometry Optimization 95
5.1 Design of Experiments 96
5.1.1 DoE Analysis of Fairing 98
5.2 Development of Fast Solution Methodology for Virtual Duct 104
5.2.1 Stratford Criterion for Prediction of Boundary-Layer Separation 107
5.2.2 Example of Stratford Criterion Applied to Virtual Duct 108
5.3 DoE Analysis of Virtual Duct 110
5.4 Optimization Methods 114
5.4.1 Optimization Approach Used in this Research, and Cases Investigated 115
5.5 Fairing Optimization 116
5.6 Virtual Duct Optimization 122
5.7 Conclusions 129

Chapter 6: Summary and Recommendations 131

Appendix A: Experimental Corrections 135
A.1 Blockage Correction 135
A.2 Pressure Calibration 137
A.3 95% Confidence Intervals 140

Appendix B: Overview of Optimization 141
B.1 Variable-Fidelity Optimization 144
B.2 Sequential Quadratic Programming Code 145

Appendix C: Preliminary Study of Virtual Duct 149
C.1 Investigation of the Design Space 149
C.2 Design Variables 150
C.3 Constraints 151
C.4 Methodology for Design Optimization 152

C.5 Survey of Design Space 153
C.6 Summary of Preliminary Study of Design Space 155

Bibliography 156

FIGURES

Figure 1.1. Maximum irradiance on target relative to the maximum irradiance of the CO_2 laser plotted against the wavelength of the laser (Jumper 2001). 2

Figure 1.2. Strehl Ratio as a function of wavelength for a constant OPD_{RMS} that would produce a Strehl ratio of 0.95 on a CO_2 Laser. These same aberrations would produce a Strehl Ratio of 0.04 on a COIL (Jumper 2001). 6

Figure 1.3. The beam direction defined by the elevation angle (α) and azimuthal angle (β) (Porter 2011a). 7

Figure 1.4. In order for the internal reflection of the beam to not destroy the internal optics, a beam dump needs to be placed inside the turret to absorb the reflection of the beam. 8

Figure 1.5: Critical Mach number for a turret using the Karmen-Tsien compressibility correction formula. 10

Figure 1.6. OPD_{RMS} for bands of modified elevation angles at transonic Mach numbers (De Lucca 2012).....11

Figure 1.7. Experimental pressure distributions over a turret compared to the potential solution over a sphere (Gordeyev 2010).....12

Figure 1.8. Oil Flow Visualization of a turret showing the location of separation, Re_D = 650,000. The line represents an elevation angle of 120°. 13

Figure 1.9. Schematic of subsonic flow around a turret (Gordeyev 2010). 14

Figure 1.10. Basic components of an adaptive-optics system (Tyson 2000).....16

Figure 1.11. Adaptive-optic system requirement estimation of aero-optic effects (Duffin 2009). 18

Figure 2.1. Examples of pod or fairing shapes that increase the critical Mach number on the turret ball to $M\infty$ = 0.8 (Rennie 2010).....22

Figure 2.2. CFD-computed pressure distributions for basic pod shapes shown in Figure 2.1 (Rennie 2010). 23

Figure 2.3. Basic aero-optic pod layout based on the "cubic-forebody" shape, including a basic cutout to enable a greater range of lookback angles (Rennie 2010). 24

Figure 2.4. Illustration showing how straight cutout walls constrain streamlines on the turret ball (Rennie 2010). 25

Figure 2.5. Pod with improved cutout and fence (i.e., "virtual duct") installed to control flow around aperture (Rennie 2010). 26

Figure 2.6. CFD-computed pressure distributions around the turret ball and critical Mach numbers for different cutout configurations. "Straight" and "improved" cutout configurations are designed for a maximum lookback angle of 20° (Rennie 2010). 28

Figure 2.7. Picture of experimental model showing (top) the pressure taps along the centerline of the model and (bottom) how the model looks in the wind tunnel (Crahan 2011). 29

Figure 2.8. Side view of the centerline of the pod for lookback angles of 20°, 40°, and 60° (Crahan 2011). 30

Figure 2.9. Experimentally and computationally-determined pressure distributions for pod model with 20° lookback angle for a high (left) fence height and a regular (right) fence height (Crahan 2011). 31

Figure 2.10. Experimentally and computationally-determined pressure distributions for pod model with 40° lookback angle for a high (left) fence height and a regular (right) fence height (Crahan 2011). 32

Figure 2.11. Experimentally and computationally-determined pressure distributions for pod model with 60° lookback angle and high (left) fence height and a regular (right) fence height (Crahan 2011). 33

Figure 2.12. Oil flow visualization for flow over the pod. 36

Figure 3.1. Isometric picture of a canonical hemisphere-on-cylinder turret with a virtual duct. 39

Figure 3.2. Comparison of pressure distribution found experimentally for flow over a 12 inch diameter turret. 40

Figure 3.3. Oil-flow visualization on the canonical hemisphere-on-cylindrical-base turret model, Re_D = 6.8 x 10^5. The superposed vertical line shows the location of an elevation angle of 120°. 41

Figure 3.4. C_P distribution for hemisphere-on-cylinder turret with top (upper) and side (lower) views. These computational results are for a diameter of .3048 m (12 in) and Re_D of 23.0 x 10^5 (Ladd 2009). 43

Figure 3.5. Flow through low-curvature virtual duct showing attachment up to an elevation angle of 150°. 45

Figure 3.6. Pressure distribution for flow through the low-curvature virtual duct configuration shown in Figure 3.5, compared to a turret without a fence. 46

Figure 3.7. Medium-curvature virtual duct configuration. 48

Figure 3.8. High-curvature virtual duct configuration. 48

Figure 3.9. Pressure distribution for flow through the medium-curvature virtual duct configuration shown in Figure 3.7, compared to a turret without a fence. 49

Figure 3.10. Picture of tufts attached to turret from the top (left) and a close up side view of the last row of tufts (right), flow is from left to right. 50

Figure 3.11. Comparison of DES CFD (solid line) and experimental (diamonds) pressure distribution for flow over a hemisphere-on-cylinder turret. 52

Figure 3.12. Magnitude of skin friction for for flow over a hemisphere-on-cylinder turret computed using the DES solver showing flow separation around an elevation angle of 120°. 53

Figure 3.13. Experimental pressure distribution (circles) compared to a DES of the same geometry (dotted line) for the low-curvature fence. 55

Figure 3.14. Skin friction on the surface of the low-curvature virtual duct found using CFD. 57

Figure 4.1. Photograph of wind-tunnel model used in PIV tests. Flow is from left to right.58

Figure 4.2. Set-up of PIV configuration to experimentally measure the secondary vortex.59

Figure 4.3. Velocity vectors on the fence found using PIV. 60

Figure 4.4. Comparison of the velocity profile through the vortex core from the bottom of the wall for the CFD and PIV data. 61

Figure 4.5. Aerial view of the Charley River at Yukon, Alaska. Credits to Tim Brabets, U.S. Geological Survey (Van Balen 2010). 62

Figure 4.6. General Schematic of flow through a curved channel (Van Balen 2010) 64

Figure 4.7. Comparison of measured (black circles), RANS- (dashed blue line), DES- (red line), and LES-computed (solid black line) velocity profiles of the non-dimensional transverse velocity in an open-channel flow. The outer wall is on the right (Constantinescu 2011). 66

Figure 4.8.(Left) CFD run of PIV set-up showing the formation of the vortex near the wall of the fence. (Right) Comparison of the velocity profile through the vortex core from the bottom of the wall for the CFD and PIV data. 68

Figure 4.9. Virtual duct wall shapes computed using DES. The wall radii are, from left to right, 0.099, 0.120, and 0.166 meters. 70

Figure 4.10. Isometric (left) and plan (right) view of turret with flow in positive x-direction. The fence is defined by 3 points. 70

Figure 4.11. DES-computed crossplane pressure distribution inside virtual ducts with R = 0.099 (top left), R = 0.120 (top right) and R = 0.166 (bottom) m. Note that the highest curvature duct (top left) produces the strongest vortex core with the lowest pressure. Note the change in legend values for the bottom figure. 71

Figure 4.12. Two-dimensional flowfield around a cylindrical core rotating as a rigid body (Katz 1991). 72

Figure 4.13. Left, Tangential velocity through vortex core on a virtual duct for varying curvature ratios. Right, Tangential velocity through vortex core for smallest curvature ratio showing the core diameter. 73

Figure 4.14. DES solutions for the circulation (left) and core radius (right) of corner vortices for flow over a turret with different virtual-duct radii. 74

Figure 4.15. View of mesh and geometry of the curved channel studied in Kashyap (2012). This configuration has is an R/B of 1.5. 76

Figure 4.16. Comparison of 2D streamline patterns (left) and streamwise velocity, u/U, (right) at the 135° cross section. 77

Figure 4.17. Variation of nondimensional gamma with curvature ratio for water flow in a curved channel (Kashyap, 2012). 78

Figure 4.18. Nondimensional Gamma as a function of curvature ratio for flow through a virtual duct on a hemispherical turret (Left) and a planar floor (Right). 79

Figure 4.19. All circulation data from Kashyap (2012) and the virtual duct study. 80

Figure 4.20. Core radius as a function of the Curvature ratio for the vortex inside of a virtual duct.....81

Figure 4.21. Density as a function of distance from the core center.....83

Figure 4.22. Schematic of beam passing between virtual duct fences. The 2 vortices are located at the corner between the hemisphereical turret and the virtual duct fences. (Right) An unaberrated outgoing beam (bottom) will have an aberrated wavefront (top) after encountering the vortices. 84

Figure 4.23. Non-dimensional density, left, and resulting OPD, right, inside half of the virtual duct, the other half is mirrored across the x = 0 axis. This case is for a curvature ratio, R/B, of 1.88 at $M\infty$ = 0.5. 86

Figure 4.24. The farfield effect of the OPD distribution in Figure 4.23, computed using the Fraunhofer approximation, λ = 1 μm. 87

Figure 4.25. Strehl Ratio as a function of the curvature ratio and freestream Mach number. 88

Figure 4.26. OPD, left, and farfield irradiance, right, for different curvature ratios at $M\infty$= 0.8. Look at Figure 4.25 showing the local minimum and maximum of SR plotted. Curvature ratios, R/B, are a) 2.1, b) 1.5, c) 1.04, d) 0.89, e) 0.74, f) 0.62, g) 0.58, and h) 0.53. Figure on pages 89-91. 89

Figure 4.27 Strehl Ratio vs OPD_{rms} showing the instability in using the Large Aperture Approximation at larger OPD_{rms} values (Gordeyev 2014).....93

Figure 5.1. Aft fairing defined by 4 points to be studied. 98

Figure 5.2. Isometric (left) and plan (right) view of turret with flow in positive x-direction. The fence is defined by 3 points that are adjusted to find the optimum shape to minimize the objective function.....104

Figure 5.3. Pressure distributions of the Euler solution for flow through the virtual ducts shown in Figure 5.4. 105

Figure 5.4. Virtual duct wall shapes computed in Figure 5.3. The curvature ratios are, from left to right, 0.902, 1.26, and 1.88.....107

Figure 5.5. Stratford's criterion applied to the lowest-curvature, R/B = 1.88, pressure distributions shown in Figure 5.3. 108

Figure 5.6. Comparison of 1st guess fairing shape to the optimal solution. 118

Figure 5.7 Critical Mach number for each function call (left) and iteration (right) for the fairing optimization. The optimal solution, found on function call 35 and iteration 7, is denoted by the diamond. 120

Figure 5.8. Pressure distribution over the front portion of the turret with fairing (left) and over the full fairing (right). 121

Figure 5.9. The location of separation for each function call (left) and iteration (right) for the virtual duct optimization. The optimal solution is found on function call 27 and iteration 5. 123

Figure 5.10. Virtual duct shape for the 1st and last iteration. 126

Figure 5.11. The pressure distribution inside of the virtual duct for the initial guess and the optimized fence. 127

Figure 5.12. Strehl Ratio as function of Mach number for the curvature ratio, 1.22, of the optimized virtual duct shape. 128

Figure A.1. Pressure distribution for 20° lookback angle with a regular fence height showing that the blockage correction converges to a similar solution for both wind tunnels (Crahan 2011). 136

Figure A.2. Overview of pressure measurement based on the pressure taps on the model and the pressure values measured with a pitot static probe. 137

Figure A.3. Data in Figure 3.6 showing the 95% confidence intervals. 139

Figure B.1. Variable fidelity framework flowchart (Gano 2004). 143

Figure C.1. Side view of turret showing lookback angle of 40° (Crahan 2010). 150

Figure C.2. Flow chart showing the optimization function call (Crahan 2010). 152

Figure C.3. Contour plots of the pressure gradient for different fence shapes on a turret by changing (a) x_1 and y_1, (b) x_2 and y_2, or (c) x_3 and y_3 with the unchanging fence points (x_1, y_1, x_2, y_2, x_3, y_3) being set at (0.25, 0.25, 0.5, 0.31, 0.85, 0.17). The region donated with the roman numeral "I" is the region of the design space where the minimum critical mach number is greater than 0.7 (Crahan 2010). . 154

TABLES

TABLE 1 SUMMARY OF EFFECT OF A COMPRESSIBLE M=0.78/0.12 SHEAR LAYER ON THE STREHL RATIO OF A 1 μM SYSTEM. 15

TABLE 2 CRITICAL MACH NUMBER FOR DIFFERENT LOOKBACK ANGLES AT DIFFERENT FENCE HEIGHTS BASED ON EXPERIMENTAL DATA (CRAHAN 2011). 34

TABLE 3 VALUES FOR EACH VARIABLE USED IN THE DOE SCREENING STUDY FOR THE FAIRING, D REPRESENTS THE DIAMETER OF THE TURRET. 100

TABLE 4 RELATIVE EFFECT OF EACH PARAMETER OR COMBINATION OF PARAMETERS ON MCRIT, COMPUTED USING DESIGN OF EXPERIMENTS APPROACH. 102

TABLE 5 VARIABLES CHOSEN FOR EACH DOE RUN ALONG WITH THE CURVATURE RATIO, R/B. THE HIGHER VALUE FOR THE VARIABLE IS HIGHLIGHTED GREY. 111

TABLE 6 DESIGN OF EXPERIMENTS FOR FAIRING, COMPARING THE DIFFERENCE BETWEEN THE HIGH AND LOW VALUES OF EACH PARAMETER BASED ON THE SEPARATION LOCATION. 114

ACKNOWLEDGMENTS

I would like to thank my advisors, Dr. Mark Rennie and Dr. Eric Jumper, with whom this work would not have been possible, my fellow Hessert graduate students, who helped me set-up experiments and gave me ideas to improve this project, and my wife, and parents who have constantly motivated me to pursue my dreams. I would also like to thank the Office of Naval Research (Award Number N00014-07-1-0291) which allowed me to pursue my work.

NOMENCLATURE

a	Speed of Sound
a,b,c,d,e,f	Arbitrary Constants
A_D	Aperture Diameter
B	Width of Bend or Virtual Duct
C_P	Pressure Coefficient
C_P'	Canonical Pressure Coefficient
C_{P0}	Incompressible Pressure Coefficient
d	Aperture Diameter, Search Direction
ds	Differential Length
D	Hemisphere Diameter
f_d	Frequency of Aero-optic Disturbance
f_u	Update Frequency
h	Fence Height
I	Farfield Irradiance
I_0	Maximum Irradiance
K	Number of Variables, Iteration Number
K_{GD}	Gladstone-Dale Constant
L	Length of Ellipsoid Forebody Long Axis
M	Mach Number
n	Index of Refraction
OPD	Optical Path Difference
OPL	Optical Path Length
P	Laser Power Output
r	Radial Component of Fairing Forebody, Radius, Distance from Center of Vortex
P	Static Pressure
r, θ, z	Cylindrical Coordinates
R	Radius of Curvature, Gas Constant
R/B	Curvature Ratio
Re	Reynolds Number
SR	Strehl Ratio
t	Time
T	Static Temperature
V	Velocity

V_r	Radial Velocity
V_z	Axial Velocity
V_θ	Tangential Velocity
x, y, z	Cartesian Coordinates
x′,y′	Nearfield Coordinates
Y	Focal Length of Optical System

Greek

α	Elevation Angle, Step Size, Lamb-Oseen Constant (1.25643), arbitrary calibration constant
α_0	Elevation Angle when Stratford Criterion is > 1
β	Azimuthal Angle, Controller Gain, DoE Influence Parameter, arbitrary calibration constant
γ	Specific Heat Ratio (air = 1.4)
Γ	Circulation
Γ^*	Non-dimensional Circulation
λ	Wavelength
ρ	Density
σ_ϕ^2	Time Averaged Optical-Phase Variance
τ_2	Computer-related Latency

Subscripts

c	Contraction Section of Virtual Duct, Blockage Corrected, Core
corrected	Disturbance corrected using an adaptive-optic system
crit	Critical
d	Diffusion Section of Virtual Duct
hi	High Fence Height
m	Measured
min	Minimum
model	Model
reg	Regular Fence Height
RMS	Root Mean Square
SL	Sea Level
ts	Test Section
uncorrected	Disturbance not corrected using an adaptive-optic system
∞	Freestream

CHAPTER 1:

INTRODUCTION

1.1 Introductory Comments

A significant amount of research is now being devoted to the problem of mounting optical systems on high-speed aircraft (De Lucca 2012, Gordeyev 2012). These systems could be used for a variety of applications such as optical communications (Gordeyev 2011, Smith 2013), imaging, or other uses (Duffner 1997, Forden 1997).

A review of the types of lasers that have been evaluated or could be employed in future aircraft-mounted optical systems is given by Carroll (2011). Starting in the late 1960s, investigators considered primarily the CO_2 laser, which was the highest-power laser available at the time. A serious problem with the CO_2 laser, however is that it has a relatively long wavelength in the far infrared, that is λ = 10.6 μm. In particular, the maximum irradiance at the focal point of a focused, unaberrated beam is limited by diffraction effects; for a beam projected from a circular aperture with diameter *d*, this peak irradiance is given by:

$$I_0 = \frac{Pd^2}{\pi Y^2 \lambda^2}, \tag{1.1}$$

where *P* is the laser output power and *Y* is the focal length of the optical system. Equation (1.1) shows that the on-target irradiance of the beam varies as the inverse of

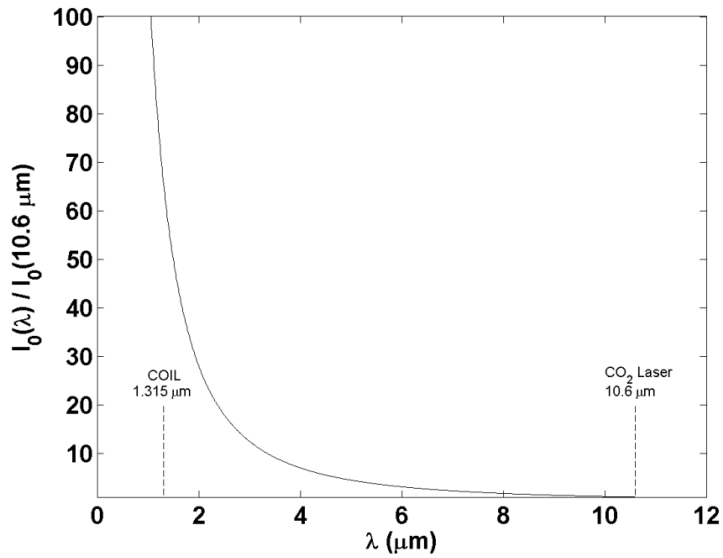

Figure 1.1. Maximum irradiance on target relative to the maximum irradiance of the CO_2 laser plotted against the wavelength of the laser (Jumper 2001).

the wavelength squared. This means that, for example, an optical system with the same power as a CO_2 laser but with an output wavelength of 1 μm would have over 100 times the peak irradiance on target. This result clearly shows the significant improvement in on-target irradiance that can be obtained by using systems with shorter wavelengths. Figure 1.1 shows how the peak, on-target diffraction-limited irradiance of an optical system varies with the system wavelength, nondimensionalized by the diffraction-limited irradiance achievable at 10.6 μm.

The trend to shorter-wavelength lasers raises, however, other operational problems. In particular, the ability to focus on distant targets in the farfield is also degraded by any optical aberrations that exist in the beam path between the point where the laser is emitted and the target. As discussed in Siegenthaler (2008), one

source of these intervening optical aberrations originates from atmospheric flows where the optical aberrations arise primarily from temperature variations in the atmosphere; however, these variations are typically associated with large-scale atmospheric structures and therefore have a comparatively low frequency that is correctable using adaptive-optic (AO) approaches (AO systems and the mechanisms by which optical aberrations are produced are discussed in further detail later in this chapter). On the other hand, optical aberrations can also originate from nearfield optically-aberrating flows that are produced by the aircraft on which the optical system is mounted. Examples of these kinds of nearfield aberrating flows include boundary layers (Buckner 2005, Gordeyev 2003), shear layers (Duffin 2009, Fitzgerald 2004, Hugo 1997, Rennie 2008), and even shock waves (De Lucca 2012, Rennie 2010). These nearfield compressible flows pose more of a problem to airborne optical-system designers due to the much higher-frequency and often larger-amplitude optical aberrations that they produce. The study of the aberrating effect of nearfield compressible flows is called "aero-optics," and dealing with aero-optic flows is the primary concern of this investigation.

If the magnitude and spatial variation of the intervening optical aberration is known, then the farfield irradiance pattern at the target can be computed (Klein 1970) using the Fraunhofer approximation:

$$I(x,y) = \left(\frac{1}{\lambda z}\right)^2 \left(\iint_{-\infty}^{\infty} e^{-i\frac{2\pi}{\lambda}(-OPD)} e^{-i\frac{2\pi}{\lambda z}(xx'+yy')} dx'dy' \right)^2 . \qquad (1.2)$$

Once the farfield irradiance pattern is known, a single-parameter representation of the effectiveness of the optical system, called the Strehl Ratio, *SR*, can be determined:

$$\overline{SR} = \frac{\bar{I}}{I_0}, \tag{1.3}$$

where $\bar{I}$ is the time average of the light irradiance at the target point in the farfield for the aberrated system, and I_0 is the optimum, diffraction-limited irradiance that could be attained on target for a system that had no aberrations, i.e. Equation (1.1). If the spatial probability distribution of the phase error is Gaussian at every instant, and if the aperture size is much larger than the scale of the aberrations, then the exponential form of the Maréchal approximation (Ross 2009) can be used to estimate the Strehl ratio:

$$SR(t) = \frac{I}{I_0} = exp\left[-\left(\frac{2\pi(OPD_{RMS}(\mathrm{t}))}{\lambda}\right)^2\right], \tag{1.4}$$

where OPD_{RMS} is the root-mean square of the Optical Path Difference (OPD) for the laser beam, to be discussed in more detail below. It has been shown that the large aperture approximation generally under-estimates the time-averaged Strehl ratio, and thus should be used cautiously (Duffin 2009, Porter 2011a).

Equation (1.4) shows that the effect that a given optical aberration has on the farfield performance of a beam increases as the wavelength of the laser decreases. For fast-moving aircraft like jet fighters or transports, this means that compressible flows in the immediate vicinity of the aircraft that would have a negligible effect on a 10.6 μm wavelength beam could potentially impose a severe limit on the ability to effectively focus a beam with a wavelength of 1 μm on a farfield target. In particular, the density

variations in the compressible flows surrounding the aircraft produce variations in the index of refraction according to the Gladstone-Dale relationship:

$$n(x, y, z, t) - 1 = K_{GD}\rho(x, y, z, t), \tag{1.5}$$

where *n* is the index-of-refraction, K_{GD} is the Gladstone-Dale constant (0.225 cm^3/g at 1 μm (Gilbert 1993)), and ρ is the density field (Settles 2001). The magnitude of optical aberrations is expressed in terms of the Optical Path Length, *OPL* (Klein 1970), which is defined as the integral of the index of refraction over the path traversed by a light ray in the beam:

$$OPL(x, t) = \int_{y_1}^{y_2} n(x, y, t)dy. \tag{1.6}$$

The relative difference in the *OPL* over the aperture is known as the Optical Path Difference (*OPD*) and is defined as:

$$OPD(x, t) = OPL(x, t) - \overline{OPL}(x, t). \tag{1.7}$$

The OPD_{RMS} (shown in Equation (1.4)) is then the root-mean-square of the *OPD* variations over the optical aperture.

Figure 1.2 plots the dependence of the Strehl Ratio on the wavelength (Equation (1.4)) for a nominal aberration that would produce a Strehl Ratio of 0.95 for a CO_2 laser with a wavelength of 10.6 μm. The figure shows that the same flowfield that has a negligible effect on a CO_2 laser would yield a much smaller Strehl Ratio of 0.04 for a system with a shorter wavelength of 1 μm.; as such, Figure 1.2 shows that all of the advantage gained by using a shorter wavelength as shown in Figure 1.1 can very easily be negated by aero-optic effects. Based on the strong effect that aero-optic aberrations

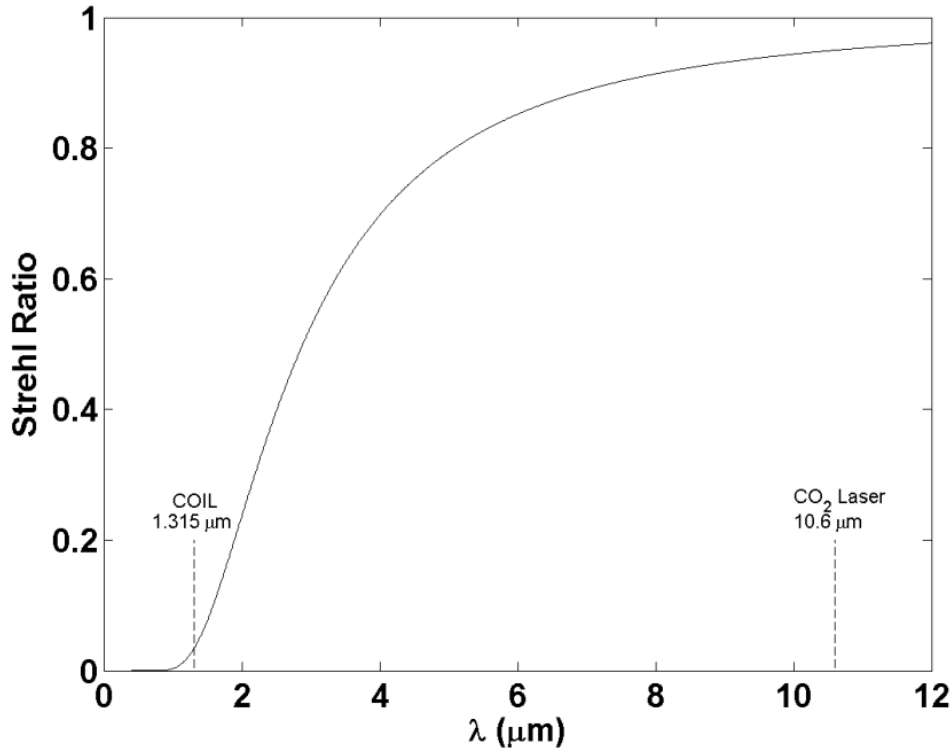

Figure 1.2. Strehl Ratio as a function of wavelength for a constant OPD_{RMS} that would produce a Strehl ratio of 0.95 on a CO_2 Laser. These same aberrations would produce a Strehl Ratio of 0.04 on a COIL (Jumper 2001).

can have on the system performance, it is apparent that there is a need for research into methods for decreasing the aero-optic aberrations on the outgoing beam from an aircraft-mounted optical system.

In summary, as investigators move towards shorter wavelength lasers, there becomes an inherent increase in the importance of designing the mounting system for the optical system in a manner that prevents or mitigates aero-optic distortions. In 1980, a mounting geometry that produced a Strehl Ratio of 0.95 using a CO_2 laser would be unacceptable for a system using a shorter wavelength today. Therefore, there now

exists a critical need for design methodologies that will prevent or minimize nearfield aero-optic flowfields and/or their effects.

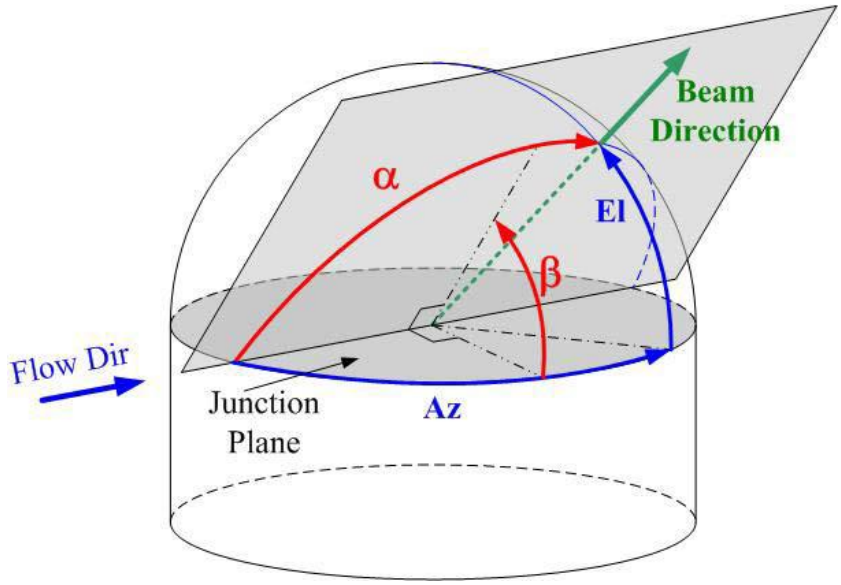

Figure 1.3. The beam direction defined by the elevation angle (α) and azimuthal angle (β) (Porter 2011a).

1.2 Advantages and Disadvantages of Spherical Turrets

In many cases, optical systems that are mounted on an aircraft are mounted in spherical turrets. Perhaps the foremost advantage to using a spherical turret is that the spherical turret is rotationally symmetric, Figure 1.3. The rotational symmetry means that the simple spherical turret can be aimed in any direction without obscuring the outgoing beam by any attached structures or fairings. More importantly, the fundamental aerodynamic character of the turret does not change with aiming direction. As such, the turret is not susceptible to large changes in aerodynamic forces

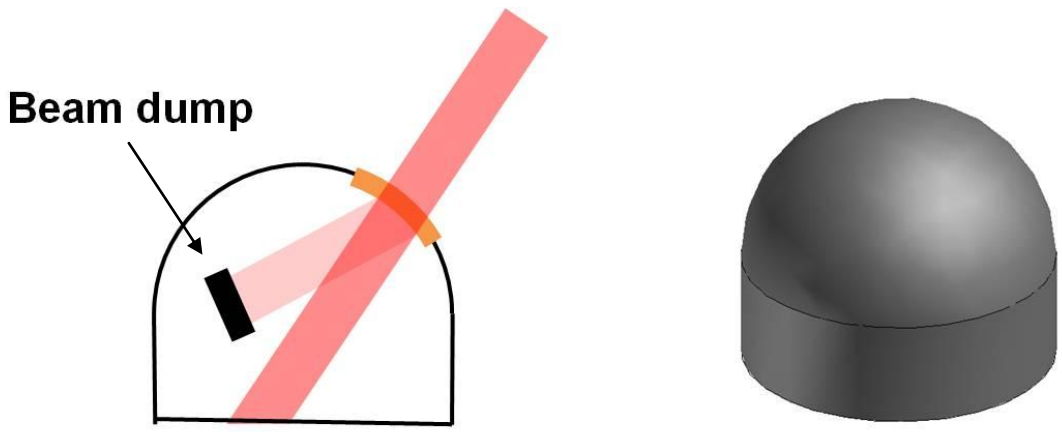

Figure 1.4. In order for the internal reflection of the beam to not destroy the internal optics, a beam dump needs to be placed inside the turret to absorb the reflection of the beam.

that may make it difficult to track the target, especially if the large changes in aerodynamic forces occur over small changes in aiming direction.

A second reason for using a spherical turret is that it allows the laser beam to be pointed in any direction while maintaining a fixed orientation between the outgoing beam and the optical window of the turret. In particular, to maximize transmission of the outgoing beam, optical windows must typically be designed for the outgoing beam to pass through the window at only a single, specific angle. Even at the optimum transmission angle, a small amount of the beam would still be reflected from the window back into the turret. Figure 1.4 shows that the reflected laser energy would have to be absorbed by a beam dump and it is realistic to assume that this beam dump could only be designed for a single orientation of the beam with respect to the window due to space limitations within the turret. As such, a practical turret design must assume

that the outgoing beam will have a fixed orientation with respect to the optical window, so that pointing the outgoing beam must be accomplished by rotating the turret rather than changing the orientation of the outgoing beam within the turret itself. The need to rotate the turret to aim the beam further supports the use of rotationally-symmetric shapes (i.e. cylindrical or spherical), at least in the region where the optical window is located, since these shapes can be rotated without altering the basic aerodynamics of the turret.

1.2.1 Critical Mach Number Issues

The above discussion has shown that there are several advantages to using a spherically-shaped turret configuration. Due to these advantages, the flow characteristics around the spherical turret have been extensively studied (Gordeyev 2010, Morgan 2009, Tutkun 2007).

On the other hand, spherical turrets are not ideal shapes for avoiding aero-optic flows. This is because, first, the high curvature of the spherical turret shape accelerates the flow around the sphere thereby producing high local flow speeds on the sphere. Specifically, the highest local flow speed on the surface of an object occurs at the location of minimum pressure; for a sphere, this location is at the top of the sphere where, in inviscid, incompressible flow, the minimum pressure coefficient, C_{P0}, is -1.25 (White 1994). For a hemispherical turret on a cylindrical base with height $D/3$ (D is the hemisphere diameter), experimental measurements have shown that the minimum C_{P0} is also approximately -1.25 (Gordeyev 2010). These minimum incompressible C_{P0} values

can be corrected for Mach-number effects using a correction such as the Karmen-Tsien compressibility correction (Karmen 1941, Tsien 1939):

$$C_P = \frac{C_{P0}}{\sqrt{1-M_\infty^2} + \left(\frac{M_\infty^2}{1+\sqrt{1-M_\infty^2}}\right)\frac{C_{P0}}{2}}. \tag{1.8}$$

Equation (1.8) shows that the minimum C_{P0} on the spherical turret becomes increasingly more negative as the freestream Mach number, M_∞, increases. In fact, when M_∞ increases beyond a certain value, then the local flow at the location of minimum C_{P0} on the sphere becomes supersonic. This "critical" Mach number at which the flow first becomes supersonic can be estimated using (Anderson 2003)

$$C_{p_{crit}} = \frac{2}{\gamma M_{crit}^2}\left[\left(\frac{1+\frac{\gamma-1}{2}M_{crit}^2}{1+\frac{\gamma-1}{2}}\right)^{\frac{\gamma}{\gamma-1}} - 1\right]. \tag{1.9}$$

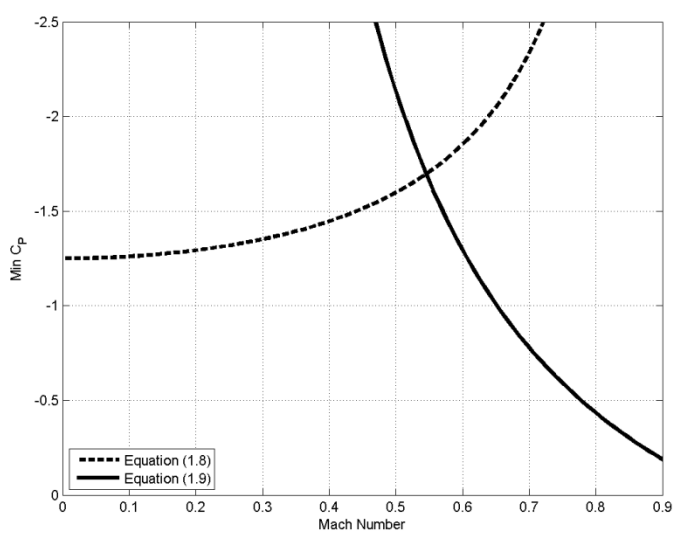

Figure 1.5: Critical Mach number for a turret using the Karmen-Tsien compressibility correction formula.

The intersection of this curve and the Karmen-Tsien compressibility correction formula, Figure 1.5, shows that supersonic flow first occurs on the sphere at a freestream Mach number of approximately 0.55. This critical Mach number for the formation of supersonic flow has important implications on the aero-optic behavior of the turret because, downstream of the local supersonic flow region on the turret, the flow decelerates back to subsonic flow by passing through a shock wave, and strong aero-optic effects can be produced by this shock wave because of the change in density across the shock; furthermore, this shock wave may also cause boundary-layer separation and formation of a downstream separated-flow region which also produces strong aero-optic effects (see below).

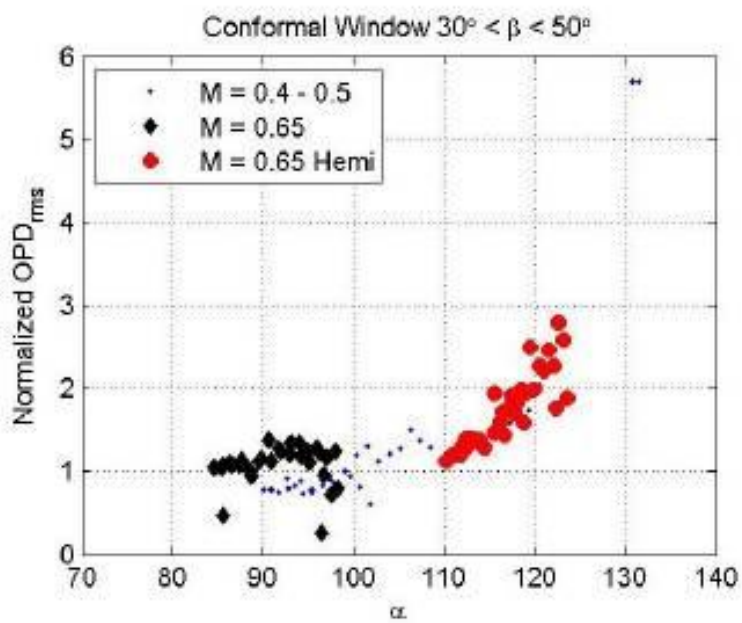

Figure 1.6. OPD_{RMS} for bands of modified elevation angles at transonic Mach numbers (De Lucca 2012).

The M_{crit} = 0.55 predicted by Equations (1.8) and (1.9) above has been validated by recent measurements performed on Notre Dame's Airborne Aero-Optics Laboratory (AAOL). The AAOL is a flight-test program that is dedicated to the investigation of aero-optic effects on airborne optical systems. As shown by De Lucca (2012), optical measurements on a spherical turret with a conformal window have shown evidence of supersonic flow and shock formation at a M_∞ of approximately 0.55. Specifically, detailed OPD_{RMS} data acquired by De Lucca are shown in Figure 1.6 for different elevation angles using the same coordinate system as that shown in Figure 1.3. The main difference between the subsonic and transonic data is the formation of a weak shock wave on the top of the turret, i.e. when α is approximately 90° in Figure 1.6. The effect of the weak shock wave can be seen by the larger OPD_{RMS} for the M_∞ = 0.65 data compared to the M_∞ = 0.4 – 0.5 data over the range 90° < α < 95°. As such, the figure shows that the shock presents an optical aberration to an outgoing beam that would

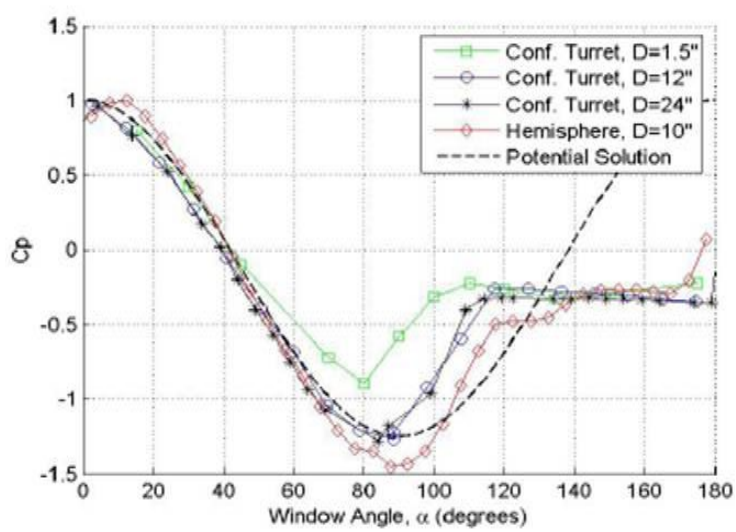

Figure 1.7. Experimental pressure distributions over a turret compared to the potential solution over a sphere (Gordeyev 2010).

become more serious as the M_∞ increases; furthermore, any unsteady motion of the shock would make it difficult to correct using an adaptive-optic (AO) approach.

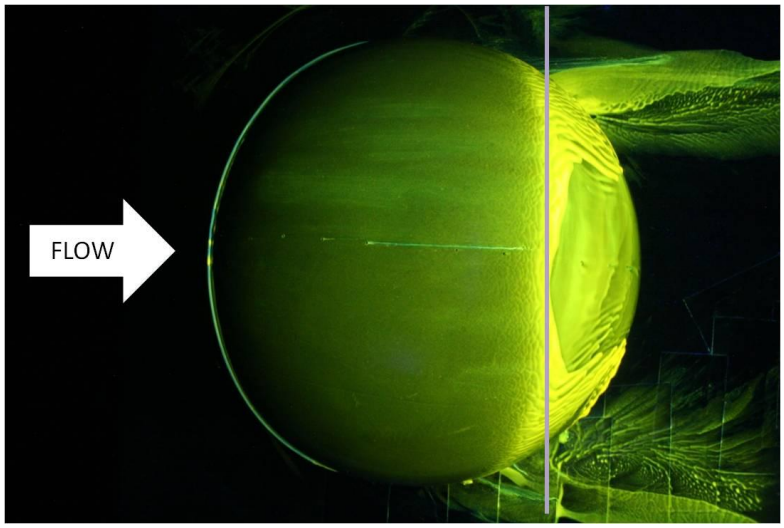

Figure 1.8. Oil Flow Visualization of a turret showing the location of separation, Re_D = 650,000. The line represents an elevation angle of 120°.

1.2.2 Flow Separation

Spherical turrets are also not ideal from an aero-optic standpoint because they are susceptible to flow separation from their aft surface. Pressure distributions measured for spherical turrets at different Reynolds numbers (Gordeyev 2010) are shown in Figure 1.7 and compared to the inviscid pressure distribution for a sphere. The figure shows that for high Reynolds numbers, the boundary-layer separation point occurs at approximately 120° from the direction of the oncoming flow. This measured location for the separation point agrees with the results of historical studies for a sphere with a turbulent boundary layer (Achenbach 1972) and more recent flow visualization

studies performed as part of this research (Figure 1.8). On the other hand, if a shock forms on the turret, the shock wave could induce flow separation from the turret at a point upstream of 120°. Once the flow separates, a shear layer is formed that seriously degrades the beam, see below. A diagram depicting the separated flow behind a spherical turret is shown in Figure 1.9.

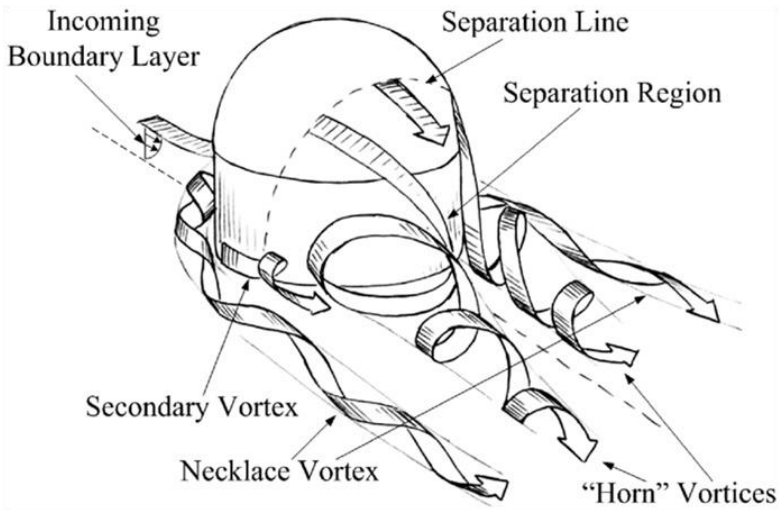

Figure 1.9. Schematic of subsonic flow around a turret (Gordeyev 2010).

1.2.2.1 Shear Layers

The separated shear layer that forms behind a spherical turret presents a severe optical aberration to any optical system that attempts to look through the shear layer. The optical aberrations produced by a shear layer were investigated by Fitzgerald (2004), who showed that the aberrations are produced by vortical structures that convect downstream in the shear layer at a speed that is approximately the average of

the high-speed flow outside of the separation region and the low-speed flow in the recirculation region. The low pressure and reduced density at the center of the shear-layer vortices result in index-of-refraction variations that impose optical aberrations on a transmitting beam of light. The magnitude of the optical aberration produced by the shear layer depends on several factors including the Mach number of the flow, and the downstream location in the shear layer (Hugo 1997).

For a shear layer with high- and low-speed Mach numbers of 0.78 and 0.12, Rennie (2008) measured an OPD_{RMS} of 0.26 μm for a beam passing through the shear layer at approximately 400 mm downstream of the origin of the shear layer; these are fairly representative of the kinds of conditions that might exist for a turret-mounted optical system carried by a jet transport or fighter. At an operating system wavelength of 1 μm, this OPD_{RMS} gives a Strehl Ratio of 0.07, meaning that only 7% of the power in the outgoing beam would be on target compared to the optimum, diffraction-limited performance. A summary of the OPD_{RMS} and Strehl Ratio for different shear layer experiments is shown in TABLE 1.

TABLE 1

SUMMARY OF EFFECT OF A COMPRESSIBLE M=0.78/0.12 SHEAR LAYER

ON THE STREHL RATIO OF A 1 μM SYSTEM.

	Shear Layer (Duffin 2009)	Shear Layer (Rennie 2008)
OPD_{RMS} (μm)	0.22 - 0.275	0.26
Strehl Ratio	0.05 - 0.15	0.07

1.2.2.2 Adaptive-Optic Corrections

A possible approach to mitigating the optical effect of an aberrating flow such as a shear layer is to employ an adaptive-optic (AO) system (Tyson 1991). AO systems are used to enhance the performance of optical systems by actively compensating for optical aberrations (Tyson 2000), and are typically used to improve image quality in optical and infrared astronomical telescopes, to aid in the imaging and tracking of rapidly-moving space objects, and to compensate for laser beam distortions (Roggemann 1996). Most AO systems are made of three different subsystems, as shown in Figure 1.10. The first subsystem is a wavefront sensor that measures the wavefront distortions of the optically-aberrating region of interest; these measurements can originate from, for example, glint from the target, or a light beacon that is intentionally created for this purpose (Rennie 2012). The second part of the AO system is a

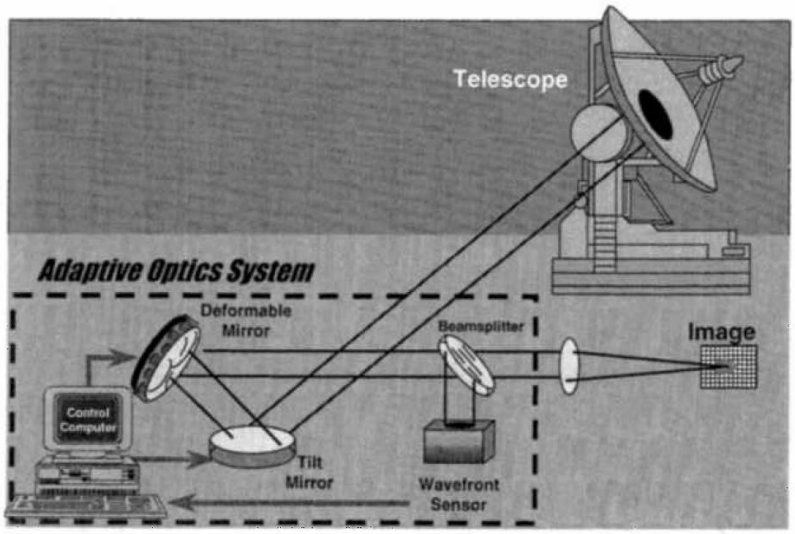

Figure 1.10. Basic components of an adaptive-optics system (Tyson 2000).

deformable mirror that can change its surface shape to place the conjugate of the measured wavefront distortions on an outgoing beam of light. The third subsystem is a computer that analyses the distortions from the wavefront sensor and uses actuators to deform the mirror correctly (Tyson 2000).

Considered individually, these subsystems are generally fast enough to deal with the high frequencies that are present in typical aero-optic flows. However, as discussed in Nightingale (2005), the overall control loop used to drive these subsystems places significant bandwidth limitations on the conventional closed-loop AO system. Specifically, Nightingale (2005) shows that a closed-loop AO system must typically operate at least 100 times the frequency of the optical aberration that is being corrected; this bandwidth is typically not achievable by existing AO systems.

A study by Duffin (2009) shows in greater detail the limitation of conventional AO systems to correct the high frequencies associated with aero-optic aberrations. In particular, every AO system has latency issues that originate from (1) the update frequency, f_u (Hz), of the applied correction and (2) the time it takes for the AO computer to read the aberrated wavefront and apply it to the deformable mirror, τ_2(s). In order to compute the latency effects, a characteristic aero-optic disturbance frequency, f_d (Hz), is also defined for the aberrating flow. Figure 1.11 plots the achievable AO correction (i.e. $-10 * \log_{10}[OPD_{RMS,corrected} / OPD_{RMS,uncorrected}]$) as a function of f_u, f_d, and τ_2. The solid line plots the required number of updates per cycle of the aero-optic disturbance, for a system that has no computer-related latency, i.e. $\tau_2 = 0$. On the other hand, Figure 1.11 shows that for non-zero values of the computer

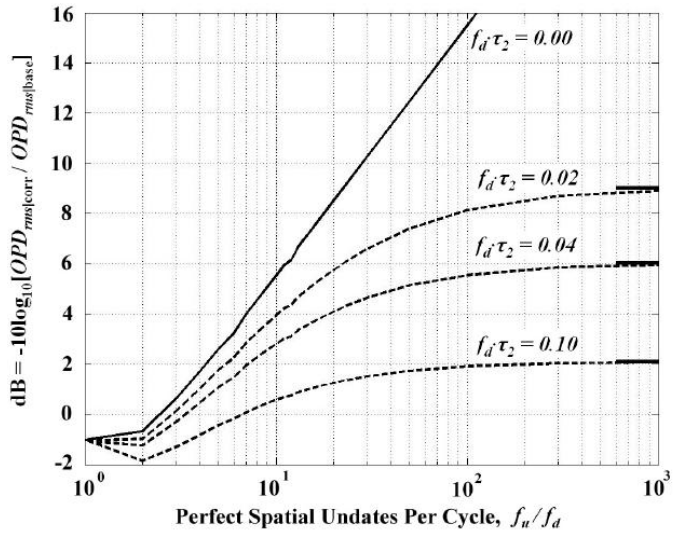

Figure 1.11. Adaptive-optic system requirement estimation of aero-optic effects (Duffin 2009).

latency, the performance of the AO system will asymptote to a maximum value shown by the horizontal lines on the right side of the figure.

As an example, consider the shear layer data shown in TABLE 1 where the $OPD_{RMS,uncorrected}$ = 0.26 µm (λ = 1 µm) and f_d = 3 kHz. Using Equation (1.4), the Strehl ratio is approximately 0.07. In order to increase the Strehl to 0.90, the $OPD_{RMS,corrected}$ must be reduced to 0.052 µm, giving a ratio of the corrected to uncorrected of 0.2, or 6.9 dB. Assuming no computer latency, $\tau_2 = 0$, Figure 1.11 shows that there needs to be 10 updates for each disturbance. Therefore, the update frequency must be 30 kHz for a perfect system with no latency. Assuming a typical controller gain of $\beta = 0.1$, the required sampling rate is estimated to be 1.9 MHz, which is much faster than the rates

that are achievable by even typical high-speed wavefront sensors (Cavalieri 2007). Note that system latencies (i.e. $\tau_2 > 0$) would increase the required update rate still further.

The above example illustrates how current state-of-the-art AO systems are unable to match the high temporal frequencies associated with aero-optic flows such as the separated shear layer that forms at the rear of a spherical turret. As such, feed-forward AO approaches are also under investigation (Rennie 2008) that employ flow-control techniques to force and regularize the shear layer, thereby increasing the effective bandwidth of the AO system. Specifically, when forced, the turbulent energy of the shear layer goes preferentially into the formation of large-amplitude vortical structures, with passing frequency dictated by the forcing actuator, rather than into broadband turbulent fluctuations (Rennie 2008). The resulting optical aberration is then highly periodic with a phase that is linked to the phase of the forcing actuator; so that most of the optical aberrations produced by the forced shear layer can be removed using a simple deformable-mirror (DM) shape that is correctly synchronized with the passing of the shear-layer vortical structures (Rennie 2008). Investigations have also been performed into the use of low-order optical measurements, such as a Malley probe, to synchronize the DM motion with the phase of the shear layer (Nightingale 2009). Despite these successes, the feedforward AO correction is still not an operationally-proven technique, and would introduce considerable additional complexity if implemented on an actual, deployed turret and optical system. In summary, although AO approaches show promise, there is still significant advantage if

the mounting system for airborne-mounted optical systems can be designed to avoid the formation of shock waves and separated-flow regions in the first place.

1.3 Summary of Spherical Turret Performance

The preceding sections have shown that there are considerable advantages to employing the canonical spherical-turret configuration as a mount for airborne optical systems. Specifically, the hemispherical turret provides a convenient and proven method to aim the outgoing beam in any direction, while satisfying the optical-window and beam-dump requirements of the system. On the other hand, aero-optic flows associated with spherical turrets can severely limit the effective field of regard of a turret-mounted system. These aberrating flows include shocks that form on the turret for $M_\infty > 0.55$, and the separated shear layer at the rear of the turret.

As such, this introductory chapter shows that new turret designs are needed that retain the aiming and transmission advantages of the spherical turret, while eliminating or mitigating the strongly-aberrating aero-optic flows to which spherical turrets are susceptible. This problem is the focus of the investigation described in this dissertation. In the next chapter, an aerodynamic design for airborne optical turrets is presented that is specifically intended to prevent the formation of shock waves and shear layers around the optical aperture, thereby avoiding degradation of the beam due to aero-optic effects in the first place.

CHAPTER 2:

A PASSIVE APPROACH TO THE MITIGATION OF AERO-OPTIC FLOWS

2.1 Introduction

The disadvantage of spherical turrets, as discussed in Chapter 1, is that they produce strongly-aberrating flows consisting of shock waves that form on the top of the turret, and shear layers that are associated with the separated-flow region aft of the turret. In this chapter, a novel design approach that minimizes these flow features is described.

2.2 Underwing Pod

A study was done by Rennie (2010) and continued by Crahan (2011) into the design of an optical mount that was designed to minimize aero-optic flows and that could be integrated into a pod that could be carried under the wing of a fighter aircraft. The constraints of this study were to mount the optical system inside a pod that was approximately the size of the 380 gallon external fuel tank carried by a legacy fighter aircraft, and that the nominal flight speed would match that of a fighter aircraft at cruise speed ($M_\infty \approx 0.8$). An early decision that was made in the study was that that the optical aperture for the outgoing beam would be mounted in a spherically-shaped turret at the

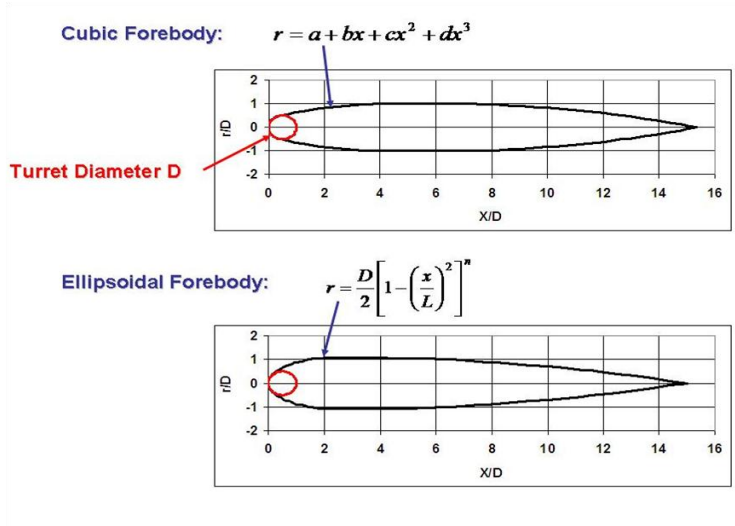

Figure 2.1. Examples of pod or fairing shapes that increase the critical Mach number on the turret ball to M_∞ = 0.8 (Rennie 2010).

nose of the pod, due to the numerous advantages of the spherical-turret geometry presented in Chapter 1.

2.2.1 Fairing Work

The first method investigated in Rennie (2010) to reduce aero-optic effects on the aircraft-mounted pod was to fair the spherical turret at the front of the pod into the downstream pod body. The objective of the fairing was to reduce the curvature of the turret at the nose of the pod (i.e. “streamline” the turret), thereby reducing the maximum local flow speed on the turret. In this case, the fairing not only reduces the maximum flow speed and hence critical Mach number of the turret, but the fairing also reduces pressure gradients on the body so that the chance of flow separation is also reduced. As such, a fairing deals with both of the disadvantages of the spherical turret

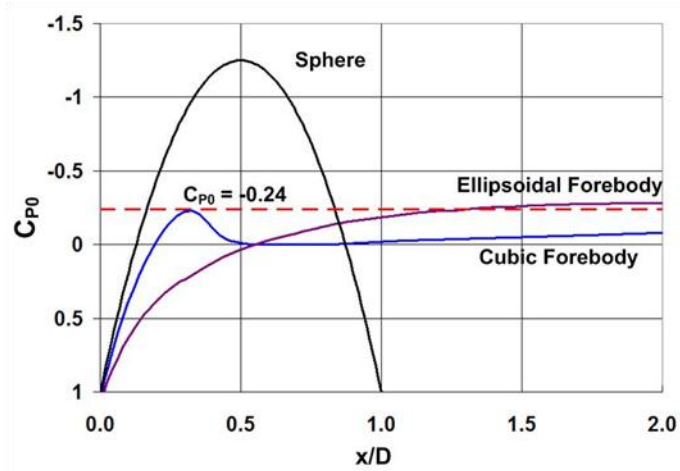

Figure 2.2. CFD-computed pressure distributions for basic pod shapes shown in Figure 2.1 (Rennie 2010).

described in Chapter 1; that is, a low critical Mach number and a large aft pressure gradient that produces flow separation.

One of the streamlining shapes for the forebody investigated in Rennie (2010) was the ellipse, given by:

$$r = \frac{D}{2}\left[1 - \left(\frac{x}{L}\right)^2\right], \tag{2.1}$$

where *r* is the radial coordinate of the fairing forebody in a cylindrical coordinate system, and *L* is the length of the ellipsoid forebody long axis. Another fairing shape that was tested used a simple cubic to blend the turret ball at the front of the pod with the ogive-shaped downstream tail of the fairing; this pod shape was denoted "cubic forebody:"

$$r = a + bx + cx^2 + dx^3. \tag{2.2}$$

Ellipsoidal and cubic-forebody pod shapes that were found to meet the design objectives are shown in Figure 2.1. The shapes are bodies of revolution consisting of a

front turret ball and an ogive tail that are blended using the forebody shapes described by Equations (2.1) and (2.2).

Pressure distributions for the fairing shapes were computed using a computational fluid dynamics (CFD) code called COBALT (Strang 1999). In order to more rapidly evaluate a larger number of possible fairing shapes, the CFD computations were performed using an inviscid-Euler routine. The boundary at the inlet and outlet was a farfield boundary, the center and bottom were symmetry planes, and the pod surface was a solid wall. The inviscid-Euler approach was justified since one of the objectives of the study was to prevent flow separations on the pod and therefore maintain a flow around the pod that is close to the inviscid-Euler approximation.

As shown in Figure 2.2, both the cubic- and ellipsoidal-forebody shapes shown in Figure 2.1 raise the minimum C_{P0} on the spherical turret from -1.25 (inviscid flow with

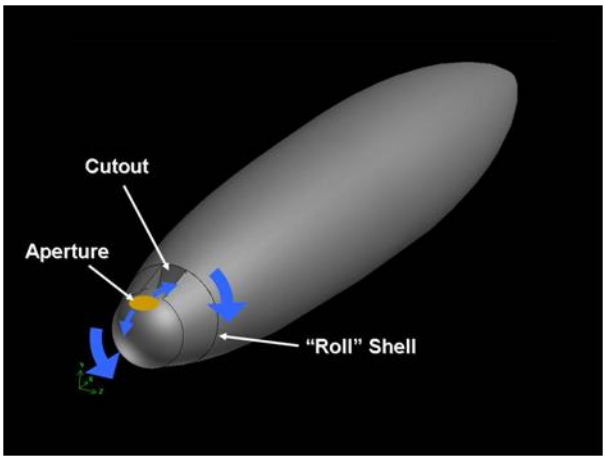

Figure 2.3. Basic aero-optic pod layout based on the "cubic-forebody" shape, including a basic cutout to enable a greater range of lookback angles (Rennie 2010).

no fairing) up to -0.24. Using Equation (1.9) this minimum C_{P0} corresponds to a critical Mach number of 0.8, so that both fairings would prevent supersonic flow in the vicinity of the turret ball up to a freestream Mach number of 0.8. On the other hand, the cubic-forebody shape is thinner, particularly around the front section of the pod, and therefore has some advantage over the ellipsoidal-forebody shape if space constraints are important.

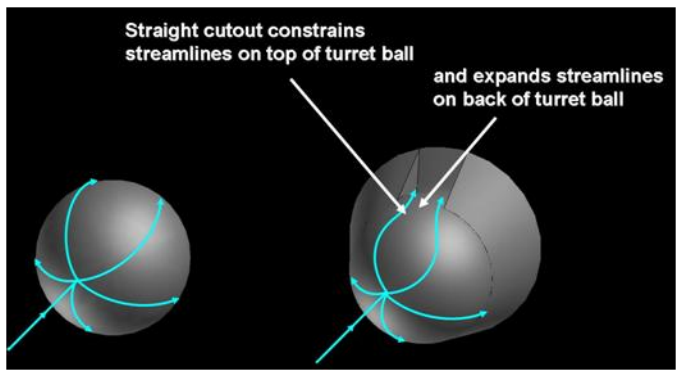

Figure 2.4. Illustration showing how straight cutout walls constrain streamlines on the turret ball (Rennie 2010).

2.2.2 Virtual Duct Concept

A problem with the fairings shown in Figure 2.1 is that they connect to the surface of the turret ball at a point that is only approximately 60° past the forward-looking direction, so that the field of regard of an optical aperture on the turret ball would be significantly restricted by the downstream fairing. One method of increasing the maximum lookback angle of the optical aperture is to remove a cutout in the pod body immediately downstream of the turret ball. This cutout would roll with the turret ball around the longitudinal axis of the pod in a rotatable section called a "roll shell."

The isometric sketch shown in Figure 2.3 includes a cutout and roll shell, and shows how the turret ball would be rotated to aim the outgoing beam in different directions.

In Figure 2.3, the cutout that enables the aperture to rotate to aft pointing angles has simple, straight walls that are separated by the aperture diameter so that the edges of the aperture will not be obscured by the pod. CFD results show, however, that the critical Mach number for this "simple" cutout design is significantly lower than the M_∞ = 0.8 target. Part of the cause for this reduction in critical Mach number can be attributed to the fact that the cutout removes some of the streamlining effect of the downstream pod body in the vicinity of the optical aperture. The CFD investigations also showed that the reduction in critical Mach number can also be attributed to the straight walls of the cutout. In particular, as shown schematically in Figure 2.4, the flow normally follows "lines of longitude" along the surface of the turret ball; however, the straight

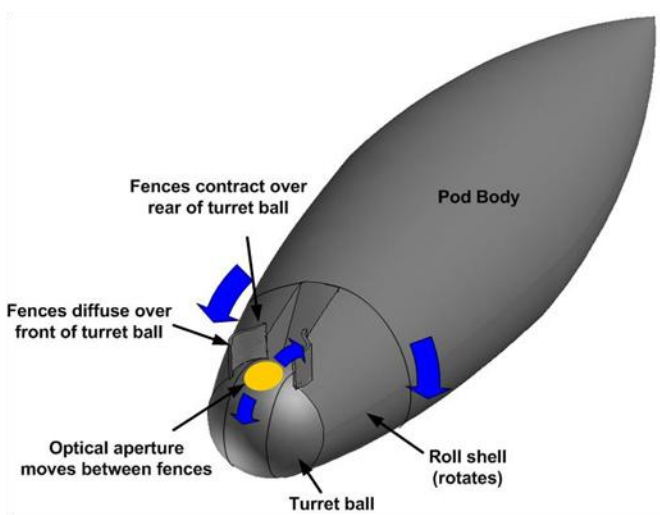

Figure 2.5. Pod with improved cutout and fence (i.e., "virtual duct") installed to control flow around aperture (Rennie 2010).

walls of the “basic” cutout shown in Figure 2.3 disrupt this flow pattern by constricting the streamlines over the top of the turret ball, resulting in increased flow speeds over the top of the ball and therefore contributing to the observed reduction in critical Mach number. The straight cutout walls also diffuse the flow on the back of the ball faster than if the flow followed lines of longitude on the ball surface; this higher diffusion increases the adverse pressure gradient on the back of the turret ball thereby increasing the risk of flow separation and associated aero-optic aberrations.

Based on the preceding results, the innovation of Rennie (2010) was to recognize that the aero-optic performance of the pod could be significantly improved by carefully shaping the cutout to control the flow over the spherical turret at the nose of the pod. In particular, rather than use a simple, straight-walled cutout as shown in Figure 2.3, the cutout was instead shaped to diffuse the flow at the front of the turret ball, thereby reducing the maximum flow speed over the turret, and to contract at the back of the ball, thereby reducing the chance of flow separation by accelerating the flow over the back of the ball. Furthermore, the effectiveness of the cutout walls was enhanced by extending the walls into the flow with a “fence.” The inner surfaces of these fences, together with the spherical surface of the turret itself, forms what can be called a “virtual duct” (Rennie 2010), which could be shaped in such a way as to prevent aero-optically aberrating flows. In effect, the walls of the virtual duct are shaped to counteract the normal curvature of the surface of the spherical turret itself, so that the flow near the optical aperture “feels” as if it is flowing through a duct with a more-constant cross-sectional area. An example of a pod with a virtual duct installed is

shown in Figure 2.5. The wall coordinates of the virtual duct were determined using fifth-order polynomials for both the contracting and diffusing sections, discussed in more detail in Chapter 5; note that the use of fifth-order polynomials is often used for wind-tunnel contraction design (Saric 1998).

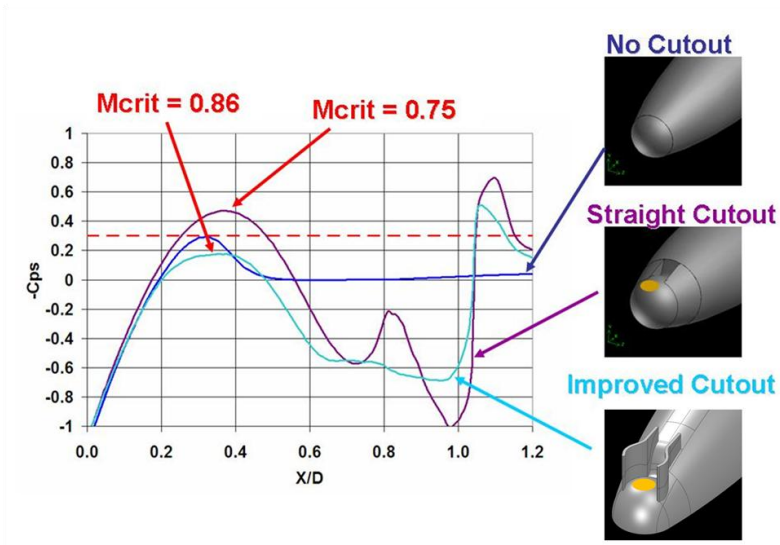

Figure 2.6. CFD-computed pressure distributions around the turret ball and critical Mach numbers for different cutout configurations. "Straight" and "improved" cutout configurations are designed for a maximum lookback angle of 20° (Rennie 2010).

Pressure distributions along the centerline of the cutout, computed using CFD for the unmodified pod, the pod with a simple straight-wall cutout, and a pod with improved cutout (i.e. a virtual duct), are shown in Figure 2.6. The figure shows that the critical Mach number for the pod with the improved cutout is even higher than for the unmodified pod shape (M_∞ = 0.86 versus M_∞ = 0.8). Further, the adverse pressure gradient on the back of the turret ball has also been reduced, which reduces the possibility for flow separation and associated aero-optic aberrations. As such, the virtual

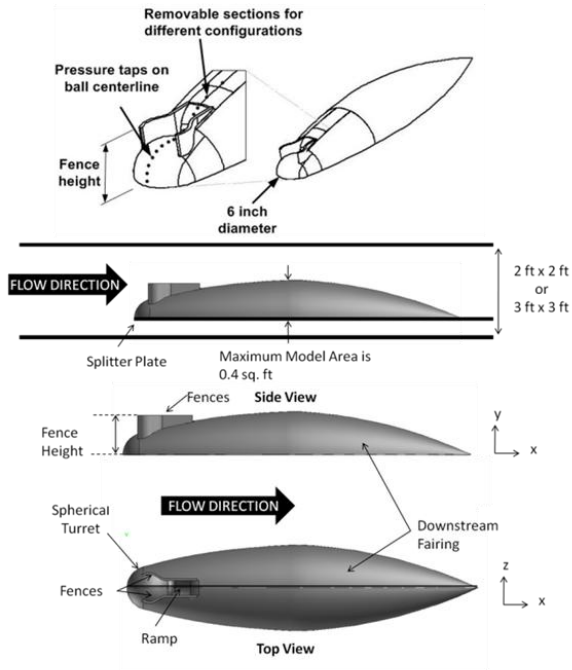

Figure 2.7. Picture of experimental model showing (top) the pressure taps along the centerline of the model and (bottom) how the model looks in the wind tunnel (Crahan 2011).

duct approach effectively modifies the flow over the spherical turret ball to reduce the chance of producing aero-optically aberrating flows such as shocks and flow separation.

The virtual-duct approach is also a “passive” flow control approach in the sense that it does not rely on actuators or suction/blowing. The technique is applicable to other turret designs, including canonical hemispherical turrets such as shown in Figure 1.9.

2.2.3 Experimental Validation of the Virtual Duct Approach

An experimental investigation of the virtual duct concept is described in Crahan (2011). The wind tunnel tests were conducted in two different facilities at the University

of Notre Dame. The first facility was a two foot by two foot subsonic wind tunnel that can reach speeds of $M_\infty \approx 0.1$. The second wind tunnel was a closed-circuit wind tunnel with a three foot by three foot test section and a top speed of $M_\infty \approx 0.6$ (but was only used at $M_\infty = 0.1$ for this experiment).

A schematic of the experimental setup including a detail of the model used in the tests is shown in Figure 2.7. First of all, in CFD studies it was shown that modeling only the top half of the pod produced flow results around the turret and virtual duct that were very close to the results obtained when modeling the full pod. As such, in order to maximize the size of the model while keeping the model blockage within acceptable limits, only the top half of the pod was built and placed on a splitter plate in the tunnel, as shown in Figure 2.7.

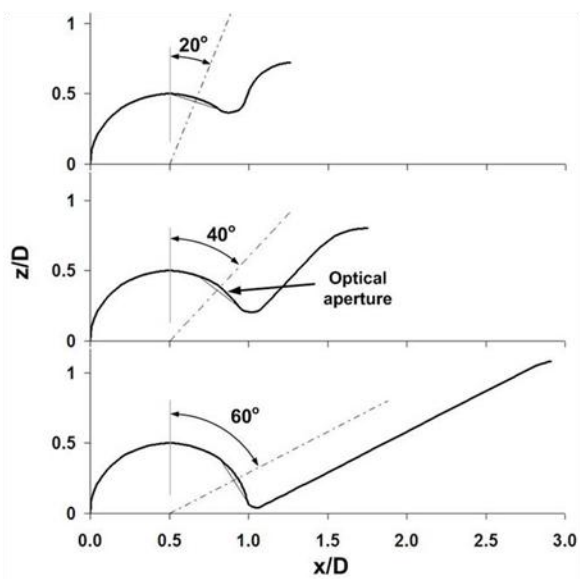

Figure 2.8. Side view of the centerline of the pod for lookback angles of 20°, 40°, and 60° (Crahan 2011).

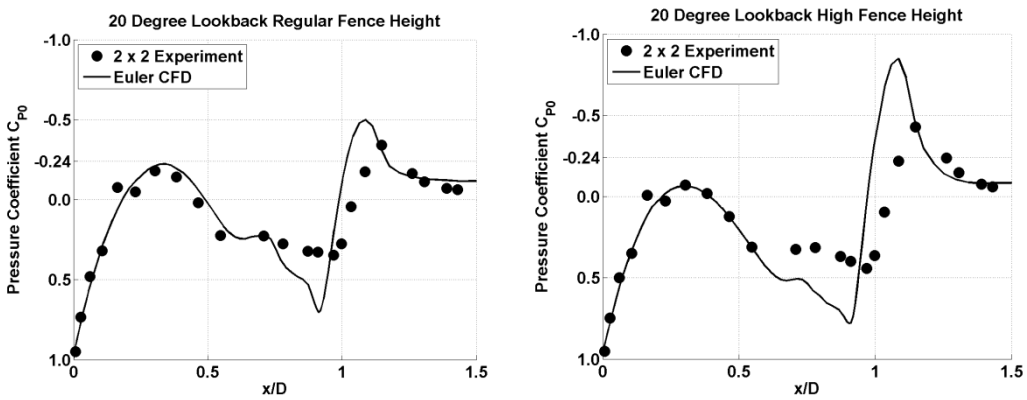

Figure 2.9. Experimentally and computationally-determined pressure distributions for pod model with 20° lookback angle for a high (left) fence height and a regular (right) fence height (Crahan 2011).

The front of the experimental model used to test the virtual duct concept was also made out of interchangeable parts. The interchangeable parts allowed for the testing of different pod configurations that allowed different maximum lookback angles, consisting of 20°, 40°, and 60°; Figure 2.8 shows the centerline profile of the turret ball and aft ramp located between the virtual-duct fences at the front of the pod, for these three lookback angles. The height of the virtual duct was also adjustable, with the fence height of the duct defined as the distance from the center of the turret ball (i.e. the floor level for the wind-tunnel model) to the top of the virtual-duct fences, as shown in the topmost drawing in Figure 2.7. The model was also instrumented with pressure taps along the centerline of the pod that were roughly 0.013 m (0.5 inches) apart. For each pressure measurement, the program took 2050 samples over 0.5 seconds and placed the average in a test file. It completed this 5 times for each pressure tap so that each location had 5 averaged measurements. The scanivalve completed this process for each

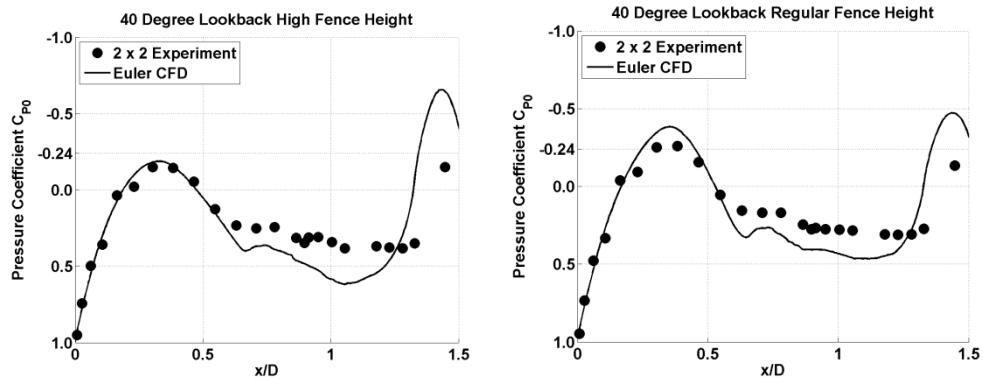

Figure 2.10. Experimentally and computationally-determined pressure distributions for pod model with 40° lookback angle for a high (left) fence height and a regular (right) fence height (Crahan 2011).

pressure tap. Once the scanivalve measured all the taps, it was reset to measure the data a second time. The average of the 5 samples taken the 1st and 2nd time to scanivalve measured the tap are the values shown below. The details of how the pressure coefficient is calculated is shown in Appendix A.

With the configuration shown in Figure 2.7, the spherical ball of the pod was D = 0.15 meters (6 in) in diameter, and the virtual-duct fence had a height of h_{REG} = 0.107 meters (4.2 in) (h_{REG}/D = 0.7) for the regular fence height and 0.137 meters (5.4 in) (h_{HI}/D = 0.9) for the high fence height. At typical test speeds in the Notre Dame low-speed wind tunnels, the Reynolds number based on the diameter of the turret ball was $Re_D = 3.4 \times 10^5$, which is near the transitional value of 3×10^5 or 4×10^5 for a sphere (Schlichting 1979). To further ensure turbulent flow a 1 mm diameter wire was placed near the front of the sphere to trip the boundary layer.

Figures 2.9, 2.10, and 2.11 show the measured pressure distributions on the centerline of the spherical turret between the virtual-duct fences, for the three lookback configurations shown in Figure 2.8 respectively, and also for regular and high fence-height configurations. All of the pressure data shown in the figures were corrected for wind-tunnel blockage effects using the method of Maskell (1963) (see Appendix A). Note that some of the experimental data sets in Figures 2.9 to 2.11 show an unusually low C_{P0} value at a single point on the front of the turret ball; this unusual C_{P0} reading was caused by the influence of the wire that was attached to the front of the turret to trip the boundary layer in each of Figures 2.9 to 2.11, the solid line shows the Euler CFD solution and the dots show the experimental results measured in the two foot by two foot wind tunnel.

There are several points that can be made from the experimental results shown in Figures 2.9 to 2.11. First, the figures show that the virtual-duct approach significantly

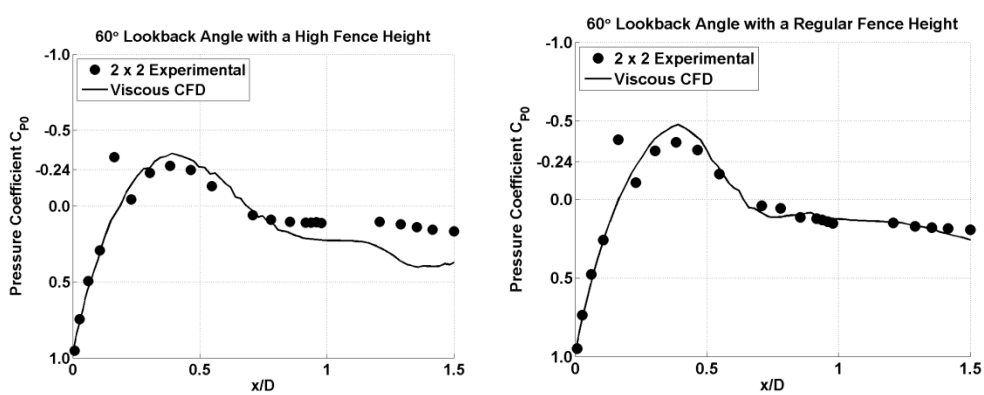

Figure 2.11. Experimentally and computationally-determined pressure distributions for pod model with 60° lookback angle and high (left) fence height and a regular (right) fence height (Crahan 2011).

reduces the maximum local flow speed on the turret ball. Taking the minimum C_{P0} from each configuration, the critical Mach number (calculated using Equation (1.8)) for all tested configurations is summarized in TABLE 2. As shown in the table, the design objective of delaying shock formation up to M_∞ = 0.8 was achieved for the 20° and 40° lookback-angle cases, and nearly for the 60° case with the high fence. Note that a sphere has a critical Mach number of 0.55.

Finally, Figures 2.9 to 2.11 show that the Euler routine does a reasonably-good job of matching the experimentally-measured minimum pressure on the spherical turret. The reason why the Euler routine compares closely to the experiment must be due to the fact that the flow over the turret in this region is close to the inviscid case. This close comparison suggests that an Euler routine can be used to perform preliminary investigations and screening of how well new virtual-duct designs perform in terms of raising the critical Mach number.

TABLE 2

CRITICAL MACH NUMBER FOR DIFFERENT LOOKBACK ANGLES AT DIFFERENT FENCE HEIGHTS BASED ON EXPERIMENTAL DATA (CRAHAN 2011).

Lookback Angle	Critical Mach number for a Regular Fence Height	Critical Mach number for a High Fence Height
20°	0.83	0.91
40°	0.79	0.85
60°	0.75	0.79

On the other hand, there are several concerns with the data shown in Figures 2.9 to 2.11. First of all, although there is a significant reduction in the pressure gradient on the rear of the spherical turret, it is not clear from the measured pressure distributions how much the boundary-layer separation point is being delayed by the virtual duct. For example, most of the experimental pressure distributions in Figures 2.9 to 2.11 show a sharp leveling off of the C_{P0} distribution starting at a location of x/D ~ 0.6 on the turret ball, corresponding to an elevation angle of approximately 100° with respect to the oncoming flow. This leveling off of the C_{P0} distribution is a common indication of boundary-layer separation since the pressure tends to remain constant within the separated-flow region downstream of the separation point. As such, the leveling off of the C_{P0} distribution at an elevation angle of 100° implies that the boundary layer may actually be separating *upstream* of the 120° separation point for the unmodified canonical hemispherical turret (see Figure 1.8).

To further investigate the boundary-layer separation point, oil-flow visualization studies were performed around the turret region of the pod within the virtual-duct fences. The oil that was used is a mixture of Dow Corning 200 Fluid at different viscosities. The mixture was made of a 1:1 ratio of fluids at 500 and 10,000 centistokes (cSt) and 10 drops of Engine Transmission UV dye so that the fluid will fluoresce under an ultraviolet light. The mixture is designed to be viscous enough to not move due to gravity, but can still be moved by the motion of the flow. Due to the viscosity of the fluid, the tunnel was run for more than 5 minutes so that the fluid could reach a steady state location. All oil flow visualization pictures only show the steady state location of

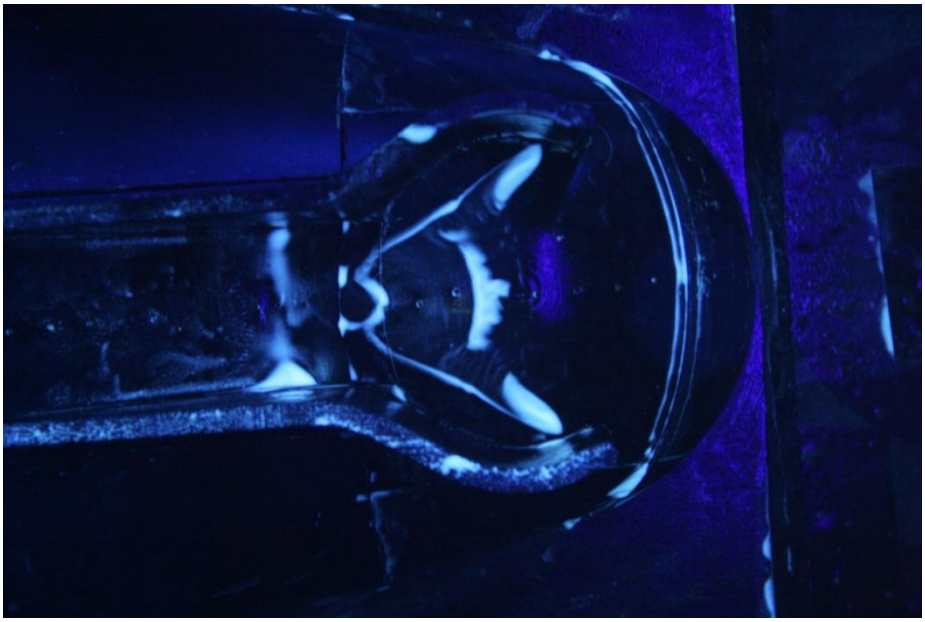

Figure 2.12. Oil flow visualization for flow over the pod.

the fluid. Figure 2.12 shows a typical photograph of the oil streaklines on the back of the turret ball and between the virtual-duct fences. The oil flow shows attached flow on the front of the turret ball, but show lines of accumulated oil that project from the corners of the virtual-duct fences diagonally across the surface of the turret, eventually meeting on the turret rear centerline. The lack of oil on the pod model downstream of these diagonal oil streaklines suggests that the flow is separated downstream of the lines, which agrees generally with the pressure distribution data in Figures 2.9 to 2.11; however, further investigation is required.

As such, the oil-flow visualization results show that the flow within the virtual duct is more complicated than originally believed, and that more work is required to fully understand the flow. Unfortunately, due to its relatively inflexible design, the pod model shown in Figure 2.7 is not ideal for the investigation of the detailed flow structure

within the virtual duct, and hence no attempt was made to further investigate the results shown in Figure 2.12. In the next chapter, experimental tests are described that were performed to more fully investigate the detailed flow structure in the virtual duct.

2.3 Concluding Remarks

The experimental pressure data has shown that the virtual duct approach can be successfully used to significantly increase the critical Mach number of a spherical turret ball. Such an increase in the critical Mach number means that the pod could be flown at cruise speeds of transport and fighter aircraft without the formation of shock waves and their associated optical aberrations in the vicinity of the optical aperture. The pressure data also showed close agreement with inviscid-Euler CFD results over the front of the turret, indicating that Euler codes can be successfully used for preliminary investigation and screening of different virtual-duct configurations regarding the prediction of critical Mach number.

The experimental pressure and oil-flow visualization data are significantly less clear, however, regarding the ability of the virtual duct to prevent flow separation on the rear of the spherical turret at the front of the pod. In particular, oil-flow visualization studies showed thick accumulations of oil that lie diagonally across the rear of the turret ball, that indicate flow separation, although further investigation is required.

It should be noted, however, that the experiments were performed at relatively-low Reynolds numbers so that, despite the presence of the boundary-layer trip wire, it is not entirely clear that the flow was fully tripped to turbulent on the turret ball. For

example, as shown by Schlicting (1979), a boundary layer trip can often fail to transition the boundary layer to turbulent if the Reynolds number is too low. As such, in the next chapter, the results of experiments are presented that were performed at a higher Reynolds number to ensure that the boundary layer on the turret ball is turbulent. Furthermore, although the fairing was shown above to have positive effects on the critical Mach number, the fairing adds additional complications to the model and makes it difficult to reconfigure the model to experimentally investigate different configurations. Based on these problems, in the next chapter, we turn our attention to a canonical turret with a virtual duct that has a larger Reynolds number than the pod in order to better understand the detailed flow structure in the virtual duct.

CHAPTER 3:

THE CANONICAL TURRET WITH VIRTUAL DUCT

3.1 Introduction

With the positive results from the underwing pod in regards to increasing the critical Mach number, a new model was made to better investigate the detailed flow in the virtual duct and the ability of the virtual-duct concept to delay separation. One problem with the underwing pod model was that the maximum Reynolds number that could be tested was relatively low, $Re_D = 3.4\text{x}10^5$. This relatively-low Reynolds number came about due to the fact that, since the pod fairing was fairly large, the spherical turret at the front of the pod had to be comparatively small so that wind-tunnel blockage effects would not be excessive. As such, to better investigate the ability of the

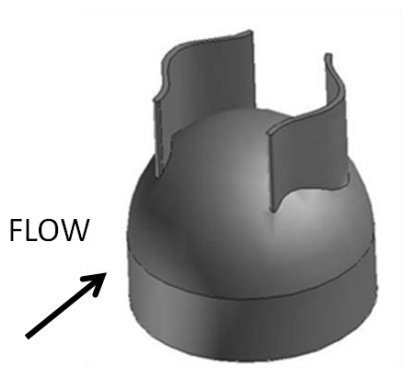

Figure 3.1. Isometric picture of a canonical hemisphere-on-cylinder turret with a virtual duct.

virtual duct to delay separation on the turret at high Reynolds number, a canonical hemisphere-on-cylinder turret model was constructed, Figure 3.1, and without the large downstream fairing representing the pod body; with these modifications, the diameter of the turret model was twice that of the pod model.

3.2 Experiments on Canonical Hemisphere-on-Cylinder Turret

The new, canonical hemisphere-on-cylinder turret was made out of a .3048 meter (12 in) diameter steel hemisphere that sits on a .3048 meter (12 in) diameter aluminum cylinder that is .102 meters (4 in) high. This turret configuration matches the turret designs tested in other investigations (Gordeyev 2010). The hemisphere was instrumented with pressure taps spaced at 10° increments, excluding the top of the hemisphere.

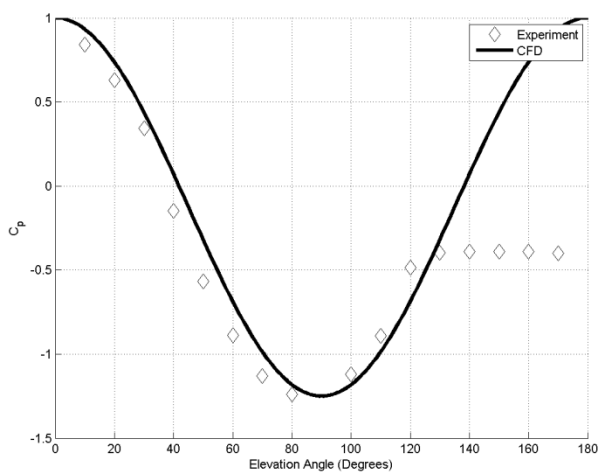

Figure 3.2. Comparison of pressure distribution found experimentally for flow over a 12 inch diameter turret.

The baseline flow over the canonical hemisphere-on-cylinder turret model was first measured with no virtual-duct fences attached. The tests were performed in the University of Notre Dame's two foot by two foot low speed windtunnel at a velocity of 34.3 m/s ($M_\infty \approx 0.1$) which gives a Re_D of 6.8 x 10^5; this Re_D is above the critical Reynolds number of 4.0 x 10^5 for a sphere (Schlicting 1979) but a boundary-layer trip was still attached to ensure that the boundary layer was turbulent. The model was placed in the middle of the test section so that the boundary layer on the wind tunnel floor would be large enough to produce the necklace vortex shown in Figure 1.9.

Figure 3.2 shows the pressure data for flow over the turret compared to the potential-flow solution for a sphere. The pressure data follows the potential-flow solution up to an elevation angle of around 120°, where turbulent flow separation

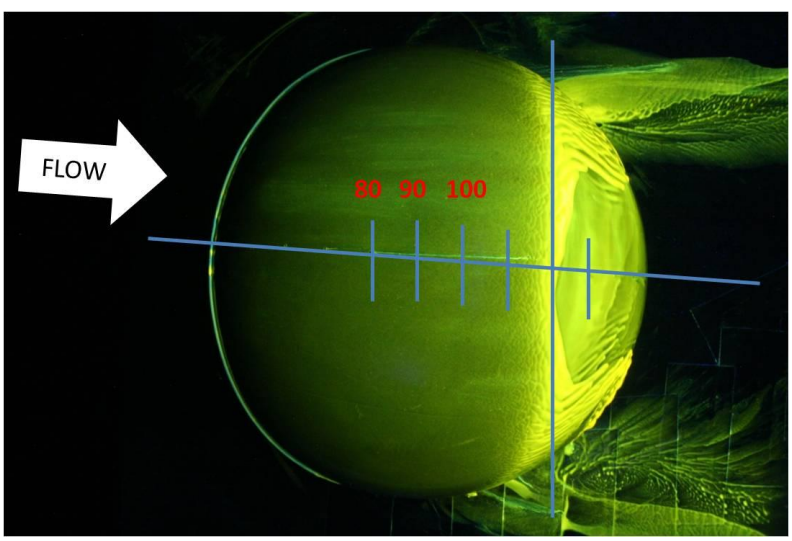

Figure 3.3. Oil-flow visualization on the canonical hemisphere-on-cylindrical-base turret model, Re_D = 6.8 x 10^5. The superposed vertical line shows the location of an elevation angle of 120°.

occurs. The experimental pressure distribution shown in Figure 3.2 is consistent with the experimental pressure distributions acquired in other studies as shown, for example, in Figure 1.7 (Gordeyev 2010).

Oil-flow visualization studies were also performed on the turret model. A photograph of the oil-flow pattern on the turret during a test at 34.3 m/s (Re_D = 6.8 x 10^5) is shown in Figure 3.3. Superposed on the photograph are vertical lines at 10° increments in elevation angle from the oncoming flow (angle α in Figure 1.3), and also a longer line at the location where the elevation angle is 120°. The flow visualization clearly shows boundary-layer separation at around the 120° location; this is indicated by the buildup of fluid at the 120° location due to the reduced skin friction close to the separation point, followed by a reduced amount of oil and/or accumulation of the oil just downstream of the separation line. A few other flow structures can be seen in this figure. First, horn vortices can be seen in the separated region away from the centerline, shown by the increase in fluid in that region. Another feature of Figure 3.3 is that the separation line on the turret decreases as the flow gets closer to the cylindrical base; this effect can also be seen in the CFD data shown in Figure 3.4, where the separation line is clearly seen to move upstream as the flow gets closer to the cylinder. In summary, the flow visualization data in Figure 3.3 shows that the baseline turret model used in the investigation has all of the main flow features observed in other supercritical-flow investigations of the canonical hemisphere-on-cylindrical base turret (Gordeyev 2010).

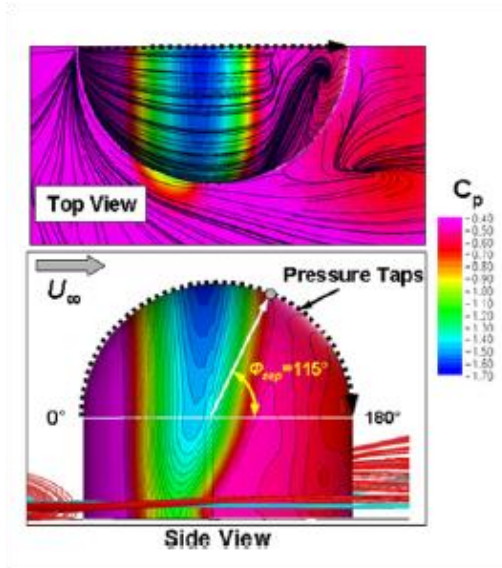

Figure 3.4. C_P distribution for hemisphere-on-cylinder turret with top (upper) and side (lower) views. These computational results are for a diameter of .3048 m (12 in) and Re_D of 23.0 x 10^5 (Ladd 2009).

3.3 Experimental Investigation of Virtual Duct on Hemisphere-on-Cylinder Turret

Once the baseline measurements were completed with the canonical turret shape, virtual-duct fences were constructed and attached. For these tests, the virtual duct was made out of flexible sheet metal that could be adjusted into different shapes. This was done by mounting a fixed vertical wall onto the turret model with horizontal mounting screws attached. The horizontal mounting screws could then be adjusted for different fence shapes and, after adjusting the screws, flexible sheet metal sections were attached to the mounting screws to form the walls of the virtual duct. This ability to adjust the fence shape enabled the rapid testing and evaluation of different fence shapes. On the other hand, the actual fence shape for any test may have had slight

irregularities and imperfections; however, the actual fence shape was measured after each test for future reference and CFD modeling.

3.3.1 Virtual Duct with Low Curvature

Oil-flow visualization studies, completed similar to the studies from Chapter 2, were first performed for a virtual duct with a radius of curvature of 0.204 meters and a maximum displacement of the center of the virtual duct fence of 0.16 meters. From the discussion of the virtual duct in the previous chapter, it is apparent that the curvature of the virtual duct has a strong effect on the performance of the virtual duct since it determines the amount of diffusion in the upstream part of the virtual duct and the amount of contraction in the downstream part. The oil-flow data for a low-curvature configuration is shown in Figure 3.5.

Looking at the flow visualization it is apparent that the virtual duct significantly delays the separation point, as shown in Figure 3.5, where a line is drawn at each 10° interval in elevation along the turret centerline, showing that the virtual-duct delays separation up to an elevation angle of about 150° for this configuration.

In addition to flow visualization, a pressure distribution was measured for the low-curvature case, shown in Figure 3.6, and compared to that of the turret without a virtual duct. The pressure distribution matches the “No Fence” case up until an elevation angle of 40°, where the fence begins to have an effect. The minimum pressure for the low-curvature case is higher than the no-fence case, such that the critical Mach number is increased from 0.55 to 0.57. This is a slight change in critical Mach number;

however, note that a downstream fairing, similar to the one studied in Chapter 2, could also be added to increase the critical Mach number still further. Also, note that the virtual duct shape chosen was not optimized and that the pressure distribution indicates that the diffusing part of the virtual duct for this fence design has very little effect and could have been better designed. The diffusing part of virtual duct has a strong effect on the maximum flow speed, and hence critical Mach number. Optimization of the virtual duct shape will be looked at in more detail in Chapter 5.

Despite the lack of optimization of the diffusing part of the virtual duct, Figure 3.6 shows that the virtual duct still has a significant, beneficial effect on the aft pressure distribution on the turret. Specifically, the smaller adverse pressure gradient between

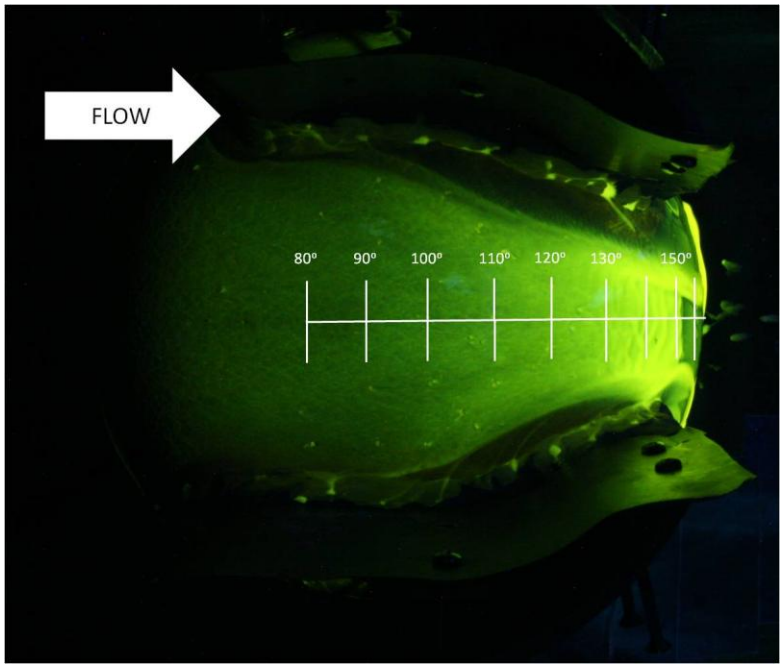

Figure 3.5. Flow through low-curvature virtual duct showing attachment up to an elevation angle of 150°.

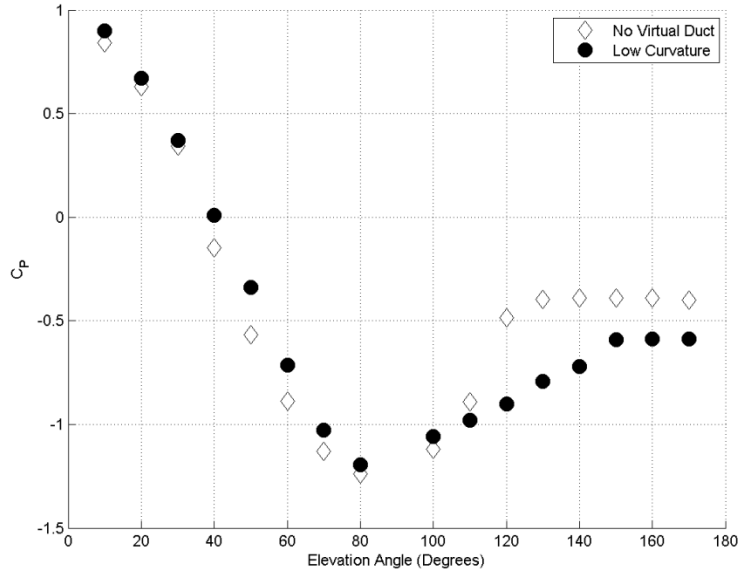

Figure 3.6. Pressure distribution for flow through the low-curvature virtual duct configuration shown in Figure 3.5, compared to a turret without a fence.

90° to 150° shows that the virtual duct successfully decreases the adverse pressure gradient on the rear of the turret. The result is that the low-curvature virtual duct delays boundary-layer separation to an elevation angle of around 150°; the pressure distribution supports this by showing a constant pressure region downstream of 150°, indicating a separation in this region. Overall, the delayed boundary-layer separation for the low-curvature virtual duct would significantly improve the aft field of regard of the turret. The same data in Figure 3.6 is shown in Appendix A displaying the 95% confidence intervals.

3.3.2 Virtual Ducts with Medium and High Curvature

Investigations were also performed on virtual ducts with higher-curvatures: a "medium-curvature" virtual duct with a 0.138 meter radius of curvature and a maximum displacement of the center of the virtual duct fence of 0.17 meters, and a "high-curvature" virtual duct with a 0.099 meter radius of curvature and a maximum displacement of the center of the virtual duct fence of 0.19 meters. These configurations were identical to the low-curvature duct except for the amount of curvature of the center region of the virtual duct. The oil-flow data for a medium-curvature configuration is shown in Figure 3.7 and a high-curvature configuration is shown in Figure 3.8. The oil-flow data for the medium- and high-curvature ducts show that these ducts also delay boundary-layer separation on the turret surface. However, the figures also show that the oil-flow data for the medium- and high-curvature ducts are increasingly dominated by an oil-free zone next to the walls of the virtual duct. Initially, it was hypothesized that this oil-free region was associated with the formation of necklace vortices at the leading-edge of the virtual-duct fences. Necklace vortices are produced by the interaction of a boundary layer with a perpendicular obstruction; for example, it is well known from hemisphere-on-cylindrical turret studies (Gordeyev 2010) that necklace vortices form at the interface between the cylinder and turret ground plane, see Figure 1.9. Evidence of the presence of necklace vortices is shown by the oil-free zones at the leading edges of the virtual-duct fences (circled in Figure 3.8).

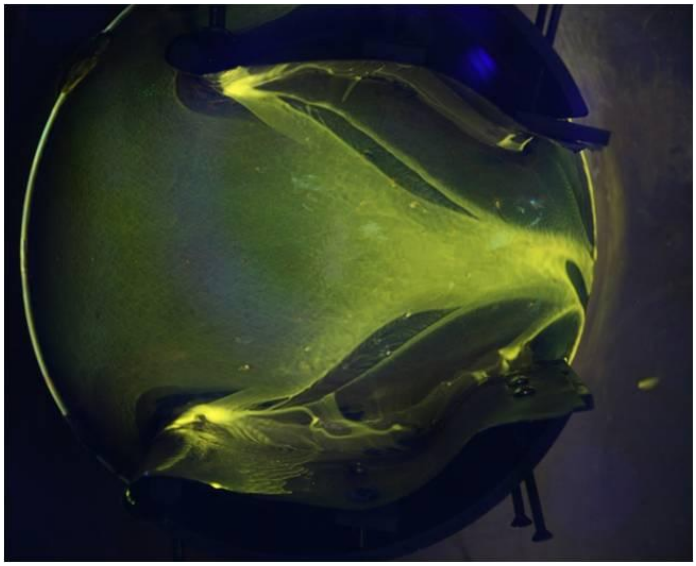

Figure 3.7. Medium-curvature virtual duct configuration.

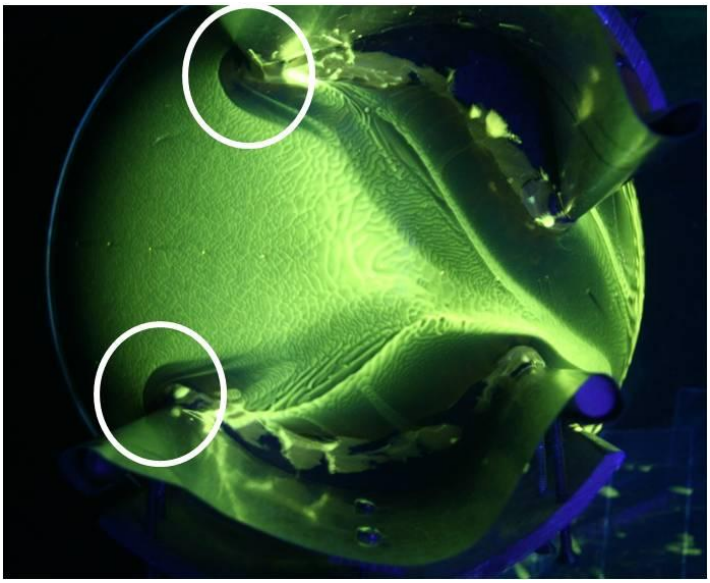

Figure 3.8. High-curvature virtual duct configuration.

In an attempt to eliminate or reduce the necklace vortices, putty was placed at the interface between the virtual-duct leading edges and the surface of the hemispherical turret, in order to more smoothly guide the flow into the virtual duct (the dark regions at the front of the virtual-duct fences in Figure 3.5 and Figure 3.7 are the putty that was placed in these regions). Despite the addition of the putty, Figure 3.5 and Figure 3.7 still show large regions that are clear of oil next to the inner surfaces of the virtual duct. As will be shown later, these clear regions are actually caused by secondary vortices that are produced by the curvature of the duct. Since these vortices have such a noticeable effect on the flow within the virtual duct as the duct curvature increases, the following chapter is devoted to detailed investigation of the cause, strength and effect of these vortices.

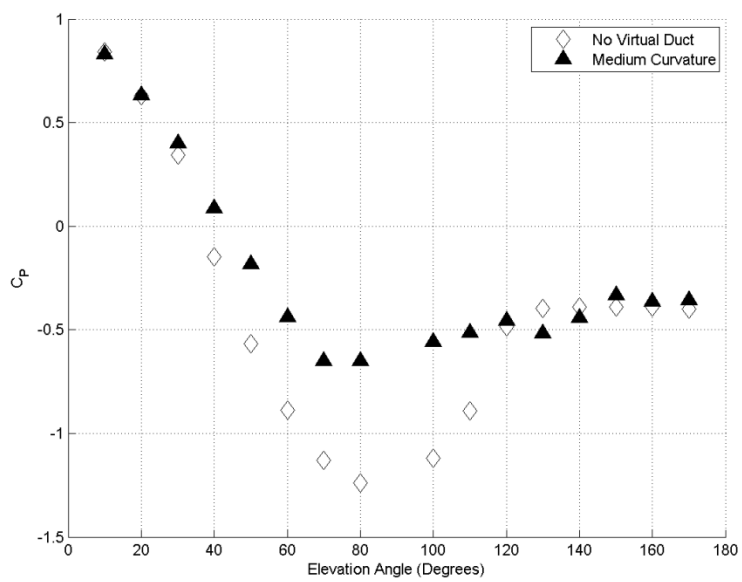

Figure 3.9. Pressure distribution for flow through the medium-curvature virtual duct configuration shown in Figure 3.7, compared to a turret without a fence.

In addition to the flow-visualization data, a pressure distribution was also measured for the medium-curvature virtual duct, Figure 3.9. This figure also shows that the medium-curvature virtual duct increases the critical Mach number and delays boundary-layer separation on the turret, similar to the low-curvature virtual duct. For this case, the critical Mach number is raised to 0.66; however, as noted earlier, it is expected that the critical Mach number could be further increased by adding a downstream fairing, similar to the one studied in Chapter 2, and by optimizing the shape of the virtual duct.

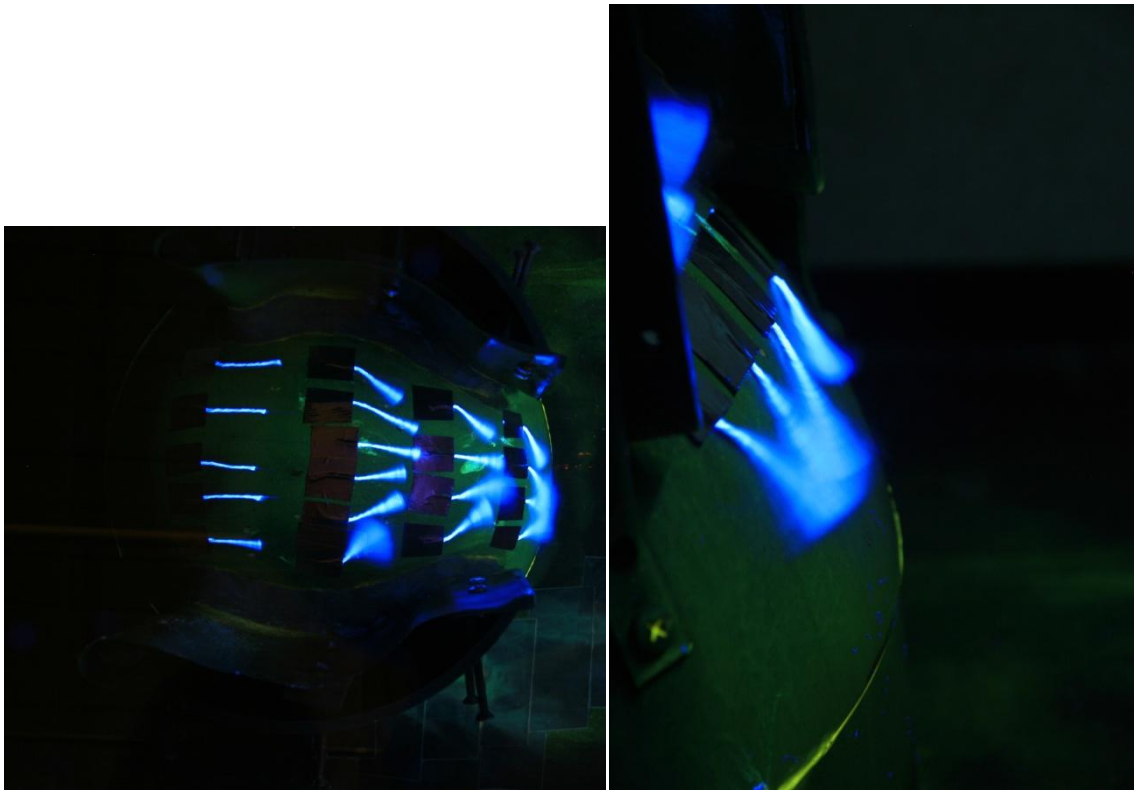

Figure 3.10. Picture of tufts attached to turret from the top (left) and a close up side view of the last row of tufts (right), flow is from left to right.

3.4 Tuft Study

As shown in Figure 3.10, tufts were also attached to the surface of the turret to visualize the flow through the virtual duct. The tufts consisted of roughly 0.013 m (0.5 inch) pieces of yarn taped to the surface of the hemisphere with tape. This was performed for the medium-curvature virtual duct configuration only. The tufts were illuminated using a black light, and the exposure time of the camera was selected to show the fluctuations of the tufts. A slightly blurry image means the tuft is moving back and forth, indicating large fluctuations in the flow, while a less blurry tuft image means the flow has fewer fluctuations. The first row of tufts does not move and appear stationary, indicating that the flow has small fluctuations at this location. Further downstream, the tufts nearest the fence (top and bottom tufts in Figure 3.10 (left)) appear to fluctuate while the inner tufts continue to stay stationary, showing the effect of the streamwise vortices that occur in the corner regions between the spherical turret surface and virtual-duct fences; the fact that the centerline tufts at this location are stationary shows that the flow on the centerline is not directly influenced by these secondary structures. From the top view, the furthest downstream row of tufts appear blurry, but a side view of these tufts, Figure 3.10 (right), shows that this is a side-to-side fluctuation, and not due to the flow separating in this region. Therefore the flow structures near the fence seem to continue through the outlet of the fence, but stay attached to the surface of the turret. The last row of tufts begins at an elevation angle of 150° and continues for roughly another 10°. These tufts show flow attachment through

the outlet of the fence up to an elevation angle of 150°, a significant improvement on the elevation angle of 120° for the flow without a virtual duct attached.

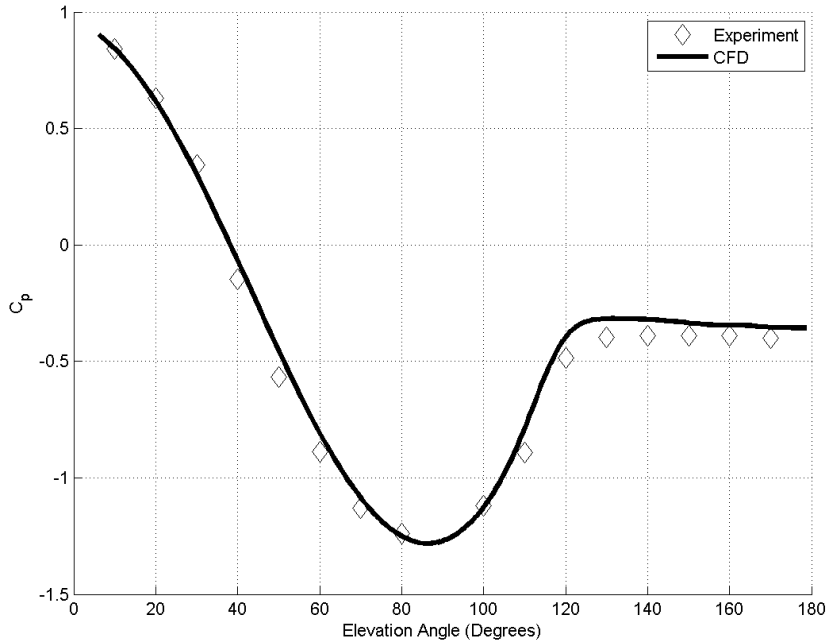

Figure 3.11. Comparison of DES CFD (solid line) and experimental (diamonds) pressure distribution for flow over a hemisphere-on-cylinder turret.

3.5 CFD Computations of Virtual Duct on Hemisphere-on-Cylinder Turret

The ability to model the effect of the virtual duct using computational fluid dynamics (CFD) was also tested; as will be shown in the following chapters, CFD was used to further investigate the design space and in optimization studies. All CFD calculations shown in this section were completed using a detached-eddy simulation (DES) algorithm to correctly capture the flowfield inside of the virtual duct; more discussion of the CFD approach is presented in the next chapter. The CFD was

completed using FLUENT at a flowspeed of 34.3 m/s (Re_D = 6.8 x 10^5). The CFD computations were time resolved, and were run for 2 flow clearing times, that is, for a total time that allowed for the air to flow through the full domain 2 times. The domain consisted of an inlet region that is 5 ball diameters long and an outlet region that is 10 ball diameters long. The inlet and outlet were defined as pressure farfield and the bottom wall and model is set as a no-slip wall.

3.5.1 Hemisphere-on-Cylinder Turret

This first CFD run was completed for a hemisphere-on-cylinder turret only. In order to correctly capture the flow over the turret, the necklace vortex that forms between the cylinder and the incoming plane needs to be modeled correctly, therefore

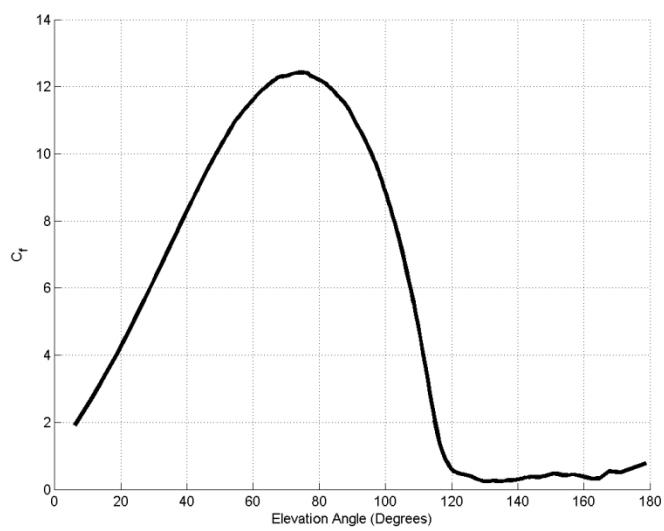

Figure 3.12. Magnitude of skin friction for for flow over a hemisphere-on-cylinder turret computed using the DES solver showing flow separation around an elevation angle of 120°.

there needs to be an inlet region that allows for the boundary layer to grow enough to produce the necklace vortex. To validate the experiment, a comparison of the centerline pressure distribution is compared to the experimental pressure distribution, shown in Figure 3.11. The pressure distribution matches the minimum C_{P0} of -1.25 and also shows separation around an elevation angle of 120°. This comparison is similar to the pressure distributions for flow over a turret as shown earlier in Figure 1.7.

In order to compare the location of flow separation, a look at the skin friction on the surface of the sphere is a good indication of when separation occurs. Figure 3.12 shows the magnitude of the skin friction as a function of elevation angle showing flow separation occurring at around 120°, which is similar to the oil-flow visualization shown in Figure 3.3. The combination of the C_{P0} and skin friction distributions over a turret show that the CFD can capture the flow features for flow over a Hemisphere-on-Cylinder Turret.

3.5.2 CFD Study of Low-Curvature Virtual Duct

To evaluate the ability to model the virtual duct using CFD, a CFD study was completed for the same low-curvature virtual-duct configuration that was investigated experimentally and shown in Figure 3.5. Since the experimental fence shape was produced by moving screws in and out of the mounting plate on the turret, the fence shapes of the low-curvature virtual duct may have slight irregularities that are not modeled correctly in the CFD. To determine the fence shape for the CFD modeling, the

experimental fence shape was traced onto a piece of paper that was placed over the top of the fences.

Figure 3.13 shows a comparison of the low-curvature pressure distribution found experimentally and computationally. The CFD-computed pressure distribution shows good agreement with experiment and appears to show attached flow up to the same elevation angle as the experiment, approximately 150°. The main discrepancy between the two pressure distributions in Figure 3.13 is that the CFD predicts a higher C_p than the experiment between an elevation angle of approximately 100° and 130°. One possible explanation for this discrepancy is that the CFD may not accurately reproduce viscous effects that may introduce additional blockage and hence speed up the flow in this region of the virtual duct. Nonetheless, despite this discrepancy, the CFD still accurately

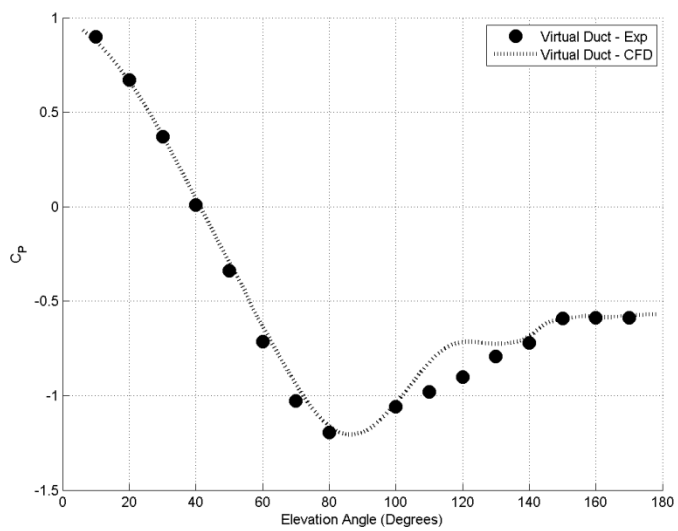

Figure 3.13. Experimental pressure distribution (circles) compared to a DES of the same geometry (dotted line) for the low-curvature fence.

predicts the separation location. The CFD shows attached flow up to an elevation angle of 148°, based on the skin friction shown in Figure 3.14, which is similar to the 150° shown in the wind tunnel test, Figure 3.5. Overall, Figures 3.13 and 3.14 indicate that the flow can be reasonably-well modeled using a DES solver, especially in regards to determining the minimum pressure and the separation location.

3.6 Concluding Remarks

In the previous chapter, the ability of the virtual duct to increase the critical Mach number of a spherical turret was demonstrated; however, the ability to delay boundary-layer separation was less clear due to the low Reynolds number of the pod-model tests, and because of the influence of the downstream fairing. An objective of this chapter was therefore to more-rigorously test the ability of the virtual duct to delay boundary-layer separation on the surface of a spherical turret. As verified by the pressure-distribution and flow-visualization results for the baseline turret, the hemisphere-on-cylindrical-base turret tests shown in this chapter were performed at a sufficiently-high Reynolds numbers to attain turbulent boundary-layer flow on the surface of the turret model. As such, the results of this chapter give a good indication of how the virtual duct would influence the turret boundary layer at the high Reynolds numbers that would exist on an actual system.

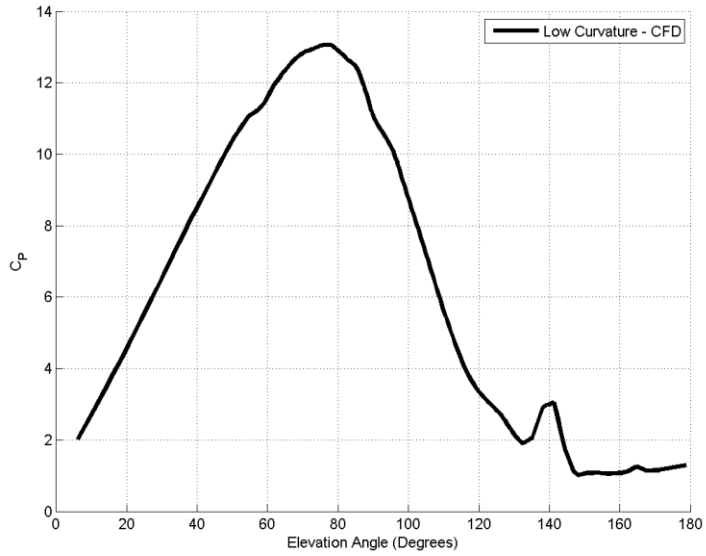

Figure 3.14. Skin friction on the surface of the low-curvature virtual duct found using CFD.

Virtual ducts with low, medium, and high curvatures were tested in this chapter and show that the virtual duct can delay separation on the turret to at least an elevation angle of 150°. However, for all configurations, the turret surface near the walls of the virtual duct was observed to be clear of oil, such that these clear regions effectively dominated the oil-flow visualizations for the medium- and high-curvature virtual duct cases. As will be shown in the next chapter, these clear regions are produced by a streamwise vortex that forms in the corner between the virtual duct walls and the surface of the turret. The next chapter describes an investigation into these streamwise vortices and the development of a methodology to predict their strength and optical effect.

CHAPTER 4:

SECONDARY FLOW EFFECTS IN THE VIRTUAL DUCT

4.1 Introduction

As shown by the surface near the walls of the virtual duct being clear of oil in the flow visualization data, Figures 3.5, 3.7 and 3.8, there is a secondary flow effect occurring in this region. This chapter presents an investigation into the cause of this flow feature. Furthermore, a model for the flow in the corner regions of the virtual duct is developed, as well as an estimation for its aero-optic effect.

Figure 4.1. Photograph of wind-tunnel model used in PIV tests. Flow is from left to right.

4.2 Particle Image Velocimetry (PIV) Study

A Particle Image Velocimetry (PIV) study was performed to investigate the nature of the flow in the corners of the virtual duct. For this study, a model of one fence of a virtual duct was constructed that was 0.229 meters long (9 inches) and 0.127 meters high (5 inches). This fence was mounted on a flat ground plane next to the window in one of the 2 foot x 2 foot low-speed wind tunnels at the University of Notre Dame, see Figure 4.1. With this mounting arrangement, the window of the wind tunnel behaved as a reflection plane for the flow, thereby allowing a much larger model to be used, and it also facilitated detailed PIV measurements of the flow in the corner of the model fence. As shown in Figure 4.2, the PIV laser sheet was generated more or less perpendicularly to the flow direction near the exit of the virtual-duct model, and the camera was pointed through the window at close to 90° to the laser sheet; the exact angle between the laser sheet and the camera direction was measured and used to correct the PIV velocity data.

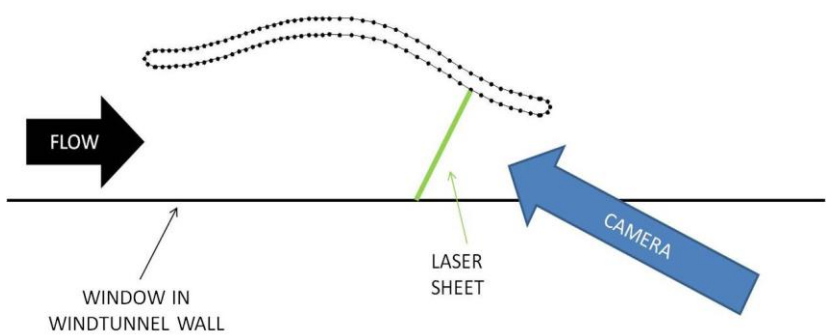

Figure 4.2. Set-up of PIV configuration to experimentally measure the secondary vortex.

The virtual-duct model shown in Figure 4.1 was mounted on a splitter plate where the leading edge of the splitter plate was at the same location as the leading-edge of the model; as such the size of the boundary layer at the leading edge of the virtual-duct model was negligible so that no necklace vortex formed on the model. As noted above, the tests were performed on a flat surface rather than on a spherical surface as would be the case for the actual deployment of a virtual duct. This was done because the planar floor significantly simplifies the experimental arrangement by eliminating problems with dark regions and reflections of the PIV laser sheet, alignment of the PIV system, etc., that would exist if the measurements were made on a spherically-shaped turret, and it was hypothesized that the planar-floor arrangement would still produce the essential flow features in the corner of the virtual-duct model. The tests were performed at a flow speed of 34.3 m/s, giving a Reynolds number based on the model length of 5.2 x 10^5; this Reynolds number is only slightly lower than the Reynolds number for the tests shown in Chapter 3 but higher than the pod study shown in Chapter 2.

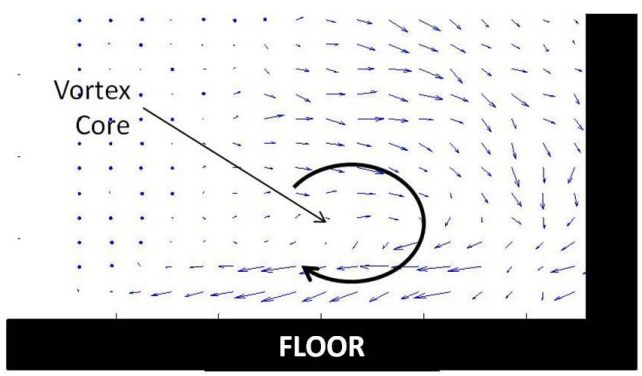

Figure 4.3. Velocity vectors on the fence found using PIV.

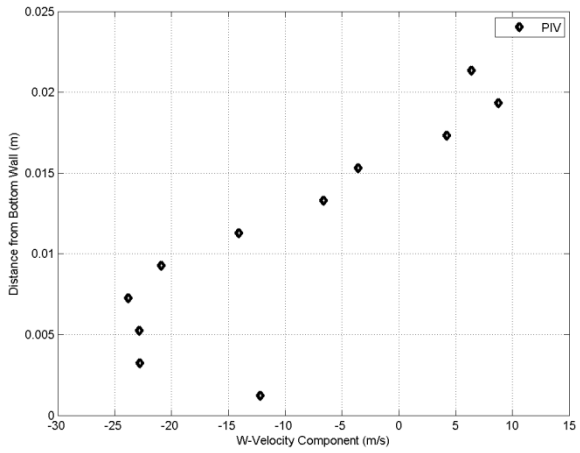

Figure 4.4. Comparison of the velocity profile through the vortex core from the bottom of the wall for the CFD and PIV data.

Figure 4.3 shows the PIV velocity vectors in the corner region of the virtual-duct model, where the virtual duct fence is on the right side of the picture and the ground-plane floor is on the bottom. The figure clearly shows that a vortex exists in the virtual-duct corner, with a clockwise rotation (when viewed from downstream as shown in Figure 4.3). The velocity profile of the vortex, taken from the PIV data for a cut approximately through the vortex center, is plotted in Figure 4.4, and also clearly shows the vortical nature of the flow. This vortex is created by the outward movement of the bulk flow near the top of the measurement region and inward motion of the flow near the floor. The fastest flow is near the floor as the fluid moves inward towards the center of the virtual duct, away from the virtual-duct wall. As such, the clear regions next to the virtual-duct walls in the oil-flow visualizations shown in Chapter 3 are caused by a sweeping of the oil away from the walls by this high-speed flow near the surface of the turret. The PIV data therefore clearly shows the existence of a vortex in the corner of

the virtual-duct wall; in the next sections of this chapter, an explanation for the physics as well as a model for this vortical flow is presented.

4.3 Curved Open-Channel Flow

Due to the unusual shape of the turret with virtual duct, there is nothing in the literature that deals specifically with a configuration like this. However, similar flow physics to the virtual duct are exhibited by the curved open-channel flow that is observed in meandering rivers, Figure 4.5.

Curved open-channel flow has been studied extensively since the late 1800s due to its application to meandering rivers and the erosion of areas around curved bends. The existence of a vortical structure in the flow was first identified by Thomson (1876)

Figure 4.5. Aerial view of the Charley River at Yukon, Alaska. Credits to Tim Brabets, U.S. Geological Survey (Van Balen 2010).

when he noticed that sediments on the bottom of a riverbend were being moved from the outer part toward the inner part of the riverbend. The inward motion of the water at the bottom of the river along with an outward motion at the surface of the river produces this vortical structure. Rozovskii (1957) explained the generation of this vortical structure in terms of the local imbalance between the driving centrifugal force and the transverse pressure gradient. Due to the boundary layer at the bottom of the river, the bulk flow moves outward more easily than the flow near the bottom surface. Due to conservation of mass, other fluid must return to the inward portion of the river to replace this outward-going flow, and thus the vortex is produced by an inward flow near the bottom of the riverbed. Depending on the speed of the fluid, which in the virtual-duct's case is large, a second vortical structure can also appear in curved open channel flow. This second smaller cell is referred to as the outer bank cell, or secondary flow cell, due to its existence on the outer wall of the curved channel. A schematic of the 2 vortices is shown in Figure 4.6.

4.3.1 Implications to Virtual-Duct Performance and Organization of this Chapter

Comparison of Figure 4.6 with the PIV data in Figure 4.3 shows that the vortices that form in the corners of the virtual duct share the same basic flow physics as the vortical structures observed in curved open-channel flow. In effect, the virtual duct can be considered as two curved channels, where each wall of the virtual duct represents the outer bank of the river in Figure 4.6.

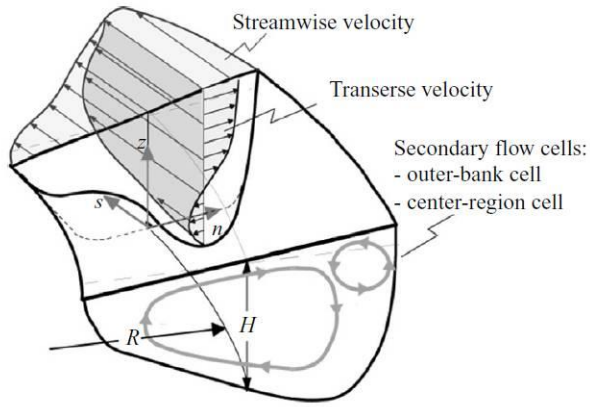

Figure 4.6. General Schematic of flow through a curved channel
(Van Balen 2010)

The existence of these corner vortices has important implications on the performance of the virtual duct. First, the corner vortices will have some kind of fluid-mechanic effect on the flow within the duct, in the sense that the vortices can be expected to induce local velocities that could affect, for example, boundary-layer separation in the duct or on the turret, or the maximum flow speed and hence critical Mach number within the virtual duct. Pressure-distribution and flow-visualization data shown in Chapter 3 did not show, however, any detrimental effect of the corner vortices on either the location of boundary-layer separation or the critical Mach number of the turret. For example, the flow-visualization data in Chapter 3 showed very similar locations for boundary-layer separation for different virtual-duct curvatures, at least up to the point at which the curvature was so large that the two corner vortices covered the entire downstream face of the turret (i.e. Figure 3.8).

More importantly, as shown in Porter (2010), streamwise tip vortices like the corner vortices produced by the virtual duct can in and of themselves produce aero-optic aberrations. As explained in Porter (2010), these aero-optic aberrations originate from the low-pressure, and hence reduced density, within the cores of the vortices. Since, as shown by the flow-visualization data in Figures 3.5, 3.7 and 3.8, the virtual-duct corner vortices would pass directly over an optical aperture on the surface of the turret, the question therefore arises as to what kind of optical aberration these vortices would present to the outgoing beam.

The remainder of this chapter therefore presents an investigation into the optical effect of the virtual-duct corner vortices. Since these vortices cover progressively more of the surface of the turret as the curvature of the duct wall increases, the aero-optic effect of the vortices has significant impact on the overall effectiveness of the virtual-duct concept. The chapter is organized as follows: first, previous work on modeling curved open-channel flow is reviewed and presented. This model is then validated for the virtual-duct configuration; due to the difficulty in experimentally measuring the flow within the virtual duct, much of this validation is performed using CFD studies. This is done by first comparing the CFD to the simplified experiments performed using the virtual-duct model mounted on a flat ground plane (i.e. Figure 4.4). Once the CFD approach is established that matches this simplified configuration, then additional CFD computations are shown for the more-complex configuration of the virtual duct mounted on a spherical turret. Finally, the validated model for the corner vortices is used with the results of previous investigations into the aero-optic effect of

tip vortices (Porter 2011b) to develop predictions for the aero-optic effect that the corner vortices would have on an outgoing beam.

4.4 Validation of Computational Approach

Numerous computational studies (Booij 2003; Constantinescu 2011; Kashyap 2012; Stoesser 2010; Van Balen 2009) have been performed into open-channel flow and show general agreement with experimental studies (Blanckaert 1999; Blanckaert 2004; Booij 2003; Hille 1985; Van Balen 2009). A common observation from the computational studies is the need for an advanced turbulence model, capable of accurately resolving turbulence anisotropy effects and the kinetic energy transfer between the mean flow and turbulence in order to capture the velocity redistribution (Constantinescu 2011).

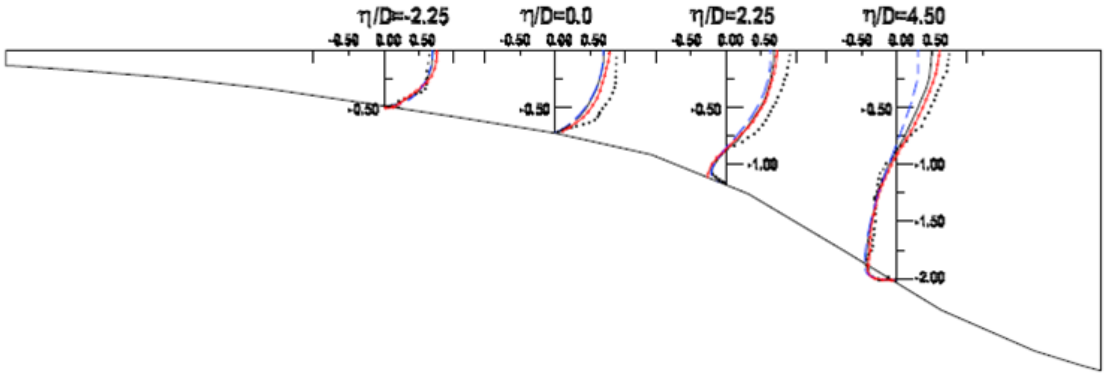

Figure 4.7. Comparison of measured (black circles), RANS- (dashed blue line), DES- (red line), and LES-computed (solid black line) velocity profiles of the non-dimensional transverse velocity in an open-channel flow. The outer wall is on the right (Constantinescu 2011).

An example of an investigation into computational modeling of open-channel flows is presented in Constantinescu (2011), which shows a comparison of DES, LES, and RANS CFD with experimental data. Figure 4.7 shows a comparison of the velocity profiles of the transverse velocity at the 60 degree location of the channel bend. Looking at the outer profile, the profile furthest to the right in Figure 4.7, DES shows a closer level of agreement with the experiment when compared to RANS. In fact, comparisons of the strength of the cross flow motions in relevant cross sections showed that the circulation of the main cell was consistently and significantly under predicted by RANS compared to DES (Constantinescu 2011).

Other studies by Booij (2003) and Stoesser (2010) also compare RANS solutions to DES and LES solutions and arrive at a similar conclusion that RANS turbulence models do not capture the anisotropy effects needed to correctly model the flow in a curved channel. Booij (2003) states that RANS computations can produce the main characteristics of the main flow and the secondary flow in curved flows; however, RANS fails to give satisfactory reproductions of the complicated secondary flowfields in the channel. Although a well-resolved LES would give the best solution, it is too computationally expensive to simulate the flow at high Reynolds numbers (Constantinescu 2011). As such, DES was selected as the preferred solver for CFD investigations of open-channel flows in this research, due to its satisfactory accuracy and reduced computational expense compared to LES.

4.4.1 DES Modeling of PIV Experiment

Based on the preceding discussion, CFD modeling of the flow in the virtual duct was performed using a DES solver. All computations were completed using the commercial CFD program, Fluent, using 2nd-order accuracy and the unsteady, pressure-based solver. The DES solver that was employed used the SST k-ω RANS model near the solid walls. The grid was fully structured and had an initial height away from the no-slip walls that corresponded to y+ less than 1, which is typically considered sufficient resolution for the computations in the boundary layer.

To validate the ability of this DES approach to model the flow in a virtual duct, a DES run was first performed for the exact experimental geometry of the PIV

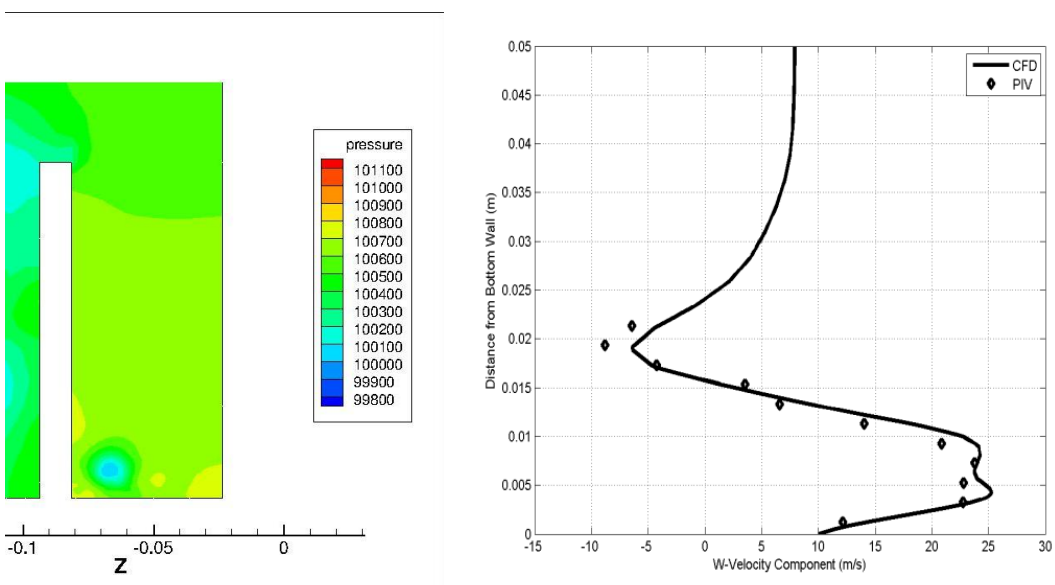

Figure 4.8.(Left) CFD run of PIV set-up showing the formation of the vortex near the wall of the fence. (Right) Comparison of the velocity profile through the vortex core from the bottom of the wall for the CFD and PIV data.

measurements shown in Section 4.2. The computational mesh used for this validation test consisted of roughly 1.6 million cells. Figure 4.8, Left, shows the DES-computed pressure distribution in a cross section of the virtual duct, viewing in the flow direction with the virtual duct fence shown in the left portion of the figure; the figure clearly shows the existence of a low-pressure region associated with the core of the vortex located just to the right of the virtual-duct wall. To better compare the DES to the PIV results, Figure 4.8, Right, shows the DES-computed velocity distribution through the core of the vortex overlayed on the velocity distribution measured in the PIV tests and shown previously in Figure 4.4. Figure 4.8, Right, shows that the DES-computed velocity distribution matches the measured velocity distribution almost exactly. In fact, near the bottom wall region, the DES also captures the boundary layer that was measured in the PIV test; this boundary layer forms due to the no-slip condition on the planar floor and the strong inward flow away from the virtual duct wall. More importantly, the DES captures the velocity profile of the vortex, and accurately models both the core radius and the circulation of the experimentally-measured corner vortex. Overall, the close agreement between the DES-computed and experimentally-measured velocities in the corner vortex shows that the DES solver can be used to model with reasonable accuracy the formation and properties of the corner vortex in the virtual duct.

4.5 DES Modeling of Virtual Duct

The DES approach validated in the previous section was next applied to the regular spherical-turret-with-virtual-duct configuration. For these computations, the

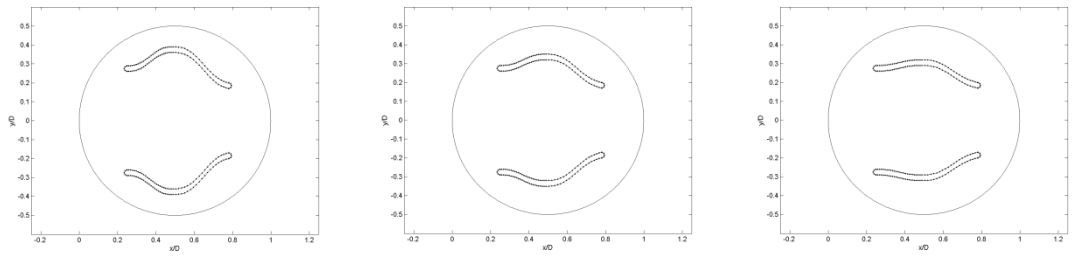

Figure 4.9. Virtual duct wall shapes computed using DES. The wall radii are, from left to right, 0.099, 0.120, and 0.166 meters.

DES model used the same computational parameters described before, specifically, the computations were performed using the DES solver in Fluent, using a fully-structured grid with y+ on the surface of the hemisphere of 1 or less. For all of the models, the Reynolds number, based on the diameter of the turret, of the computations was around 6.8×10^5, which matches the experimental tests in Chapter 3 and is large enough so that the boundary layer over the turret was turbulent.

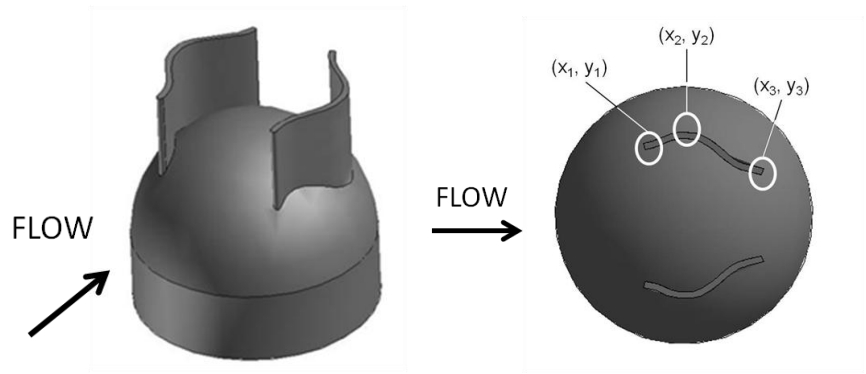

Figure 4.10. Isometric (left) and plan (right) view of turret with flow in positive x-direction. The fence is defined by 3 points.

The computations were performed for 3 different virtual duct wall radii, R = 0.099, 0.120, and 0.166 m, which are different from the virtual-duct shapes that were experimentally tested in the previous chapter, but are still able to show the effect of changes in virtual-duct curvature radius. A top view of each fence shape is shown in Figure 4.9. The fence wall coordinates were determined using fifth-order polynomials

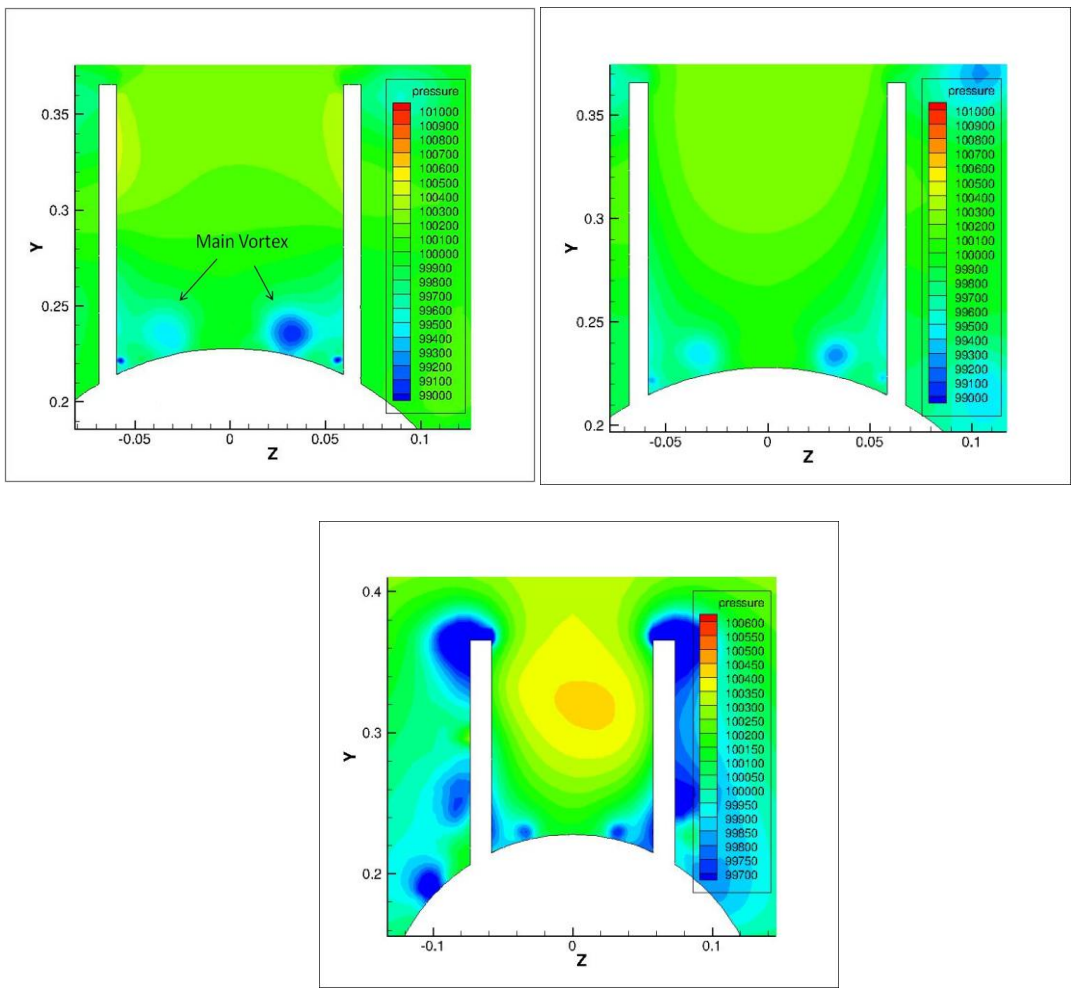

Figure 4.11. DES-computed crossplane pressure distribution inside virtual ducts with R = 0.099 (top left), R = 0.120 (top right) and R = 0.166 (bottom) m. Note that the highest curvature duct (top left) produces the strongest vortex core with the lowest pressure. Note the change in legend values for the bottom figure.

for both the diffusing and contracting sections:

$$y_d = a_d + b_d x + c_d x^2 + d_d x^3 + e_d x^4 + f_d x^5 \text{ and}$$
$$y_c = a_c + b_c x + c_c x^2 + d_c x^3 + e_c x^4 + f_c x^5 \,. \tag{4.1}$$

The six constants *a, b, c*, *d*, *e*, and *f* for each section were determined by the six boundary conditions consisting of the chosen starting and ending azimuthal locations of the fence, plus zero slope and curvature at the start and end of each section of the fence. As such, a unique fence shape can be defined by choosing the locations of three points on the fence, consisting of the leading- and trailing-edge points and the point of maximum diffusion of the fence, that is, the points 1, 2, and 3 as shown in Figure 4.10. The effective radii of the virtual ducts were determined by superposing a circle on the

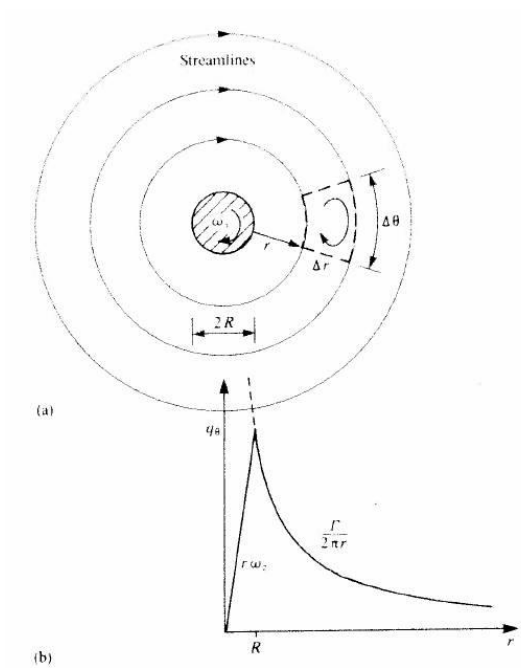

Figure 4.12. Two-dimensional flowfield around a cylindrical core rotating as a rigid body (Katz 1991).

three points, and determining the radius of this circle; as shown below, the effective radii computed in this way provides a single parameter for the virtual-duct curvature that can be related to the global performance of the virtual duct.

Figure 4.11 shows computed pressure distributions in the virtual ducts for the three computational models. The figure clearly shows the existence of vortices in the corners of the virtual ducts. The 3 CFD calculations also show that as the radius of curvature of the fence decreases, the strength of the vortex increases.

As will be shown below, the key parameters that determine the aero-optic effect of a tip vortex are the circulation of the vortex and the core radius of the vortex. These two parameters were determined from the DES-computed results for each of the 3 virtual-duct models. Specifically, vortex flowfields typically vary as $\Gamma/2\pi r_c$, with a viscous core that exhibits a linear velocity change between the peak rotational velocities, Figure 4.12 (Katz, 1991). As such, the core radius was determined as one half

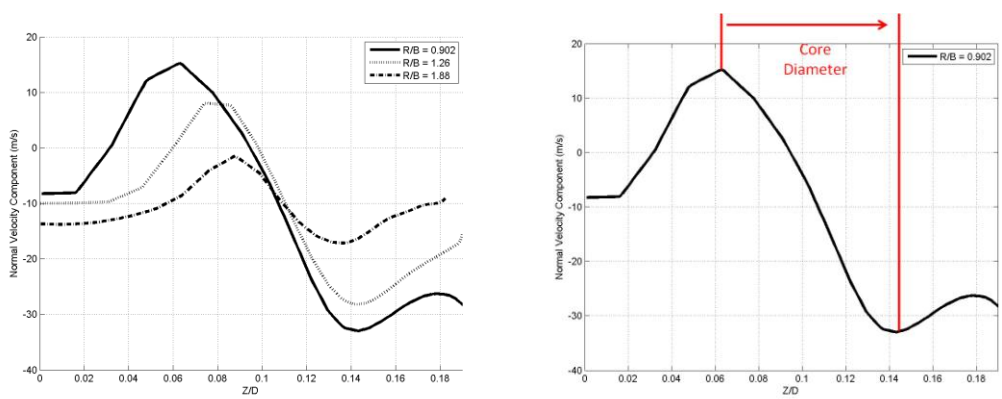

Figure 4.13. Left, Tangential velocity through vortex core on a virtual duct for varying curvature ratios. Right, Tangential velocity through vortex core for smallest curvature ratio showing the core diameter.

the distance between the points of maximum tangential velocity in the vortex. As an example, Figure 4.13 right shows the tangential velocity through the vortex core for the lowest radius of curvature case, R = 0.099 m. The viscous core is shown in Figure 4.13 between the minimum and maximum tangential velocities. The core radius, r_c, was found to be 0.0403D (12.3 mm). Once the core radius was determined, the circulation was computed using:

$$\Gamma = -\oint V \cdot ds \,, \tag{4.2}$$

where v is the velocity along the path of the closed integral taken around the core radius (i.e. outside of the inner viscous core).

Figure 4.14 shows how the core radius and circulations computed using DES CFD varies with the radius of the virtual duct. The figure shows that both the circulation and the core radius increase as the duct radius decreases. Based on the physical explanation for the cause of the corner vortices (see Figure 4.6), the results of Figure 4.14 make

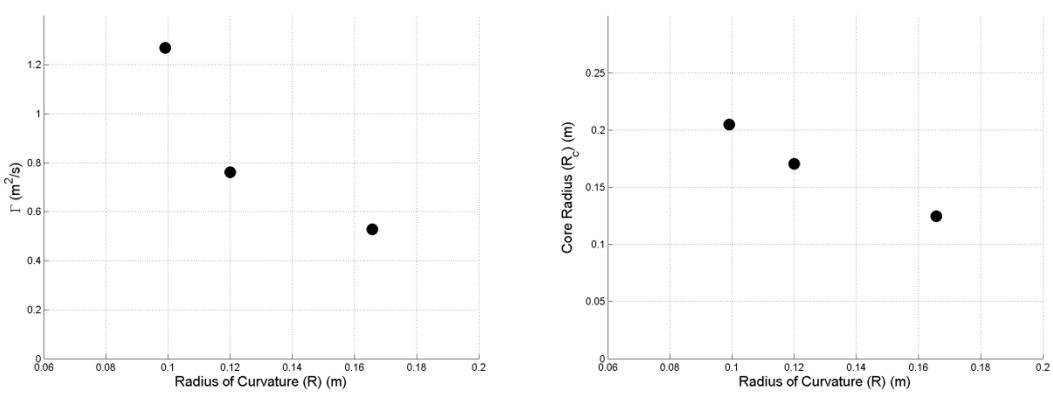

Figure 4.14. DES solutions for the circulation (left) and core radius (right) of corner vortices for flow over a turret with different virtual-duct radii.

sense in that a higher curvature of the virtual duct (i.e. smaller radius of curvature) would produce greater motion of the bulk flow to the outside of the duct resulting in a stronger vortex.

4.6 Scaling of Corner Vortex Parameters

4.6.1 Open-Channel Flow Studies

As mentioned above, previous studies into the flow in curved open channels have been primarily concerned with the flow in water channels, including streams and rivers. An example of a study of the circulation of the streamwise vortex in curved open-channel flow was completed by Kashyap (2012), who investigated the circulation strength of the vortex in water channels of different curvature ratios; a typical geometry investigated by Kashyap is shown in Figure 4.15. For his investigation, Kashyap defined a nondimensional curvature ratio, R/B, as the ratio of the radius of the curvature of the bend, R, to the width of the bend, B. Kashyap looked at five curvature ratios using a CFD simulation (R/B = 1.5, 3.0, 5.0, 8.0, and 10.0) and compared it with one curvature ratio that was tested experimentally. The CFD simulations were completed using a steady finite-volume 3D RANS viscous solver with a standard Reynolds Stress Model (RSM) closure. The RSM model was used because it can account for the turbulence anisotropy discussed above (Kashyap 2012).

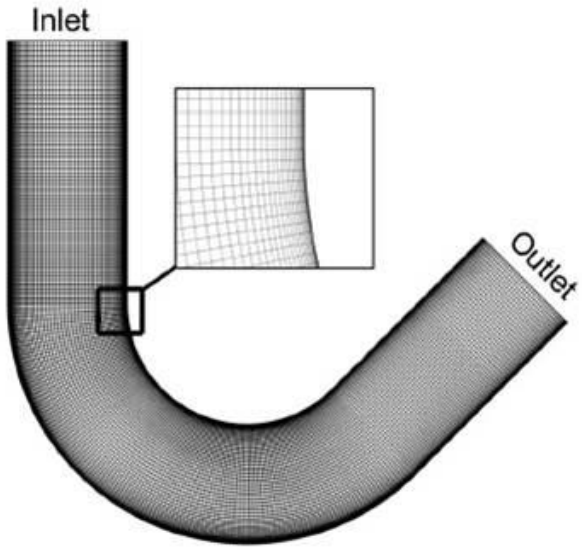

Figure 4.15. View of mesh and geometry of the curved channel studied in Kashyap (2012). This configuration has is an R/B of 1.5.

Figure 4.16 shows streamline patterns (left) and streamwise velocity, u/U (right) for 3 different cross sections tested computationally; these figures show that the CFD successfully reproduced the streamwise vortices. More importantly, Figure 4.17 shows the circulation compared to the curvature ratio of the bend. From Figure 4.17, it is noted that as the curvature ratio increases (i.e. the bend becomes more gradual) the strength of the vortex produced is smaller. This trend matches qualitatively the DES results for the virtual duct shown in the previous section. It also matches the experimental flow-visualization results shown in Chapter 3, in the sense that as the curvature of the virtual duct increases, the vortex becomes larger and stronger as shown by the larger oil-free zones next to the virtual-duct walls.

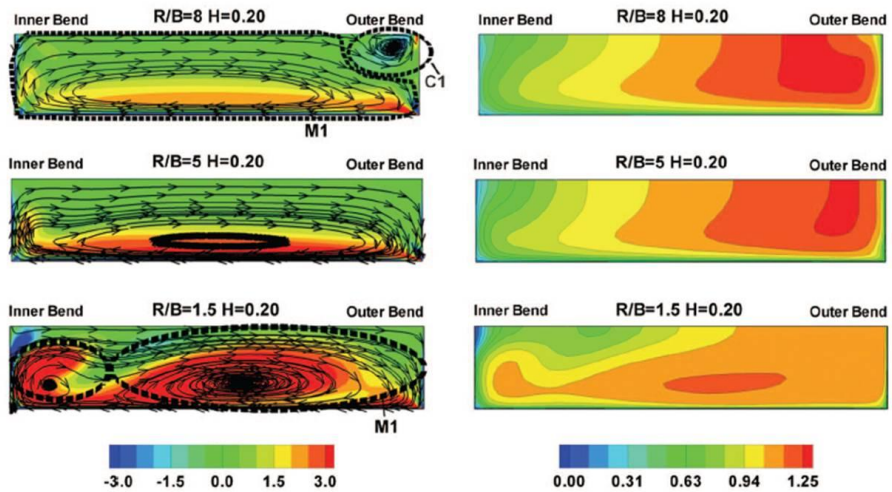

Figure 4.16. Comparison of 2D streamline patterns (left) and streamwise velocity, u/U, (right) at the 135° cross section.

4.6.2 Testing of Open-Channel Scaling Approach

Perhaps the most significant observation of Figure 4.16 and Figure 4.17 is that Kashyap nondimensionalizes the open-channel data by the flow speed and by geometric parameters only, that is, U and B.

$$\Gamma^* = \frac{\Gamma}{U \cdot B}, \tag{4.3}$$

In particular, the Reynolds number does not appear in the nondimensionalization of the open-channel data, indicating that Reynolds-number effects do not influence the strength or size of the corner vortices.

Kashyap's nondimensionalization approach was also tested for the virtual-duct-on-hemispherical-turret results computed in Section 4.5. Figure 4.18 shows the results of this nondimensionalization. The figure shows that the nondimensionalization approach successfully collapses all of the DES data for the virtual duct onto a single

curve, despite large differences in Reynolds number used in the computations. For example, Figure 4.18 (Left) shows that a virtual-duct solution at M_∞= 0.5 produces the same Γ* as the solution at M_∞ = 0.1.

Figure 4.18 (Right) also includes DES computations of the simplified virtual duct case with a flat floor; the figure shows that these data also match the scaling reasonably well. Specifically, two DES solutions for the same wall curvature were computed at two different Reynolds numbers, but at the same freestream velocity; i.e., the different Reynolds numbers were obtained by changing the viscosity of the fluid, where one computation was performed using the viscosity of air and a second used the viscosity for water. The results of these computations are shown in Figure 4.18 (Right), which shows that the two computations produce roughly the same nondimensional Γ* despite having significantly different Reynolds numbers. As such, the CFD results for the virtual

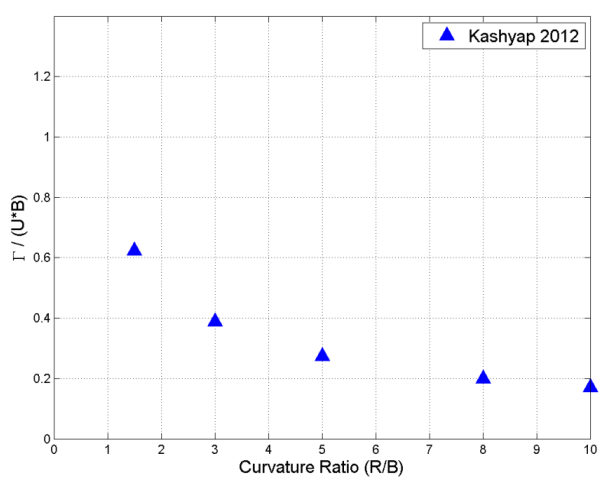

Figure 4.17. Variation of nondimensional gamma with curvature ratio for water flow in a curved channel (Kashyap, 2012).

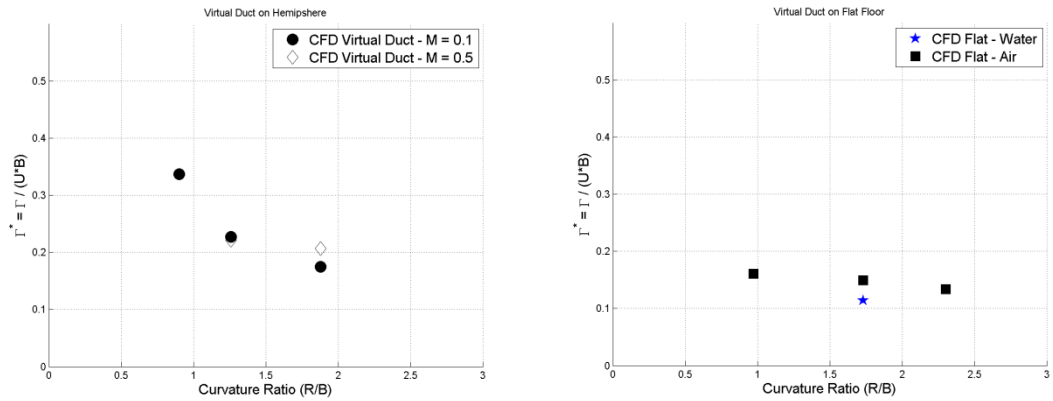

Figure 4.18. Nondimensional Gamma as a function of curvature ratio for flow through a virtual duct on a hemispherical turret (Left) and a planar floor (Right).

duct also support the finding that the corner-vortex circulation is independent of Reynolds-number effects.

A curve fit to the nondimensionalized virtual-duct data for curvature ratios between roughly 0.5 and 4 (circles in Figure 4.18 Left) is

$$\Gamma^* = \frac{\Gamma}{UB} = 0.297\left({}^{R}/_{B}\right)^{-0.890}. \tag{4.4}$$

For comparison, the virtual-duct-on-hemispherical turret results are shown on the same plot as Kashap's results for a curved channel in Figure 4.19. The figure shows that the curved channel produces noticeably larger Γ^* than the virtual duct geometry. Although only very rough comparisons between the virtual-duct and open-channel results can be made in Figure 4.19 due to the geometrical differences between the two configurations, a possible explanation for the difference is that all of the water that enters the curved channel is forced outward to produce the vortex so that all of the entering fluid contributes to the strength of the vortex. On the other hand, for the virtual duct, some

of the fluid escapes over the top of the fence, so that not all of the flow entering the duct contributes to the strength of the vortex. Nonetheless, both the river-channel and virtual-duct geometries show the same trend that the smaller the bend radius, the stronger the vortex that is produced.

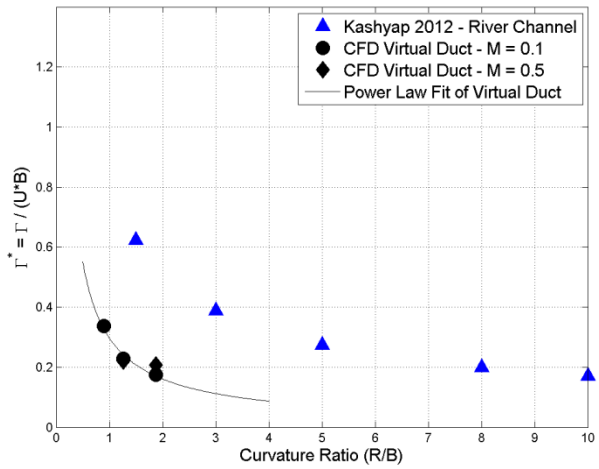

Figure 4.19. All circulation data from Kashyap (2012) and the virtual duct study.

A similar curve fit for the core radius is

$$\frac{r_c}{B} = 0.110\left({}^{R}/_{B}\right)^{-0.388}. \tag{4.5}$$

Figure 4.20 shows that, as the curvature ratio decreases, the core radius increases. Looking back to the pressure distributions inside of the virtual duct; Figure 4.11, the larger core radius is seen by the larger area of low pressure. This effect is also supported by the flow visualization study completed in Chapter 3, in the sense that when the virtual-duct curvature increases, the oil-free zones near the virtual duct fences become larger.

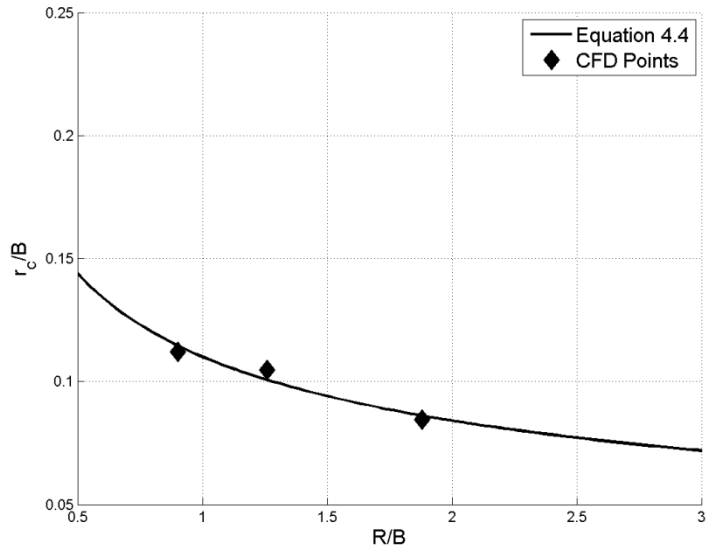

Figure 4.20. Core radius as a function of the Curvature ratio for the vortex inside of a virtual duct.

Using the nondimensional relationships shown in Equations (4.4) and (4.5), the next section shows an estimation of the optical effect of the corner vortices on a beam of light passing through the flowfield inside of a virtual duct.

4.7 Estimation of Aero-Optic Effect of Corner Vortices

A method for determining the optical effect of a tip vortex was developed by Porter (2011b). Porter showed that the density field and hence optical aberration associated with a tip-vortex flow is a function of the core radius and the circulation strength of the vortex. Note that an estimation of the optical aberration of the corner vortices could also be determined directly using the density field from the CFD results

for the turret with virtual duct; however, Porter's approach was used due to its validation against experimental optical measurements of tip-vortex flows.

Porter's approach follows the solution outlined in Bagai and Leishmen (1993), which is repeated here for completeness. Starting with the Euler equations for axisymmetric flow with no radial velocity component:

$$\frac{V_\theta^2}{r} = \frac{1}{\rho}\frac{\partial P}{\partial r}$$

$$V_Z \frac{\partial V_Z}{\partial z} = \frac{1}{\rho}\frac{\partial P}{\partial z}. \tag{4.6}$$

For tip-vortex flows, the streamwise pressure gradient is typically much smaller than the radial gradient and can be neglected. For a vortex with a Lamb-Oseen velocity profile:

$$V_\theta(r,\theta) = \frac{\Gamma}{2\pi r}\left(1 - e^{-\alpha\left(r/r_c\right)^2}\right)$$

$$V_r(r,\theta) = 0, \tag{4.7}$$

the radial component of Equation (4.6) is:

$$\frac{\Gamma^2}{4\pi^2 r^3}\left(1 - e^{-\alpha\left(r/r_c\right)^2}\right)^2 = \frac{1}{\rho}\frac{\partial P}{\partial r}. \tag{4.8}$$

For isentropic flow, the right side of Equation (4.8) can be linearized as:

$$\frac{1}{\rho}\frac{\partial P}{\partial r} = \frac{\gamma R T}{\rho}\frac{\partial \rho}{\partial r}. \tag{4.9}$$

Inserting Equation (4.9) into Equation (4.8) and integrating gives the density profile for the tip vortex:

$$\rho = \frac{\rho_\infty \Gamma^2}{8\pi^2 a^2 r_c^2} f\left(\frac{r}{r_c}\right) + \rho_\infty, \tag{4.10}$$

where the function *f* is given by:

$$f\left(\frac{r}{r_c}\right) = \left[2\alpha Ei\left\{-\alpha\left(\frac{r}{r_c}\right)^2\right\} - 2\alpha Ei\left\{-2\alpha\left(\frac{r}{r_c}\right)^2\right\} - \frac{r_c^2 e^{-2\alpha\left(\frac{r}{r_c}\right)^2}\left(e^{\alpha\left(\frac{r}{r_c}\right)^2} - 1\right)^2}{r^2}\right]. \tag{4.11}$$

and Ei is the exponential integral in the form of the Cauchy principal value integral. An example of a density profile computed using Equation (4.10) is shown in Figure 4.21; the profile shows a lower density at the center of the vortex and, further from the core, the density returns to its freestream value.

The optical path difference for a beam of light passing through the density field shown in Equation (4.10) is computed using Equations (1.5) through (1.7):

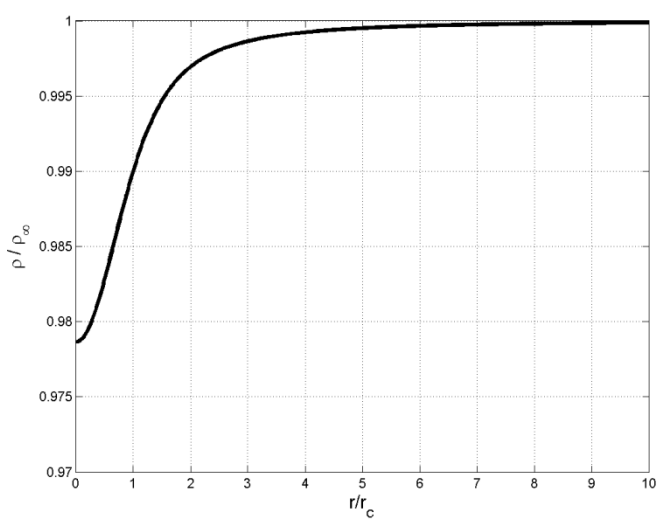

Figure 4.21. Density as a function of distance from the core center.

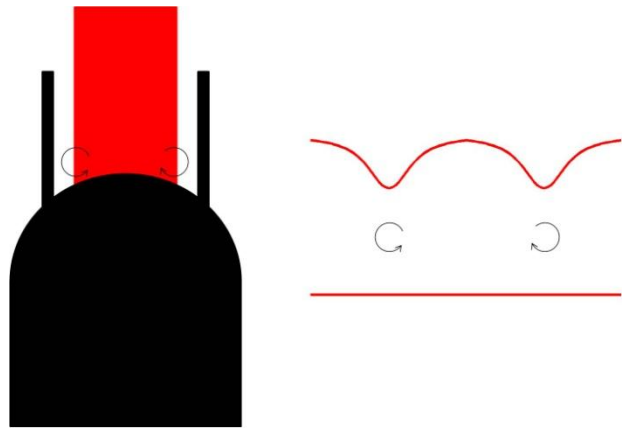

Figure 4.22. Schematic of beam passing between virtual duct fences. The 2 vortices are located at the corner between the hemisphereical turret and the virtual duct fences. (Right) An unaberrated outgoing beam (bottom) will have an aberrated wavefront (top) after encountering the vortices.

$$OPD(x) = \frac{\rho_\infty \Gamma^2}{\rho_{SL} a^2 r_c}\left[C(x) - \frac{1}{A_D}\int_{-A_D/2}^{A_D/2} C(x)dx\right] \tag{4.12}$$

where

$$C(x) = \frac{1}{r_c}\int_{-\infty}^{\infty} f\left(r/r_c\right)dy. \tag{4.13}$$

In the above equations, r is defined as the distance from the center of the vortex. As described in Chapter 1, once the *OPD(x)* distribution is known, the farfield effect of the vortex can be determined using the Fraunhofer approximation (Equation (1.2)), and a single-parameter representation of the effect of the vortex can be determined by computing the Strehl ratio, Equation (1.3).

Based on the above approach, a simple estimate for the optical effect of the corner vortices was generated as follows. First, the estimate was generated for the condition of a beam passing through the corner vortex perpendicularly to the axis of the

vortex; this geometrical definition was selected because it conforms to the assumptions of Equations (4.10) to (4.13) and because it gives a reasonable approximation for the general optical effect of the corner vortices. Furthermore, it was assumed that 2 vortices pass over the aperture (1 for each corner of the virtual duct), and the location of the corner vortices on the aperture was estimated from the DES simulations described in Section 4.5. Finally, it was assumed that the two corner vortices that lie on the aperture do not interact, such that the optical effect of the each vortex could be computed independently using Equations (4.10) to (4.13) and then added later. A schematic of the estimation approach is shown in Figure 4.22. Note that the location of the center of the vortex varies slightly depending on the curvature ratio, R/B, of the virtual-duct fence; however, a constant value was chosen of $x/A_D = 0.45$ that represents the middle of the range of values.

Figure 4.23 shows the OPD across half of the aperture for the case of a virtual duct with a curvature ratio of 1.88 at $M_\infty = 0.5$. The left part of the figure shows the vortex in 2-D space, where the surface of the turret is on the bottom and the virtual duct fence is on the right. The right part of the figure is the resulting aberration produced by the vortex. The locations of the two corner vortices can be seen by the decrease in OPD at $x/A_D = 0.45$. Figure 4.24 shows the farfield effect of the OPD distribution in Figure 4.23, computed using the Fraunhofer approximation (Equation (1.2)) and assuming an outgoing beam with a wavelength of 1 μm. The Strehl ratio for this case is 0.68.

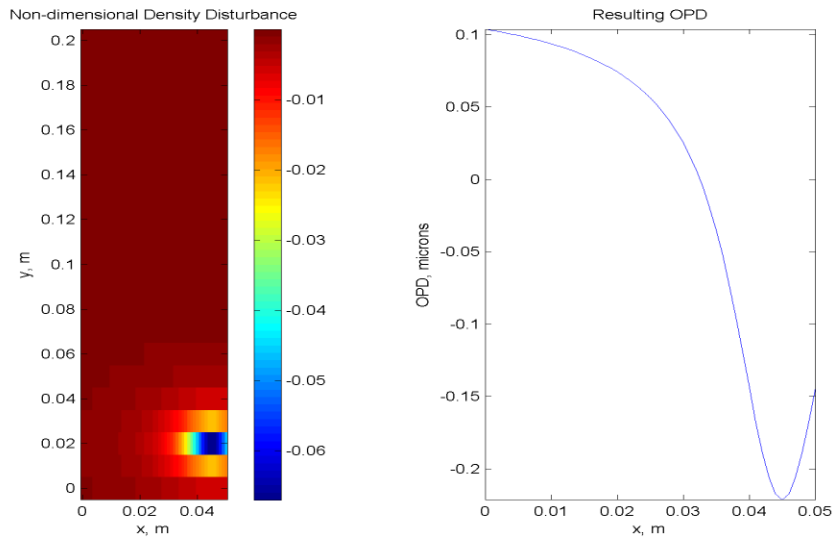

Figure 4.23. Non-dimensional density, left, and resulting OPD, right, inside half of the virtual duct, the other half is mirrored across the x = 0 axis. This case is for a curvature ratio, R/B, of 1.88 at M_∞ = 0.5.

Figure 4.25 shows the results of a parametric investigation of the effect of freestream Mach number and virtual-duct curvature ratio on the optical effect of the corner vortices. The figure shows that the Strehl ratio decreases substantially as the radius of curvature of the virtual-duct fences decreases and the circulation of the resulting corner vortices increase. The Strehl ratio also decreases as the freestream Mach number increases, which also increases the strength of the corner vortices.

One major feature of Figure 4.25 is the large variations in Strehl ratio as R/B becomes very small. These variations are caused primarily by the splitting of the beam on-target irradiance by the vortex aberrations (see Figure 4.26) and that, as the strength of the corner vortices increase, the outer and inner parts of the vortex aberration produces constructive and destructive interference. In particular, Figure 4.26 shows the

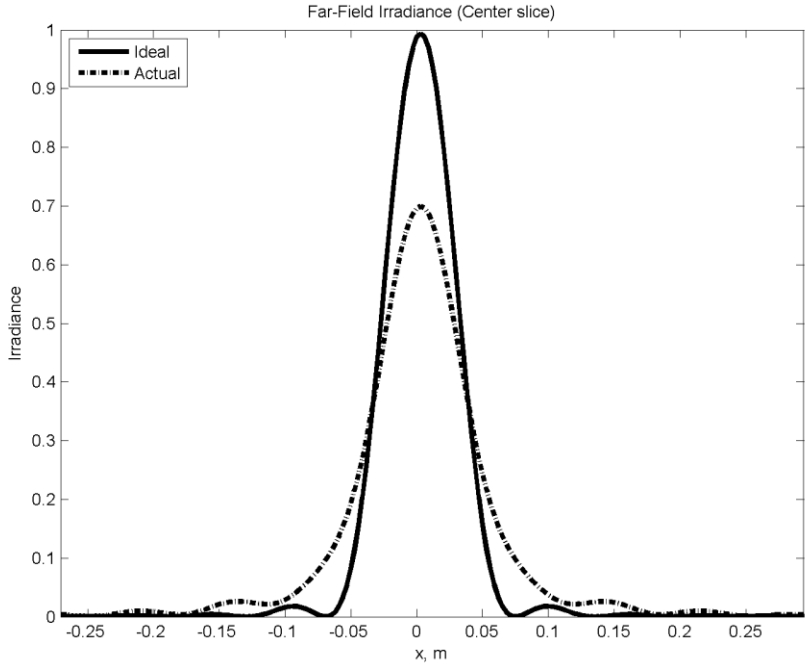

Figure 4.24. The farfield effect of the OPD distribution in Figure 4.23, computed using the Fraunhofer approximation, λ = 1 μm.

OPD and farfield irradiance patterns as the strength of the corner vortices increase, for M_∞ = 0.8. The figure shows that, as the strength of the vortex aberration increases, the aberration first produces a progressively split farfield pattern with multiple lobes that are displaced from the aim point; however, as the strength of the vortices increase still further, constructive interference between the inner and outer parts of the vortex aberration begins to produce a lobe back on the aim point.

Note that the farfield patterns in Figure 4.26 and the Strehl ratio values in Figure 4.25 were computed using the Fraunhofer approximation, Equation (1.2), and that the Strehl Ratio values would be significantly lower if the Large-Aperture Approximation (LAA), or Marachel Approximation, Equation (1.4), were used. This fact illustrates the

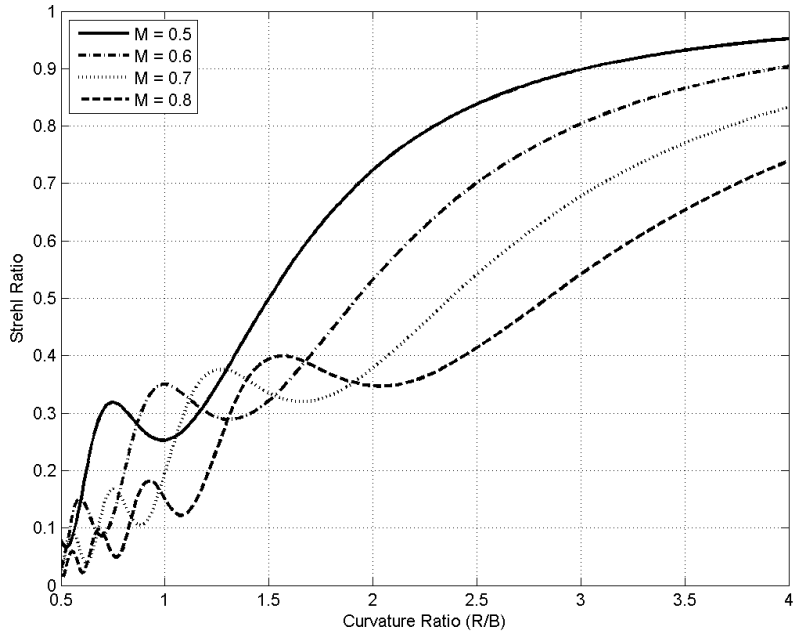

Figure 4.25. Strehl Ratio as a function of the curvature ratio and freestream Mach number.

limitation of the LAA, in which a normal distribution of the probability function of the wavefront is assumed. Figure 4.27 shows a similar result obtained by Gordeyev (2014) which compares the Strehl Ratio computed using the LAA as a function of the OPD_{rms} for aberrations with different probability distributions; the figure also shows that the Strehl Ratio can be significantly different from the LAA result depending on the nature of the optical aberration.

Figure 4.26. OPD, left, and farfield irradiance, right, for different curvature ratios at M_∞= 0.8. Look at Figure 4.25 showing the local minimum and maximum of SR plotted. Curvature ratios, R/B, are a) 2.1, b) 1.5, c) 1.04, d) 0.89, e) 0.74, f) 0.62, g) 0.58, and h) 0.53. Figure on pages 89-91.

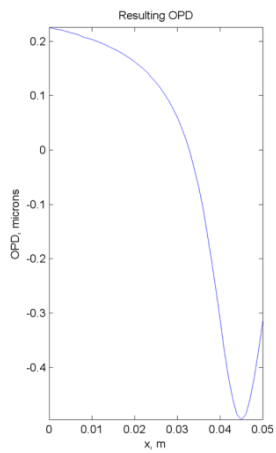
Resulting OPD
OPD, microns
x, m

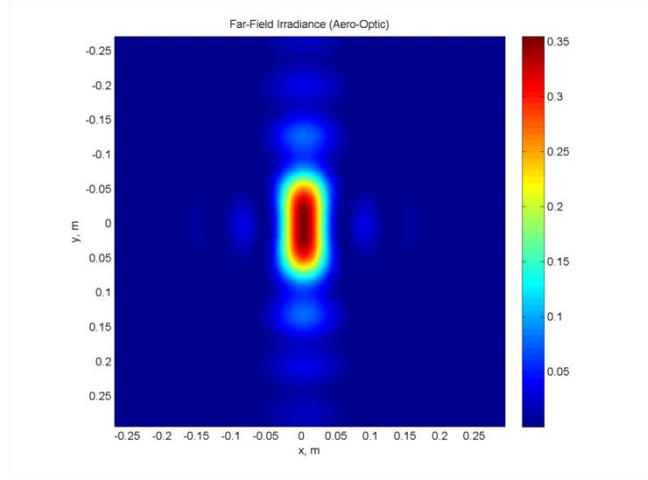
Far-Field Irradiance (Aero-Optic)
y, m
x, m

b)

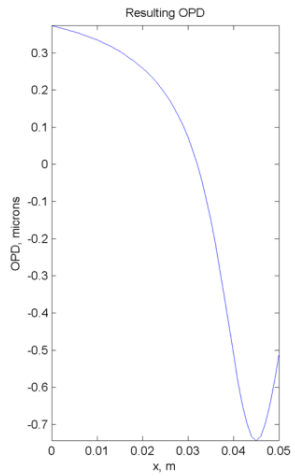
Resulting OPD
OPD, microns
x, m

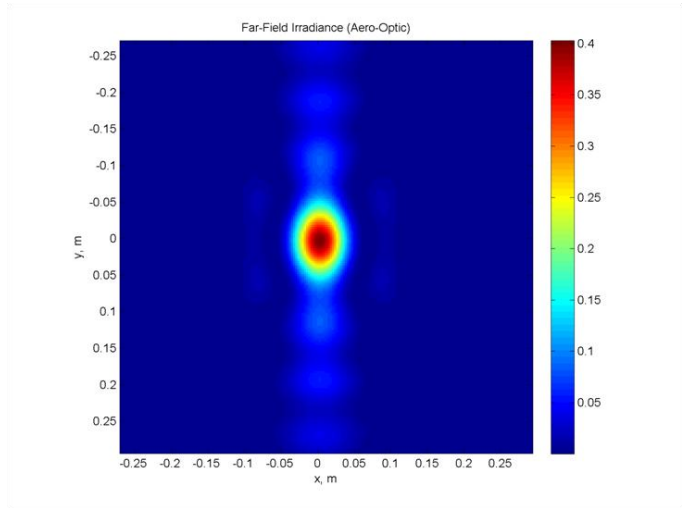
Far-Field Irradiance (Aero-Optic)
y, m
x, m

c)

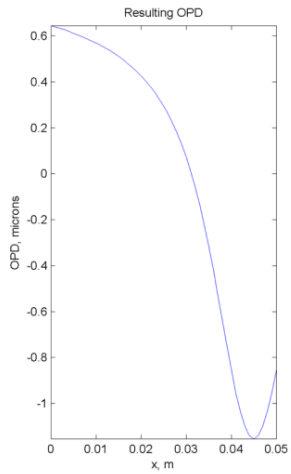
Resulting OPD
OPD, microns
x, m

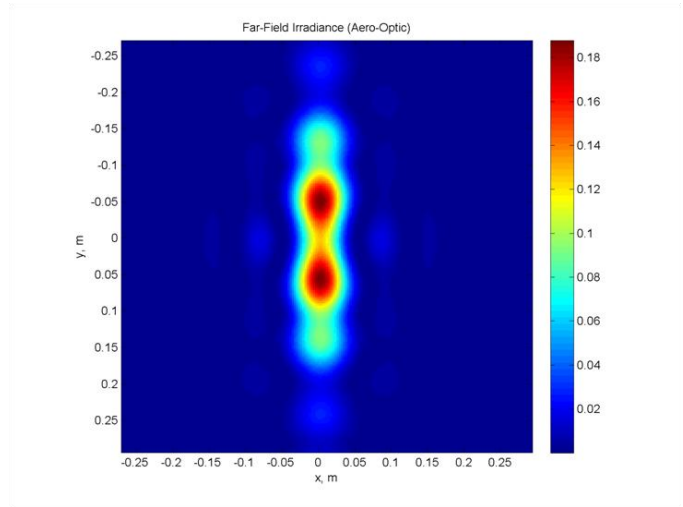
Far-Field Irradiance (Aero-Optic)
y, m
x, m

d)

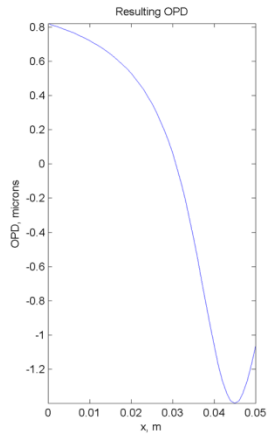
Resulting OPD
OPD, microns
x, m

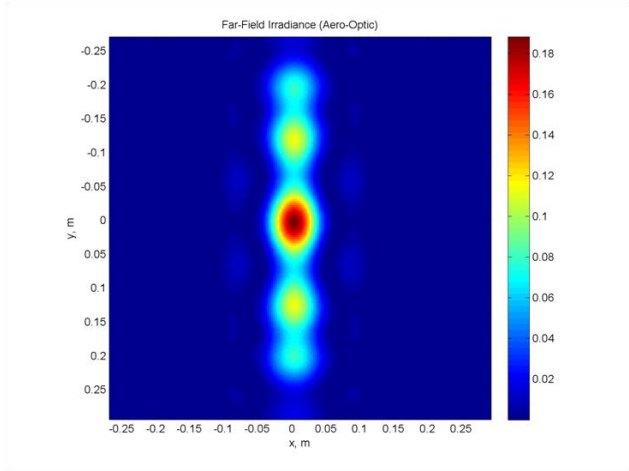
Far-Field Irradiance (Aero-Optic)
y, m
x, m

e)

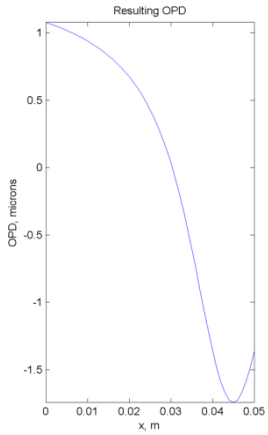
Resulting OPD
OPD, microns
x, m

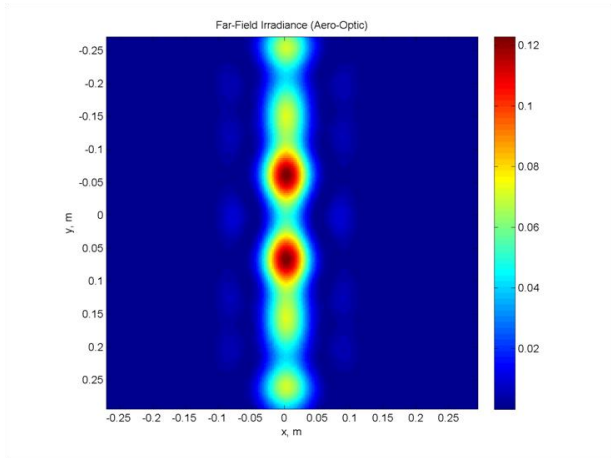
Far-Field Irradiance (Aero-Optic)
y, m
x, m

f)

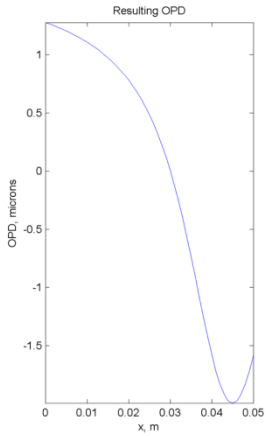
Resulting OPD
OPD, microns
x, m

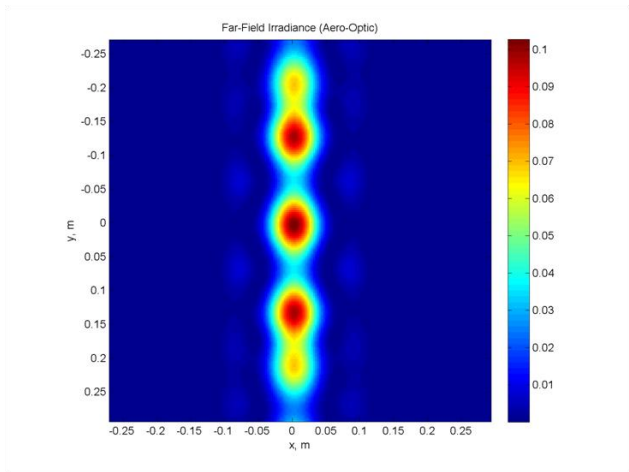
Far-Field Irradiance (Aero-Optic)
y, m
x, m

g)

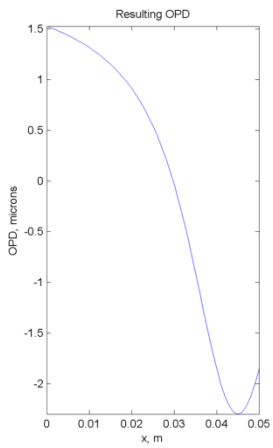
Resulting OPD
OPD, microns
x, m

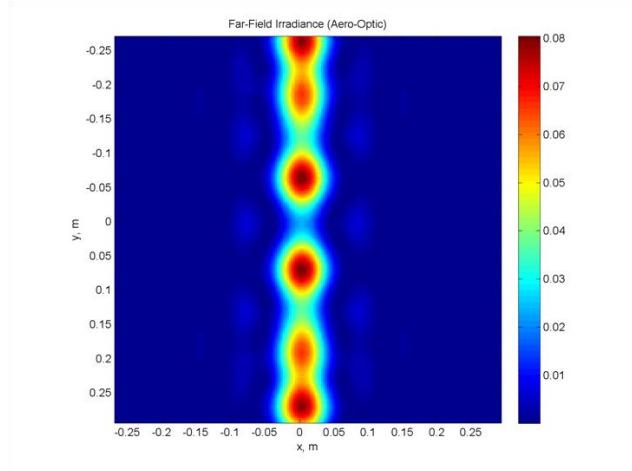
Far-Field Irradiance (Aero-Optic)
y, m
x, m

h)

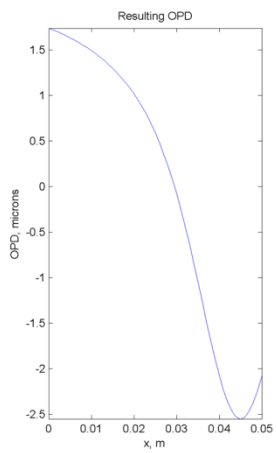
Resulting OPD
OPD, microns
x, m

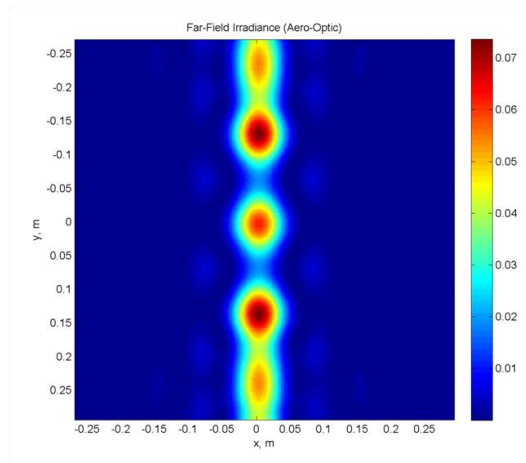
Far-Field Irradiance (Aero-Optic)
y, m
x, m

It should be noted that the estimates provided in this section only show the approximate magnitude of the optical aberration caused by the corner vortices. Specifically, the calculations do not account for temporal variation of the aberrations or turbulence in the vortex core; this temporal variation and turbulence could change the farfield irradiance patterns and Strehl Ratios from that shown in Figure 4.25; however, Figure 4.25 still provides a reasonably accurate first approximation of the effect of the corner vortices.

In general, Figure 4.25 shows that if no AO compensation is used, a Strehl Ratio of roughly 0.55 or higher can be achieved for Mach numbers of 0.8 or lower if the

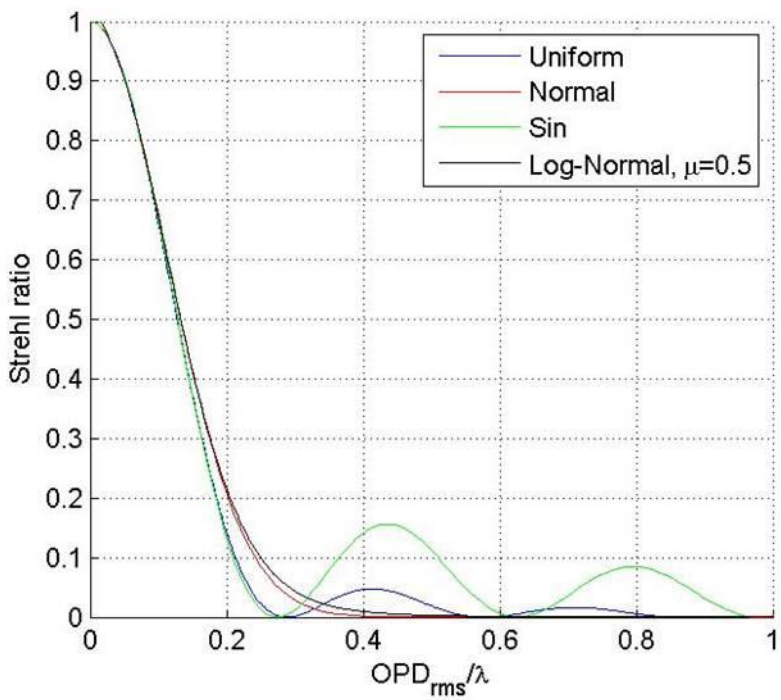

Figure 4.27 Strehl Ratio vs OPD_{rms} showing the instability in using the Large Aperture Approximation at larger OPD_{rms} values (Gordeyev 2014).

virtual-duct curvature ratio is only 3. On the other hand, if the curvature ratio is 1 then the Strehl Ratio falls below roughly 0.3 for all Mach numbers above 0.5. In the following section, an idea of the kind of curvature ratio that would be necessary in practice is examined in more detail.

4.8 Conclusions

The secondary vortices that form in the corners between the virtual-duct wall and the sphere were investigated using a combination of experiments and CFD to understand the effects on an outgoing beam. The investigation showed that as the curvature of the virtual-duct fences decreases, the circulation of the corner vortices decreases and the core radius decreases; both of these effects mean that the corner vortices have a stronger optical effect on an outgoing beam as the virtual-duct curvature increases. As such, it is desirable to use a virtual duct with the minimum curvature necessary to achieve the design objectives of an optical system. The next section presents a method of determining the optimum virtual-duct shape to achieve given design objectives.

CHAPTER 5:

GEOMETRY OPTIMIZATION

The results of Chapters 2 and 3 showed how a virtual-duct design developed in a trial-and-error fashion can improve the critical Mach number and/or boundary-layer separation performance of a pod or canonical spherical turret. There is, however, no guarantee that the designs that produced the improved results shown in Chapters 2 and 3 were optimum, or even nearly-optimum designs, and that even better performance cannot be achieved with a better design. Considering the basic virtual-duct concept shown in Figure 3.1, it is clear that there are a multitude of possible fence designs that would result in an improvement over the unmodified hemispherical turret configuration.

One method of moving towards the optimum virtual-duct design is to use design-optimization techniques. Furthermore, even before the optimization routine is run, Design of Experiments (DoE) screening methods can be employed to find the most-important design variables to use in the design-optimization approach. Once the important design variables are found, the details of a design are improved in an iterative fashion, where each iteration moves the design closer to a user-defined goal defined by an “objective function.” This chapter summarizes an investigation into the optimum

virtual-duct configuration using Design of Experiments screening techniques and design-optimization techniques, and summarizes the results obtained.

5.1 Design of Experiments

In Chapter 3, a process of using a guess and check method is outlined, showing that minor changes to the fence shape can have different effects on the surface pressure measurements. This “best-guess approach” is frequently used in practice by engineers and scientists, and usually works reasonably well, but it has two main disadvantages. First, if the initial best guess does not produce the correct result, the designer must take another guess at the design configuration. The second problem is that if the initial guess produces an acceptable result, the designer is tempted to stop testing without a guarantee that the best solution is found (Montgomery 2009). This problem seemed to happen with the underwing pod wind tunnel experiment; except that the next guess could not be completed since the model was made for only 1 virtual-duct fence shape.

The next step would be to move on to a “one-factor-at-a-time” approach where a baseline set of design parameters are identified, and then each one is perturbed one at a time to see the effect. This once again is an effective strategy, but still does not guarantee success, since it does not account for the interaction of any variables. Considering the virtual duct described in Chapter 3, if the maximum diffusion point is moved out, the diffusion and contraction of the virtual duct will both be increased; however, if it is only desired to have a strong contraction of the flow, then this first-

order study would not find it. Therefore the correct approach to dealing with several factors is to conduct a Design of Experiments (DoE) screening study to look at possible interactions between variables.

A common DoE study is known as a “factorial experiment” (Montgomery 2009) where the effect of design variables is examined together, instead of one at a time. The method used in this investigation is the 2^k method, discussed in detail in Chapter 6 of Montgomery (2009) and also by Lundstedt (1998). The k represents the number of design variables to vary. A baseline value is selected for each variable and then the variable is perturbed slightly. By changing each variable systematically, the effect of each variable and its interactions with other variables can be found. If 2^k function calls are too many, a method to decrease the function calls is known as the 2^{k-2} method. This method decreases the number of function calls needed, but also decreases the accuracy of the DoE.

In the following sections, DoE methodology is applied to two design problems related to the virtual-duct concept. First, the DoE approach is applied to the design of a simple fairing for a hemispherical turret, such as might be used to improve the critical Mach number for the turret. Following this, the DoE approach is also applied to the design of the virtual duct for a hemispherical turret. For the optimization of a fairing, the 2^k method is used since there are fewer variables, but for a turret on a virtual duct, the 2^{k-2} method is used to minimize the function calls. The beginning of the next 2 sections gives an overview of each study.

5.1.1 DoE Analysis of Fairing

In this section, the Design of Experiments (DoE) approach is first applied to the design of a downstream fairing for a spherical turret. As discussed in Chapter 2, the purpose of the fairing is to reduce the local curvature of the overall shape, thereby reducing the flow acceleration around the turret and hence increasing the critical Mach number. Note that for this study, it was assumed that the fairing would be sufficient to eliminate flow separations in the vicinity of the optical aperture regardless of the fairing shape, so the DoE focused on the effect on critical Mach number only.

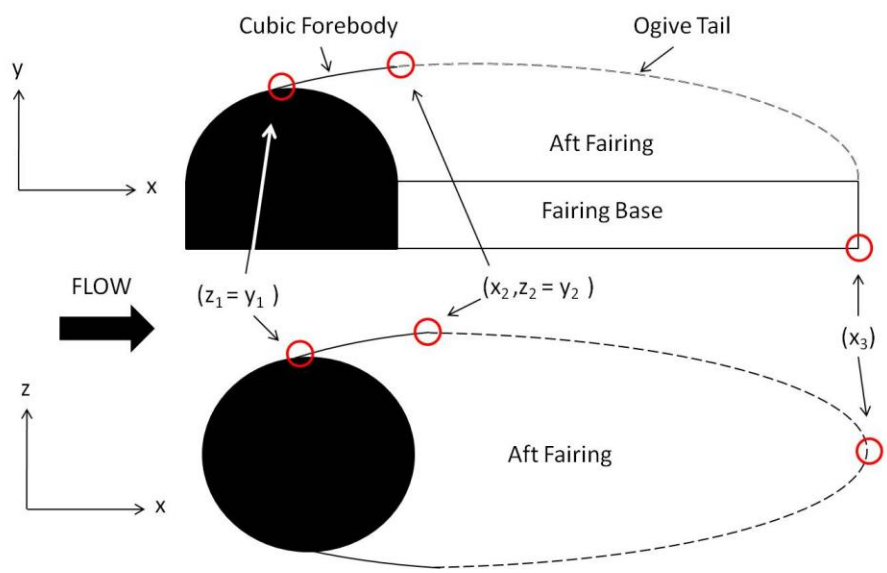

Figure 5.1. Aft fairing defined by 4 points to be studied.

The basic turret configuration used in this section is a canonical hemisphere-on-cylindrical-base turret, similar to the one shown in Figure 1.3; however, the results obtained are also generally applicable to the aircraft-mounted pod configuration examined in Chapter 2. The height for the cylindrical base of the turret was fixed at *D*/3

(where *D* is the turret diameter); this base height is commonly used for hemispherical turret configurations and has been shown to be sufficiently high that the hemispherical turret is not influenced by the incoming boundary layer on the surface, or the resulting necklace vortex as shown in Figure 1.9 (Gordeyev 2010).

Other assumed design features for the fairing were that the fairing would be rotationally symmetric with an ogive-shaped tail (dotted line in Figure 5.1), and that a cubic-shaped forebody (Equation (2.2)) would be used to blend the fairing into the hemispherical turret (solid line in Figure 5.1). With these assumed design features, the shape of the ogive tail is fully defined by the position of the trailing edge (x_3) and the maximum width of the fairing (x_2 and y_2 (or z_2)). The cubic forebody is also fully defined by the boundary conditions consisting of the point of contact with the turret ball (point 1 in Figure 5.1), the condition of zero slope at the point that the cubic forebody blends into the ogive tail, and the condition of matching the slope of the cubic forebody with the slope of the turret ball at the point of contact with the turret ball. As such, with the given design assumptions, a unique fairing shape is defined by the selection of the points 1 to 3 shown in Figure 5.1; more specifically, a unique design is specified by the selection of the 4 values x_1, x_2, y_2, and x_3.

Since the fairing shape can be defined by 4 parameters, a 2^k factorial DoE approach was implemented with k = 4 to determine the most important parameters and combinations of parameters. In the 2^k design approach, 2^k combinations of the important design parameters are created and the resulting design configurations are analyzed to determine their effect on the performance parameter of interest (i.e. critical

Mach number for this case). Once the design configurations are analyzed, a numerical value, β, is found that represents how much each parameter, and combination of parameters, affects the critical Mach number. Once the total effect for each parameter, and combination of parameters, is found, a percentage is computed to show how much it affects the critical Mach number. This percentage is used to determine which variables have the strongest effect on the solution and need to be included in the optimization.

TABLE 3

VALUES FOR EACH VARIABLE USED IN THE DOE SCREENING STUDY FOR THE FAIRING, D REPRESENTS THE DIAMETER OF THE TURRET.

CFD Run	x1	x2	y2	x3	M_{CRIT}
1	0.1D	1.8D	1.1D	4.5D	0.608
2	0.3D	1.8D	1.1D	4.5D	0.704
3	0.1D	2.2D	1.1D	4.5D	0.595
4	0.3D	2.2D	1.1D	4.5D	0.746
5	0.1D	1.8D	1.3D	4.5D	0.626
6	0.3D	1.8D	1.3D	4.5D	0.444
7	0.1D	2.2D	1.3D	4.5D	0.622
8	0.3D	2.2D	1.3D	4.5D	0.718
9	0.1D	1.8D	1.1D	6.5D	0.615
10	0.3D	1.8D	1.1D	6.5D	0.725
11	0.1D	2.2D	1.1D	6.5D	0.603
12	0.3D	2.2D	1.1D	6.5D	0.756
13	0.1D	1.8D	1.3D	6.5D	0.642
14	0.3D	1.8D	1.3D	6.5D	0.649
15	0.1D	2.2D	1.3D	6.5D	0.632
16	0.3D	2.2D	1.3D	6.5D	0.734

TABLE 3 shows the values of the parameters x_1, x_2, y_2, x_3 generated by the 2^k method. As discussed above, each combination of parameters produced a unique fairing shape, which was analyzed using the Euler routines in the CFD program, AVUS. In this case, Euler routines were used since it was expected that the fairing would ensure attached flow so that the flow on the turret and fairing would be well represented by the Euler solutions. The grid was generated using Gambit and consisted of about 1 million unstructured grid points depending on the exact geometry of the fairing. Furthermore, the CFD solutions were computed at M_∞= 0.1, since the critical Mach number could be computed from the resulting pressure distribution and Equation (1.8).

The most important output of the DoE analysis are the influence parameters, β, which show the magnitude of the effect that a particular design parameter or combination of parameters has on the design objective (i.e. M_{crit} in this case). An illustration of how the DoE influence parameters, β, are computed can be obtained by examining the parameter x_1 in TABLE 3. It has a high value of 0.3D (highlighted in gray) and a low value of 0.1D (not highlighted) where the front of the turret is at 0.0D. By taking the average of the critical Mach number for all the CFD runs with a high x_1 value of 0.3D and the average for all the CFD runs with a low x_1 value of 0.1D, the difference, β, shows how much this parameter affects the critical Mach number:

$$\beta = abs(\overline{M_{Crit_{(x_1=High)}}} - \overline{M_{Crit_{(x_1=Low)}}}). \tag{5.1}$$

The absolute value of β is computed since only the magnitude of the effect on critical Mach number is important.

Once a β is found for each variable, and combination of variables, all the values are added up to produce a total change of the critical Mach number:

$$Total\ Change = \sum \beta. \tag{5.2}$$

Finally, by normalizing by the total change, the relative effect of each parameter or combination of parameters on the critical Mach number is obtained as a percentage. TABLE 4 shows the percent contribution of each influence parameter.

TABLE 4 shows that the x_1 variable contributes the most toward the total change

TABLE 4

RELATIVE EFFECT OF EACH PARAMETER OR COMBINATION OF PARAMETERS ON MCRIT, COMPUTED USING DESIGN OF EXPERIMENTS APPROACH.

Influence parameter	Total Change	Percent Contribution
β_{x_1}	**0.089**	**35.00%**
β_{x_2}	**0.026**	**10.33%**
β_{y_2}	**0.013**	**5.04%**
β_{x_3}	**0.014**	**5.43%**
$\beta_{x_1x_2}$	**0.036**	**14.15%**
$\beta_{x_1y_2}$	**0.038**	**14.93%**
$\beta_{x_1x_3}$	**0.004**	**1.42%**
$\beta_{x_2y_2}$	**0.014**	**5.63%**
$\beta_{x_2x_3}$	**0.003**	**1.13%**
$\beta_{y_2x_3}$	**0.002**	**0.93%**
$\beta_{x_1x_2y_2}$	**0.012**	**4.55%**
$\beta_{x_1x_2x_3}$	**0.002**	**0.64%**
$\beta_{x_1y_2x_3}$	**0.000**	**0.15%**
$\beta_{x_2y_2x_3}$	**0.000**	**0.15%**
$\beta_{x_1x_2y_2x_3}$	**0.001**	**0.54%**

at a percent contribution of 35%. This is obvious since this influence parameter defines the location of the front of the fairing, and hence would be expected to affect the flow in the region of the turret the most. Y_2 and x_2 also have strong effects on the solution when combined with x_1. This is due to the fact that the combination of these variables helps control the slope of the fairing near the turret. If x_2 (or y_2) is too close to the turret, the fairing angle will be too steep and will produce local high-speed flow. The location of the back of the fairing has little effect on the solution according to this study, but it should be noted that the DoE study placed the last point 4.5-6.5 ball diameters downstream of the turret. If the back of the fairing is moved much closer to the turret, it will have a stronger effect on the solution since the overall shape will begin to perform much like a turret without a fairing. As such the back of the fairing was held constant for the optimization study to be discussed later in this Chapter.

As shown in TABLE 3, the critical Mach number values produced by the DoE study varied from .595 to .756; however, as discussed in Chapter 2, it would be preferable if the fairing produced critical Mach numbers of 0.8 or higher, which is closer to the cruise speeds of jet transports or fighters. It should be noted, however, that DoE screening methods do not produce an optimized design; rather, DoE screening methods merely identify the most important design parameters, and optimization routines are necessary to converge to a design with a critical Mach number closer to 0.8. Based on the percent contributions shown in TABLE 4, it is apparent that x_1, x_2, and y_2 are the most important parameters needed in any optimization routine. As such, x_3 will be left out of the optimization for the faring. This is advantageous as it will decrease the 4-

variable optimization routine into a 3-variable optimization routine producing fewer function calls and ultimately a shorter time to converge to a solution. This optimization study will be discussed in more detail later in the chapter.

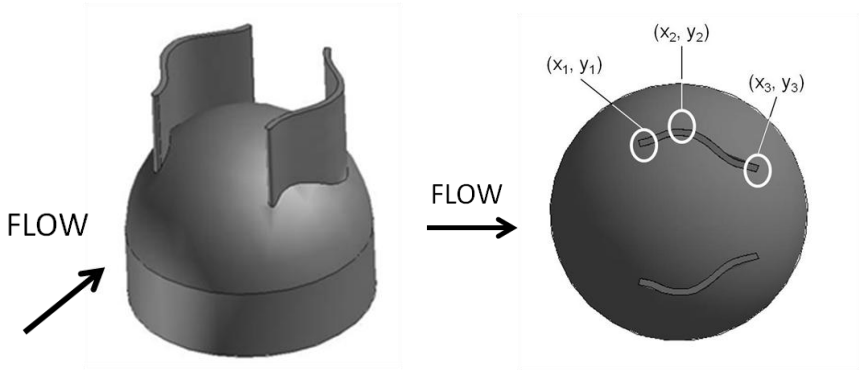

Figure 5.2. Isometric (left) and plan (right) view of turret with flow in positive x-direction. The fence is defined by 3 points that are adjusted to find the optimum shape to minimize the objective function.

5.2 Development of Fast Solution Methodology for Virtual Duct

In the DoE analysis of the fairing shown in the preceding section, an Euler routine was used to compute solutions for the different fairing geometries that came out of the DoE analysis; the use of an Euler routine in this case was possible due to the highly-streamlined fairing shapes that were examined such that boundary-layer separation could be assumed to be minimal or nonexistant. On the other hand, the virtual-duct-on-spherical-turret geometries are not streamlined, such that the analysis routine must be capable of predicting boundary-layer separation with reasonable precision. Furthermore, as discussed in Chapter 4, CFD computations of the virtual duct should

ideally be computed using a DES scheme in order to accurately capture the corner vortices that form in the virtual duct.

Use of DES computations in the DoE analysis represents a large computational expense, however. Furthermore, as will be discussed below, in addition to the more-accurate DES simulation of the virtual duct, it is also advantageous to have available a faster, less-accurate analysis technique as part of the optimization process that can produce results rapidly with only a small reduction in accuracy. As such, a computational approach was developed for the virtual-duct configurations in which an Euler code is used in combination with a separate routine to predict boundary-layer separation. Specifically, the location of boundary-layer separation was predicted from the Euler data using a pressure-based prediction algorithm called the Stratford criterion; this methodology is described in further detail below. The critical Mach number for the

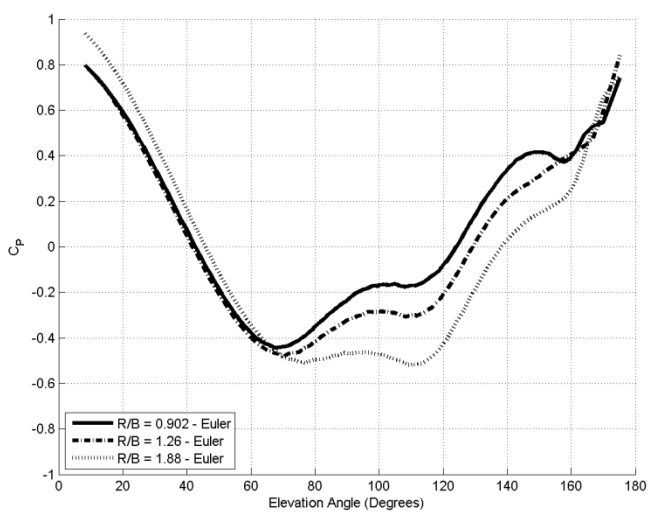

Figure 5.3. Pressure distributions of the Euler solution for flow through the virtual ducts shown in Figure 5.4.

virtual-duct design configurations was also computed from the Euler solutions from the minimum predicted, C_P, as described in Chapter 2.

An illustration of the ability of the Euler CFD to generate useful information regarding the virtual-duct performance is shown in Figure 5.3. The figure shows pressure distributions along the centerline of the turret (between the virtual-duct fences) computed using the Euler routine in FLUENT with a fully structured mesh for 3 different virtual ducts with different curvatures; diagrams of the 3 virtual-duct shapes are shown in Figure 5.4. These shapes are the same fence shapes as those used in the DES CFD study shown in Chapter 4 (but are different from the virtual-duct shapes tested experimentally in Chapter 3). Referring to Figure 5.3 and Figure 5.4, it is possible to discern a clear relationship between the virtual-duct geometry and the Euler-computed pressure distributions along the centerline of the turret. Specifically, all three virtual-duct geometries have the same inlet width and starting location, and also have very similar pressures at the inlet location of around an elevation angle of 60° in Figure 5.3. Downstream of the inlet, however, it is possible to see a clear relationship between the C_P on the turret surface and the shape of the virtual duct for each case, with the more highly-curved virtual ducts (i.e. smaller curvature ratio) producing lower flow speeds on the turret as expected. As such, it is clear that the Euler results are useful for making at least preliminary selections between different design configurations for the virtual duct.

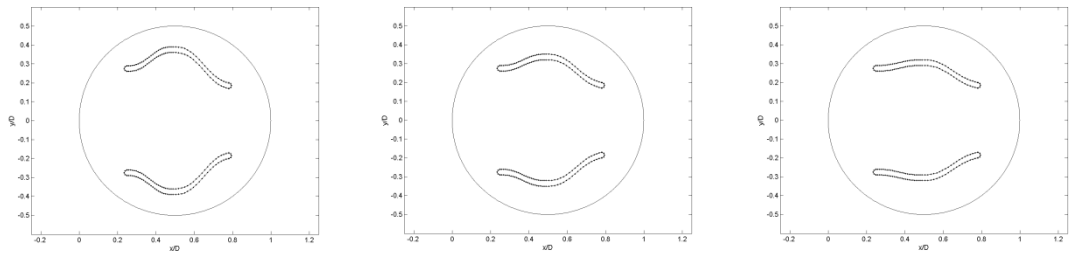

Figure 5.4. Virtual duct wall shapes computed in Figure 5.3. The curvature ratios are, from left to right, 0.902, 1.26, and 1.88.

5.2.1 Stratford Criterion for Prediction of Boundary-Layer Separation

A method that has been developed to predict separation of turbulent boundary layers based on pressure distributions is known as Stratford's criterion (Stratford 1959). This method was developed to predict boundary-layer separation for flow on a flat plate or airfoil. In the Stratford approach, a solution for the "inner" part of the boundary layer is found and compared to the "outer" part of the boundary layer to form the following condition for flow separation:

$$C_p' \sqrt{x \frac{dC_p'}{dx}} = 0.39 (\frac{Re_x}{10^6})^{0.1}, \tag{5.3}$$

which can be rearranged as:

$$\frac{C_p' \sqrt{x \frac{dC_p'}{dx}}}{0.39 (\frac{Re}{10^6})^{0.1}} = 1, \tag{5.4}$$

where *Re* represents the local Reynolds number based on the length of the surface and the canonical pressure coefficient C_p' is defined as

$$C_p' = \frac{C_p - C_{p_{min}}}{1 - C_{p_{min}}}. \tag{5.5}$$

As such, boundary-layer separation is predicted using the Stratford criterion when the term on the left-hand side of Equation (5.4) is greater than or equal to 1.

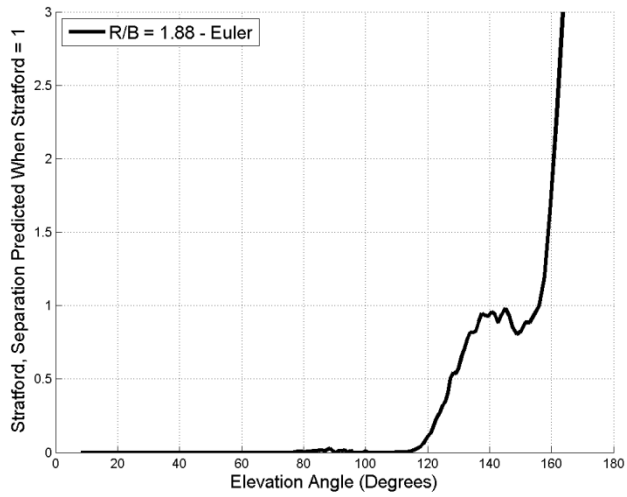

Figure 5.5. Stratford's criterion applied to the lowest-curvature, R/B = 1.88, pressure distributions shown in Figure 5.3.

5.2.2 Example of Stratford Criterion Applied to Virtual Duct

Prior to showing an example of the Stratford criterion applied to an Euler solution for the virtual duct, it should be reiterated that the Euler CFD cannot model the corner vortices that form in the corners of the virtual duct and that were investigated in Chapter 4. However, as shown in Figures 3.5, 3.7 and 3.8, the corner vortices only become important as the curvature of the virtual duct increases. As such, as the virtual-duct becomes more highly-curved, the Euler/Stratford approach described here becomes less accurate, so that the Euler/Stratford approach can only be used with

confidence for the modeling of virtual ducts with relatively-low curvature (or high curvature ratio R/B). Note that this limitation is not particularly severe since, as shown in Chapter 4, the corner vortices produced by higher-curvature virtual ducts also produce in and of themselves optical aberrations on the outgoing beam, so that an objective of any optimization of the virtual duct should also be to use a virtual-duct shape with the minimum curvature possible. In summary, it must be remembered that for the Euler/Stratford approach described here, and the optimization process in which it is used (shown below), it is assumed that the virtual-duct curvature is relatively low.

As an example of the ability of the Euler/Stratford approach to predict boundary-layer separation in a low-curvature virtual duct, Figure 5.5 shows the Stratford criterion (i.e. the term on the left side of Equation (5.4)) computed for the pressure distribution of the low-curvature, R/B = 1.88, virtual duct shown in Figure 5.3. The figure shows that the Stratford method predicts boundary-layer separation at approximately 155° for this case. Although the virtual-duct shape for the result shown in Figure 5.5 is slightly different than the shapes tested experimentally in Chapter 3, the predicted separation location in Figure 5.5 is still very close to the location that was measured for the low-curvature duct investigated in Chapter 3 (see Figure 3.5). This close comparison demonstrates the ability to predict boundary-layer separation with reasonable accuracy using the Euler/Stratford approach.

In summary, using an Euler routine and the critical-Mach-number and Stratford approach, it is possible to obtain fast and relatively-accurate estimates of the susceptibility of a virtual-duct design to shock formation and boundary-layer separation.

This development of a fast analysis approach provides a substantial advantage for the DoE analyses and, as will be shown below, the design-optimization computations. As discussed above, the Euler/Stratford approach developed here will become less accurate as the curvature of the virtual duct increases and the importance of the corner vortices increases. However, the Euler solutions should still give reasonable results for low- to medium-curvature virtual-duct configurations and, as shown in Chapter 4, it is desirable in any case to use the lowest-curvature virtual duct possible in order to reduce the optical effect of the corner vortices.

5.3 DoE Analysis of Virtual Duct

For the virtual-duct geometry, the objective of the DoE analysis was to identify the important design parameters and their relative effect on the design objectives of minimizing the critical Mach number and delaying flow separation. As discussed in Section 4.5, a unique virtual-duct geometry can be defined by the location of 3 points, each having an x and y component for a total of 6 variables. In order to simplify the analysis, the height of the virtual-duct fence was not included as a design parameter; rather, the fence height was held constant for all cases at 0.9 times the turret diameter. Therefore, in order to use the 2^k method with 6 variables, an analysis of 64 different combinations of the design variables would need to be completed. However, to reduce the number of required analyses, a fractional factorial design can be used. Fractional factorial designs assume that high-order interactions have a negligible effect on the performance of the design, and only use information on the low-order interactions by

completing only a fraction of the complete 2^k parameter combinations (Montgomery 2009). For the virtual-duct study, a 2^{k-2} method was used that allowed the DoE study to be completed with only 16 CFD runs.

For the virtual-duct DoE study, the objective function was set as the location of separation. As such, the output of the DoE study (i.e. TABLE 5) shows the effect that each design parameter or combination of parameters has on the location of separation. Note that this emphasis on the location of separation appears to ignore the second objective of the virtual duct, which is to increase the critical Mach number on the turret.

TABLE 5

VARIABLES CHOSEN FOR EACH DOE RUN ALONG WITH THE CURVATURE RATIO, R/B. THE HIGHER VALUE FOR THE VARIABLE IS HIGHLIGHTED GREY.

Run	x_1	y_1	x_2	y_2	x_3	y_3	R/B	M_{crit}	Separation Location
1	0.25D	0.23D	0.47D	0.254D	0.765D	0.17D	2.71	0.679	134.7
2	0.265D	0.23D	0.47D	0.254D	0.78D	0.17D	2.74	0.693	142.4
3	0.25D	0.245D	0.47D	0.254D	0.78D	0.185D	4.09	0.755	151.6
4	0.265D	0.245D	0.47D	0.254D	0.765D	0.185D	3.67	0.749	150.9
5	0.25D	0.23D	0.485D	0.254D	0.78D	0.185D	3.22	0.704	158.8
6	0.265D	0.23D	0.485D	0.254D	0.765D	0.185D	2.88	0.686	146.2
7	0.25D	0.245D	0.485D	0.254D	0.765D	0.17D	3.16	0.750	159.2
8	0.265D	0.245D	0.485D	0.254D	0.78D	0.17D	3.27	0.745	160.4
9	0.25D	0.23D	0.47D	0.269D	0.765D	0.185D	2.20	0.688	142.8
10	0.265D	0.23D	0.47D	0.269D	0.78D	0.185D	2.20	0.674	141.3
11	0.25D	0.245D	0.47D	0.269D	0.78D	0.17D	2.45	0.735	146.9
12	0.265D	0.245D	0.47D	0.269D	0.765D	0.17D	2.20	0.734	146.2
13	0.25D	0.23D	0.485D	0.269D	0.78D	0.17D	2.11	0.688	142.6
14	0.265D	0.23D	0.485D	0.269D	0.765D	0.17D	1.90	0.678	142.4
15	0.25D	0.245D	0.485D	0.269D	0.765D	0.185D	2.52	0.732	147.8
16	0.265D	0.245D	0.485D	0.269D	0.78D	0.185D	2.56	0.730	146.2

However, it should be noted that for the virtual-duct optimization, the critical Mach-number requirement was incorporated into the optimization as a design constraint, in the sense that potential virtual-duct shapes were given a poor evaluation if they did not produce a critical Mach number greater than a defined minimum value. As such, the approach of the virtual-duct DoE and optimization was to maximize the separation location under the condition that the critical Mach number was also greater than a minimum cutoff value.

TABLE 5 shows the fence points for each DoE run for the virtual-duct configurations, along with the curvature ratio. Each of these fence shapes were analyzed using Euler CFD to find the pressure distribution. The CFD calculations for this study were performed using the Euler routine in the CFD code AVUS, and using a fully unstructured mesh. From the Euler data, the boundary-layer separation location was estimated using the Stratford criterion and is shown in TABLE 5, the critical Mach Number is also included as a reference although it had no affect on the DoE. The influence parameters and subsequent percent contributions of each design parameter or combination of parameters to the separation location were then computed using the same methods presented in Section 5.1.

TABLE 6 shows the percent contribution of each influence parameter to the separation location. The percent contributions show three strong 1st-order interactions and one strong 2nd-order interaction. As shown in the table, the strong 1st-order interactions involve only the parameters y_1, x_2, and y_2. At first glance, the fact that x_3 and y_3 do not produce strong 1st-order interactions appears to indicate that the location of

the virtual-duct outlet has little effect on how the virtual duct delays separation. This presumption is, however, incorrect, because the y_3 parameter appears in the 2nd-order interaction $y_1y_3 + x_2y_2$ which produces a strong 15.76% contribution to the separation location. This 2nd-order interaction, $y_1y_3 + x_2y_2$, is a combination of the inlet and outlet widths, y_1y_3, with the location of the virtual-duct center point, x_2y_2, and effectively reflects that the way in which the widths of the virtual-duct inlet and outlet (y_1 and y_3) affect the separation location also depends on the location of the virtual-duct center point. Specifically, the large $\beta_{y1y3} + \beta_{x2y2}$ term shows that the center of the virtual duct must be well matched to the inlet and outlet widths of the virtual duct in order to produce a low pressure gradient and delayed boundary-layer separation. In this regard, referring to Figure 5.3, the R/B = 1.88 case had an effective location of the center point in the sense that it held the pressure inside the virtual duct fairly constant given the inlet and outlet width of the virtual duct. TABLE 6 also shows that the parameters x_1 and x_3 make individual contributions to the separation location that are well below 10%, and that any influence parameters that include these variables are also below 10%. As such, in order to increase the speed of the optimization, it is advantageous to leave out x_1 and x_3 thereby reducing the 6-variable optimization to a 4-variable optimization. Therefore, only parameters y_1, x_2, y_2, and y_3 are used in the optimization to be discussed below.

In summary, the DoE analysis for the virtual duct shows that an optimization routine that attempts to delay as far as possible the location of separation while maintaining a minimum critical Mach Number of 0.7 should be a 4-variable optimization problem involving the parameters y_1, x_2, y_2, and y_3. Appendix C shows an initial

evaluation of the virtual-duct design space, while Section 5.6 show a complete optimization study looking at maximizing the location of separation.

5.4 Optimization Methods

Design optimization is the process of finding the optimum solution to a given design problem. The method consists of defining a function that quantifies the success of a design and then attempting to find an optimum design that minimizes that function while applying any known constraints to the design (Tovar 2010). Several optimization

TABLE 6

DESIGN OF EXPERIMENTS FOR FAIRING, COMPARING THE DIFFERENCE BETWEEN THE HIGH AND LOW VALUES OF EACH PARAMETER BASED ON THE SEPARATION LOCATION.

Influence Parameters	Percent Contribution
β_{x_1}	**0.58%**
β_{y_1}	**28.36%**
β_{x_2}	**18.49%**
β_{y_2}	**19.36%**
β_{x_3}	**3.43%**
β_{y_3}	**0.98%**
$\beta_{x_1y_1} + \beta_{x_2x_3}$	**0.18%**
$\beta_{x_1x_2} + \beta_{y_1x_3}$	**2.74%**
$\beta_{x_1y_2} + \beta_{x_3y_3}$	**0.00%**
$\beta_{x_1x_3} + \beta_{y_1x_2} + \beta_{y_2y_3}$	**0.98%**
$\beta_{x_1y_3} + \beta_{y_2x_3}$	**5.06%**
$\beta_{y_1y_2} + \beta_{x_2y_3}$	**4.07%**
$\beta_{y_1y_3} + \beta_{x_2y_2}$	**15.76%**

techniques have been developed to solve computationally-expensive problems. These techniques are briefly reviewed in Appendix B, and the selected approach for this investigation is described below.

5.4.1 Optimization Approach Used in this Research, and Cases Investigated

In the optimization approach employed in this research, CFD is used as the simulation model for optimization of the design object. As such, in the optimization flowchart shown in Figure B.1, each evaluation of the optimization function, *f(x),* requires a solution of a CFD model of the flow around the design object. This CFD solution typically also involves a re-generation of the computational mesh for the design object.

Due to the intricacy of generating the computational mesh, it was found to be impractical to perform DES or even RANS computations as part of the optimization process. This is because the generation of a successful mesh for these types of solutions, particularly given the possible existence of sharp corners and interfaces in the virtual-duct configuration, is generally a complex undertaking that is difficult to automate without human supervision. Furthermore, due to limitations in computational resources for the investigation, the long computational times involved in even RANS solutions was deemed beyond the scope of the investigation. As such, all optimizations shown in this research were performed using only an ("low fidelity") Euler CFD solver. Specifically, optimizations were performed for two cases. First, an optimization was performed to determine the optimum shape of a downstream fairing for the canonical hemispherical-

turret-on-cylindrical-base configuration discussed in Section 5.1.1. In this case, due to the streamlined shape of the fairing, boundary-layer separations was assumed to be nonexistent (or unimportant) on the fairing so that the flow over the fairing is reasonably-well approximated by the Euler CFD simulation, especially in the upstream region of the fairing in the vicinity of the hemispherical turret. In addition to this fairing case, an optimization was also done for the shape of the virtual duct on a hemispherical turret. In this case, as shown in Chapter 4 and discussed previously in this chapter, a DES solution is required to accurately simulate the strength and effect of the streamwise vortices that form in the corners of the virtual duct. However, for low curvatures of the virtual duct, the corner vortices have a reduced effect and do not extend over much of the turret face; as such, the optimization is performed for only a low- to medium-curvature virtual duct with the Stratford criterion used to estimate boundary-layer separation as described in Section 5.2.1. The details and results of these optimizations are described in the following sections.

5.5 Fairing Optimization

As shown in Rennie (2010), a simple method of increasing the critical Mach number and eliminating flow separation on a spherical turret is to add a downstream fairing. In this regard, a fairing could be used to improve the aero-optic performance of either an underwing pod such as described in Chapter 2, or a canonical hemispherical turret. As a first step towards developing an aero-optic mitigation strategy, an optimization was first performed on the fairing shape for a canonical hemispherical

turret. Note that the fairing shapes shown in Figure 2.1 were more or less randomly selected, and are in no way optimized.

The optimization problem was formulated using the SQP method as described and presented in Appendix B. A basic design for the fairing, consisting of a cubic forebody that merges into an ogive tail, was assumed. With this basic design, the constraints on the variables consisted of setting x_1 on the front of the turret, x_2 downstream of the turret, and y_2 above the turret, see Figure 5.1. As the Design of Experiments screening study completed in Section 5.1.1 indicated, only x_1, x_2, and y_2 need to be included in the optimization routine while x_3 can be held constant. As such, x_3 was set at a constant value of 6.5D, which was judged sufficiently large to maintain the ogive-tail shape during the optimization. For this fairing-optimization study, it was also assumed that essentially any fairing would either eliminate or delay flow separation to a point at which the separated flow would not enter the field of regard of the optical system mounted in the spherical turret. As such, the optimization was performed only on the critical Mach number, which was formulated into the objective function. The overall problem in standard form was therefore:

$$\begin{aligned} &\min[min(-C_p)] \\ \text{s.t.}\quad &0.1D \leq x_1 \leq 0.5D\ , \\ &1.1D \leq x_2 \leq 3.0D, \text{ and} \\ &0.85D \leq y_2 \leq 1.6D. \end{aligned} \tag{5.6}$$

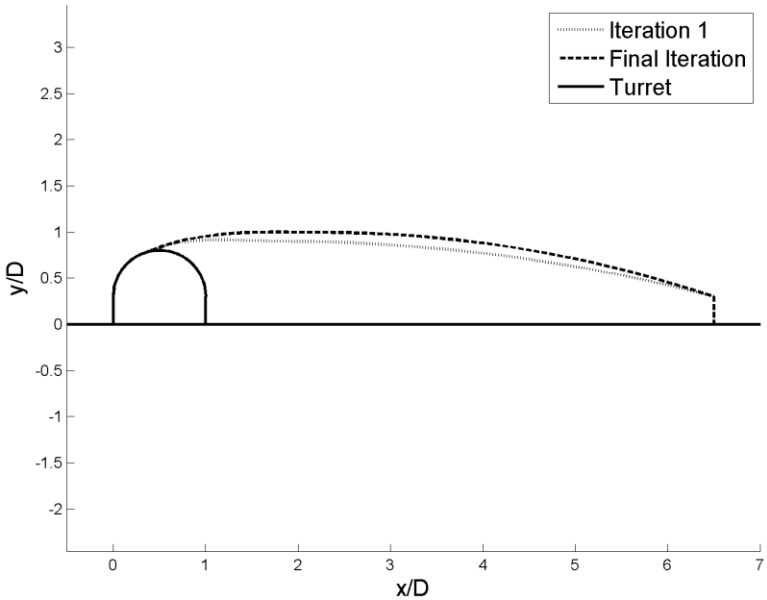

Figure 5.6. Comparison of 1st guess fairing shape to the optimal solution.

As stated before, an SQP algorithm was used to converge to an optimal design. The optimization began with an initial guess, which was chosen as a location near the middle of the feasible region: x_1 = 0.29D, x_2 = 1.8D, and y_2 = 0.9D (x_3 is constant at 6.5D). Based on these values, the gradient of the objective function, $\nabla f(x_k)$, was found by perturbing each variable by 10^{-4}D and computing the Euler solution for each parameter perturbation. The Hessian, $\nabla^2 f(x_k)$, was then computed using the Davidon-Fletcher-Powell (DFP) formula (Davidon 1991, Fletcher 1963). Equation (5.6) was simplified into a quadratic programming problem that was solved by the inherent Matlab function, quadprog. Once the quadratic programming problem was solved, the Wolfe condition, Equation (D.4), was used to decide if the new solution is better than

the previous solution. If it is not better, the step length was halved until a better solution was found. Once a better solution is found, the process was repeated by finding the derivative of the objective function and stepping through the optimization routine again. If a better solution is not found, then the optimization routine was assumed to have converged to an optimal shape and the program exits.

For this configuration an optimal solution was found in 7 iterations, consisting of 41 function evaluations. The first guess solution, pictured in Figure 5.6 with the final solution, had a critical Mach number of 0.723 while the final solution had a critical Mach number of 0.770. Although the change seems minimal, the increase in critical Mach number is significant and the optimal solution is able to delay the formation of shock waves at higher speeds than the initial guess. It should be noted that the optimization routine only looked at the minimum pressure in the region around the turret ($0.0 < x/D < 1.25$) and assumed that any shocks that form downstream on the fairing would not affect a beam leaving the turret. When comparing to Chapter 2 where a critical Mach number of 0.8 was found, it should be noted that the current model is for a turret that includes an extra D/3 base while the $M_{crit} = 0.8$ result from Chapter 2 was for a symmetric, streamlined pod. Since flow speeds over the top of a turret with D/3 base are slightly faster than at equivalent locations on a pod, it is more difficult to achieve higher M_{crit} for the turret on D/3 base configuration.

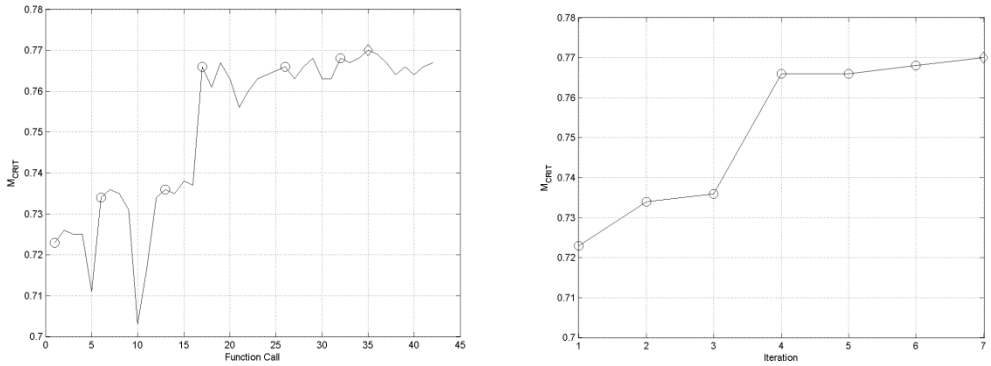

Figure 5.7 Critical Mach number for each function call (left) and iteration (right) for the fairing optimization. The optimal solution, found on function call 35 and iteration 7, is denoted by the diamond.

To get a better understanding for the results of each iteration and function call, Figure 5.7 shows the critical Mach number of each function call and iteration respectively. Figure 5.7 , Left, shows the function calls, defined as anytime an Euler run is completed for a fairing shape. Showing the number of function calls gives an idea of the length of an optimization routine, since each Euler run takes ~3 hours on 48 processors, multiplying this by the total function calls, 41, shows that it took 5.1 days to reach an optimal solution. It takes a total of 4 functional calls to compute a derivative (i.e. a 3-variable optimization needs 4 data points to compute the derivative for each variable), then if the Wolfe condition, Equation (B.1), is not satisfied, based on the initial step length, α, subsequent function calls are completed with smaller step lengths until a more optimal point is found. Figure 5.7 , Right, shows each iteration which is defined by each time the optimization routine finds a more optimal point. In this case it found 6 points with increasing optimality, until it finally converged on the optimal solution.

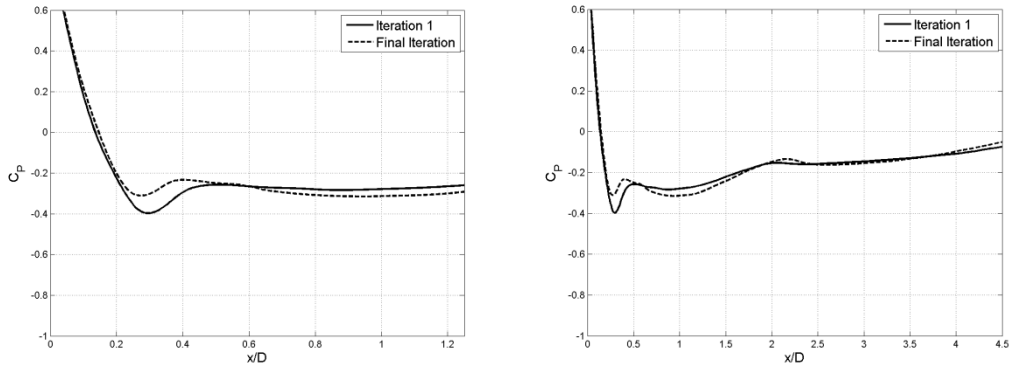

Figure 5.8. Pressure distribution over the front portion of the turret with fairing (left) and over the full fairing (right).

The pressure distribution for the optimized fairing is shown in Figure 5.8, and gives some insight into how the optimization process produces an optimum shape. Specifically, it is apparent that, in order to minimize the flow speed over the fairing, no point on the fairing should have a faster flow speed than another point on the fairing (otherwise the fairing shape could be adjusted slightly to reduce the speed at the high-speed point thereby resulting in a lower M_{crit} even if this adjustment resulted in an increase in the flow speed at another point on the fairing). In this regard, comparing the 1st iteration to the final iteration in Figure 5.8 shows that the optimization procedure has produced a more equal pressure distribution (and flow speeds) over the fairing. The local minimum in the C_p for the optimized distribution at x/D = 0.29 corresponds to the curvature of the hemispherical turret just upstream of the interface between the turret and the downstream fairing. By optimizing the location of this interface, and the local slope of the fairing at this location, the optimization procedure has maximized the M_{crit} for the fairing. Note that the pressure distribution in Figure 5.8 shows that the C_p at x/D

= 0.9 appears to be slightly lower than at x/D = 0.29; this difference shows that the fairing shape still could have been improved slightly, except that the optimization procedure may have been unable to do this possibly due to the grid resolution of the CFD models.

5.6 Virtual Duct Optimization

With the success of the fairing optimization, an optimization was also performed for the flow over a turret with a virtual duct. A preliminary investigation of the design space is presented in Appendix C that gives a good understanding of how different fence shapes affect the adverse pressure gradient. For the virtual-duct optimization, the critical Mach number was set as a constraint while the optimization was used to maximize the downstream location of the flow separation. The location of separation was defined by the elevation angle, α_0, of the point on the turret at which the Stratford criterion, Equation (5.4), became greater than one:

$$\alpha_0 \; when \; \frac{C_p' \sqrt{x \frac{dC_p'}{dx}}}{0.39(\frac{Re}{10^6})^{0.1}} > 1, \tag{5.7}$$

As such, the objective function for the optimization was:

$$\max \alpha_0 \tag{5.8}$$

where α_0 is defined as the elevation angle when the Stratford criterion is first satisfied.

As shown in the Design of Experiments study, Section 5.2, only the variables y_1, x_2, y_2, and y_3 have a strong effect on the performance of the virtual duct; as such, x_1 and x_3 were kept constant for the optimization, specifically, values of x_1= 0.25D and

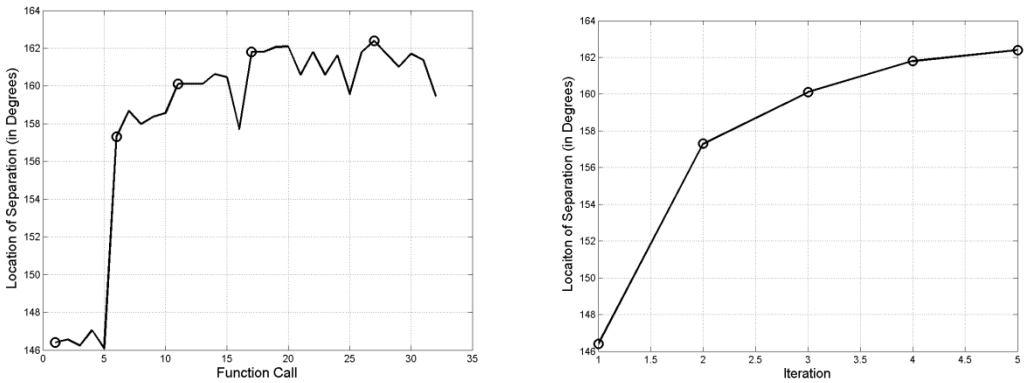

Figure 5.9. The location of separation for each function call (left) and iteration (right) for the virtual duct optimization. The optimal solution is found on function call 27 and iteration 5.

x3=0.765D were selected; these points were selected arbitrarily, however, they are fairly close to the locations of the inlet and outlet to the virtual duct tested experimentally in Chapter 3.

The variables of interest, y_1, x_2, y_2, and y_3, were constrained such that x_2, is located downstream of x_1 and upstream of t x_3:

$$x_1 - x_2 \leq -0.05D,$$
$$x_2 - x_3 \leq -0.05D. \tag{5.9}$$

Furthermore, the y_2 location must be further from the turret centerline than y_1 and y_3 in order for the virtual-duct fences to have the correct diffusing and contracting regions:

$$y_1 - y_2 \leq -0.015D,$$
$$y_3 - y_2 \leq -0.015D. \tag{5.10}$$

Another constraint on the virtual-duct fences is that they cannot be located too close to the centerline or else they would block the outgoing beam; therefore the minimum value must be greater than 0.17:

$$y_i \leq -0.17D \quad \text{for i = 1, 2, and 3,} \tag{5.11}$$

and that each fence point must be located on the turret:

$$\sqrt{(x_i - 0.5D)^2 + y_i^2} \leq 0.45D \text{ , for i = 1, 2, and 3.} \tag{5.12}$$

A further constraint was placed on the curvature ratio of the virtual duct, R/B, based on the limitations of the Euler/Stratford approach discussed above. Specifically, the radius of curvature of the virtual duct was limited to values greater than 1.2, which was judged to be sufficiently low (based on the results of Section 5.2) that corner vortices formed in the virtual duct would not significantly influence the flow in the duct. Finally, as stated above, the critical Mach number was constrained to be greater than 0.7. Since the value for the critical Mach number is not known until after a function call is completed, a penalizing method is used to account for this constraint. If a function produces a critical Mach number below 0.7, the separation location, i.e. objective function, is moved forward:

$$\begin{gathered} \alpha_0 = \alpha_0 - 100(0.7 - M_{crit}) \text{ for } M_{CRIT} < 0.7 \\ \alpha_0 = \alpha_0 \text{ for } M_{CRIT} > 0.7 \end{gathered} \tag{5.13}$$

In summary, a statement of the overall optimization problem in standard form is:

$$\begin{gathered} \max \alpha_0 \\ \text{s.t.} \quad M_{CRIT} > 0.7 \end{gathered} \tag{5.14}$$

$$x_1 - x_2 \leq -0.05D,$$

$$x_2 - x_3 \leq -0.05D,$$

$$y_1 - y_2 \leq -0.015D,$$

$$y_3 - y_2 \leq -0.015D,$$

$$\sqrt{(x_i - 0.5D)^2 + y_i^2} \leq 0.45D \text{ , for i = 1, 2, and 3, and}$$

$$y_i \leq -0.17D \quad \text{for i = 1, 2, and 3.}$$

The optimization problem described in Equation (5.14) was solved using the Euler routines contained in AVUS. The initial parameter values were arbitrarily selected to be (x_1,y_1) = (0.25D,0.23D), (x_2,y_2) = (0.45D,0.30D), and (x_3,y_3) = (0.765D, 0.19D). These initial parameters gave a virtual duct shape that had a critical Mach number of 0.728 and a location for separation of 146.4°. Note that the value of 146.4° is similar to the separation location found for the high curvature-ratio case shown in Figure 5.5.

The optimization problem converged to an optimal solution with a critical Mach number of 0.75 and a location for separation at an elevation angle of 162.4°. The optimized solution was achieved after 32 function calls and 5 iterations, which required 8 days using 72 processors. The value of the location of separation for each iteration and function call is shown in Figure 5.9. The non-circled points are the function calls that consist of 5 function calls to compute the derivative and the associated calls for each iteration while the optimization routine “hunts” for a better location in which to move the design. Once the better location is found, the next iteration begins with the circled points. Similar to the fairing, large increases in the location of separation appear in the

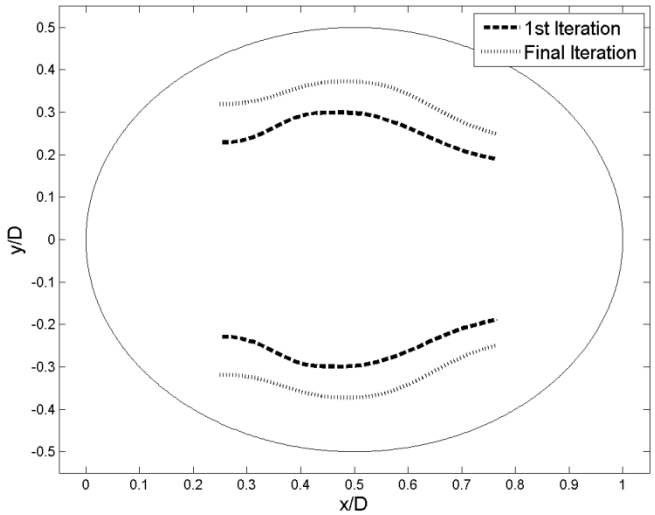

Figure 5.10. Virtual duct shape for the 1st and last iteration.

early iterations, while the fine tuning occurs in the later iterations. Note that, although the separation of 146.4° for the initial guess is a significant improvement on the 120° separation location of a canonical turret, Figure 5.9 shows that this initial guess is nowhere near optimum. As such, a designer may have been tempted to use this first guess and settle on a separation location of 146.4°; however, by performing an optimization routine, a superior virtual-duct shape is obtained with a separation location of nearly 162.4°.

A comparison of the virtual-duct shapes for the initial and final optimization iterations is shown in Figure 5.10. The figure shows that the optimization process has moved the location of the widest point on the virtual duct (point 2 in Figure 5.2) slightly downstream. However, perhaps the most interesting detail of Figure 5.10 is that the fence shapes for the initial and final iterations are actually relatively similar and that the

main effect of the optimization has been to move the virtual-duct fences outward on the turret. Although the most likely effect of this outward shift of the virtual-duct fences would be to entrain more flow into the virtual duct, a designer would probably not find this improved design except by chance due to the difficulty in developing an intuitive feel for how the virtual duct affects the flow over the curved surface of the turret. As such, the virtual-duct shapes in Figure 5.10 further demonstrate the advantage conferred by the optimization process.

Figure 5.11, left, shows a comparison of the pressure distribution for the first and last iterations. Significantly, the optimized solution has moved the minimum pressure location on the turret almost 40° further downstream. This downstream shifting of the minimum pressure location also moves the adverse pressure gradient farther downstream and results in a delay of boundary-layer separation as shown on the right side of Figure 5.11. The plot of the Stratford condition in Figure 5.11, right, also

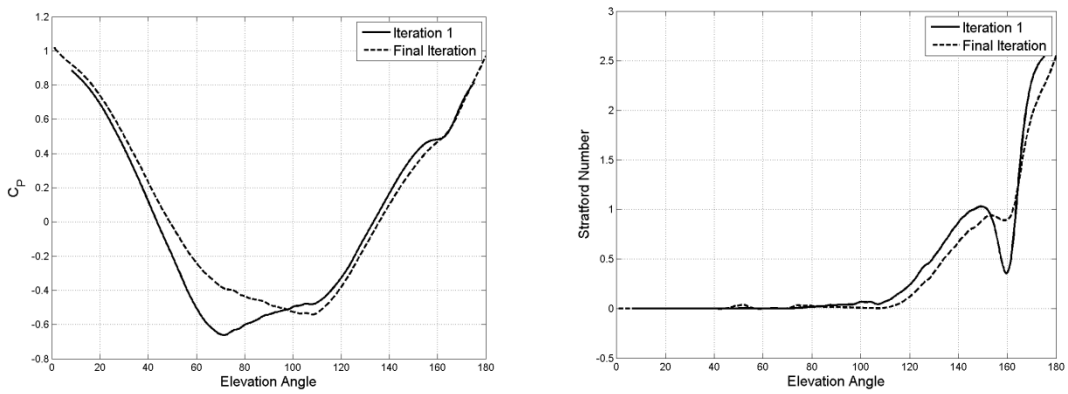

Figure 5.11. The pressure distribution inside of the virtual duct for the initial guess and the optimized fence.

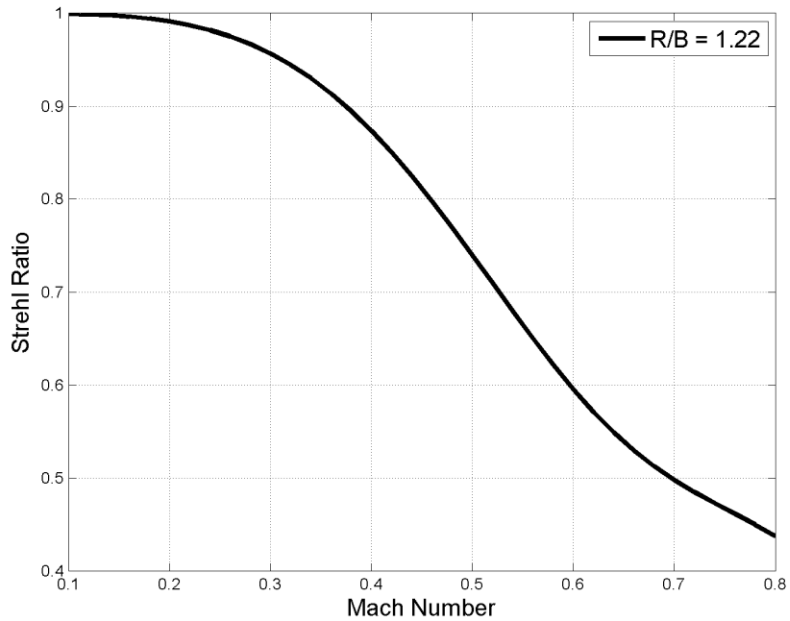

Figure 5.12. Strehl Ratio as function of Mach number for the curvature ratio, 1.22, of the optimized virtual duct shape.

indicates that the 145° location, coinciding with the outlet of the virtual duct, is a critical region for separation. This result highlights the effect that the outlet of the virtual duct has on the location of separation, and suggests that the separation location might be delayed still further by moving the outlet of the virtual duct even further rearward.

The final location of (x_1,y_1) = (0.25D,0.32D), (x_2,y_2) = (0.485D, 0.37D), and (x_3,y_3) = (0.765D, 0.25D) corresponds to a curvature ratio of 1.22. For this curvature ratio, a plot of the Strehl Ratio as a function of freestream Mach number is shown in Figure 5.12. The Strehl ratios shown in the figure were calculated using the same procedure described in Section 4.7. Note, however, that due to the optimized fence locations being farther away from the turret centerline (i.e., the optimized fence locations are

approximately 0.08D wider than the beam aperture), the corner vortices from the fences would also be located farther from the optical aperture. Specifically, the estimated location of the corner vortices is adjusted to be roughly 0.05 A_D to the side of the edge of the aperture, and this location for the corner vortices was used to compute Figure 5.12. This adjustment was estimated based on the fence outlet, y_3, being 0.25D from the centerline instead of 0.19D used in Chapter 4. As such, the fact that the optimization shows that wider virtual-duct fences result in better performance is a particularly important result since it also means that the corner vortices from the fences would be located farther from the optical aperture and hence would have a reduced effect on the performance of the virtual duct. Due to the wider virtual duct, the computed Strehl Ratios in Figure 5.12 are over 0.45 up to M_∞= 0.8 and over 0.6 up to M_∞= 0.6.

5.7 Conclusions

The Design of Experiments study helped to minimize the variables needed in the optimization routines. Although some assumptions were made, the final results proved to be reasonable. With the understanding of the important variables, an optimization of the fairing and the virtual duct was completed. The fairing optimization converged on a shape that increased the critical Mach number of a canonical hemispherical turret with D/3 base to 0.77, which is a significant improvement on the M_{crit} of 0.55 for a turret without a fairing. For the virtual duct, the optimization process also produced a superior design that moved the point of minimum pressure/maximum flow speed

farther downstream, thereby delaying the start of the adverse pressure gradient on the turret and hence delaying boundary-layer separation. This optimized virtual-duct design moved the separation location downstream from an elevation angle 120° for a canonical turret to 162.4° for a turret with a virtual duct, while also increasing the critical Mach number from 0.55 for a turret to 0.75 for a turret with a virtual duct. Significantly, the virtual-duct optimization also showed that better performance is achieved if the fences of the virtual duct are moved farther out on the turret. This wider spacing of the duct fences has the added benefit of also moving the corner vortices farther out and hence farther away from the optical aperture, thereby reducing the aberrating effect of the vortices themselves.

CHAPTER 6:

SUMMARY AND RECOMMENDATIONS

This dissertation has described an investigation into the "virtual duct" concept, in which fences are mounted on a spherical turret with the purpose of mitigating or eliminating aero-optic aberrations by increasing the critical Mach number and delaying boundary-layer separation in the vicinity of the optical aperture. The following are the major findings of the investigation:

- The ability of the virtual duct to delay boundary layer separation was successfully demonstrated experimentally, as described in Chapter 3. Depending on the curvature of the duct, the flow visualization studies showed that the flow remained attached up to an elevation angle of 160°. These experiments were conducted using a turret with Re_D greater than the critical Re_D for a sphere; so that a turbulent boundary layer existed on the turret.
- Streamwise vortices were experimentally shown to form in the corners of the virtual duct. A CFD study was performed to develop a physics-based explanation for the cause of the vortices, based on previous research into flow in river channels, as well as a model to estimate the strength of the corner vortices as a function of the shape of the virtual duct.

- A simple method was developed based on previous work by Porter (2011b) to estimate the optical effect of the streamwise corner vortices. The effect of the corner vortices on the farfield irradiance pattern of an outgoing beam was computed using the Fraunhoffer Equation, Equation (1.2) as a function of vortex parameters.
- A low-fidelity method for predicting boundary layer separation on a turret with a virtual duct was developed that uses only the Euler equations along with the Stratford criterion, Equation (5.4). This method gave a reasonable comparison to experimental results for comparable geometries.
- Optimization methods for a fairing and virtual duct were developed and successfully demonstrated in Chapter 5. These optimization studies showed that adding a faring to a turret can raise M_{crit} to at least 0.77. The virtual-duct optimization showed that a virtual duct can be developed with M_{crit} of at least 0.75 that delays separation to 162.4°. The virtual-duct optimization achieved this increase in performance while constraining the virtual-duct curvature to a sufficiently-low value that the corner vortices produced in the virtual duct would remain relatively weak. The virtual-duct optimization showed that better performance is achieved if the fences of the virtual duct are moved farther out on the turret. This wider spacing of the duct fences has the added benefit of also moving the corner vortices farther out and hence farther away from the optical aperture, thereby reducing the aberrating effect of the vortices themselves.

The following recommendations are made for future work:

- The optimization study described in this research was performed for only a single location of the inlet and outlet of the virtual duct. This was done because the DoE study indicated that the virtual-duct inlet and outlet locations, x_1 and x_3, had only a minor effect on the performance of the virtual duct with regards to delaying boundary-layer separation. However, there is some evidence that the virtual-duct outlet can have a substantial effect on the boundary-layer separation location as evidenced by the rapid increase in the Stratford criterion near the virtual-duct outlet as shown in Figure 5.5. As such, additional optimization studies could be performed using different inlet and outlet locations of the virtual duct to more fully evaluate the effect of x_1 and x_3 on the performance of the virtual duct. For these studies, the outlet of the virtual duct could be moved farther downstream, or even off the rear of the turret.
- The optimizations described in this investigation were completed using low-fidelity Euler equations combined with a pressure-based method of predicting boundary-layer separation. This approach was implemented primarily due to limitations in the available computational resources. As such, further investigations could be performed using more powerful CFD resources. Specifically, the fairing optimization would benefit from CFD with finer resolution gridding along with using a structured grid to better resolve the flow speeds near the surface of the fairing. The virtual-duct optimization could also be performed using a true multi-fidelity optimization, described in Appendix B, in which the Euler/Stratford approach is used as a low-fidelity model and a high-fidelity DES

CFD solution is computed periodically to correct the low-fidelity solutions. Furthermore, work could be done to eliminate the need for human interaction in the gridding of the high fidelity solutions to obtain a fully-automated optimization procedure.

APPENDIX A:

EXPERIMENTAL CORRECTIONS

A.1 Blockage Correction

To correct for the blockage in the wind tunnel a solid blockage correction equation was taken from Maskell (1963). Taking C_P equations for the measured and corrected values,

$$C_{P_m} = 1 - \left(\frac{V_m}{V_\infty}\right)^2 \tag{A.1}$$

and

$$C_{P_c} = 1 - \left(\frac{V_c}{V_\infty}\right)^2, \tag{A.2}$$

and setting the mass flow into the control volume, before the experimental model is introduced, equal to the mass flow out of the control volume, at the pod's maximum diameter of 0.3048 m (12 inches),

$$\rho_m V_m (A_{ts} - A_{model}) = \rho_c V_c (A_{ts}). \tag{A.3}$$

Substituting Equations (A.1) and (A.2) into Equation (A.3), and setting $\rho_m = \rho_c$, the equation for the corrected C_{Pc} is found to be

$$C_{P_c} = 1 - \left(1 - C_{P_m}\right) \cdot \left(\frac{A_{ts} - A_{model}}{A_{ts}}\right)^2. \tag{A.4}$$

This equation only corrects for solid blockage, corrections due to buoyancy and wake blockage have been neglected. Buoyancy blockage is neglected because the model is placed close to the inlet of the test section; therefore the boundary layer has had little growth by the time it reaches the turret ball. Wake blockage is neglected since the model is aerodynamic and there is little separation on the body.

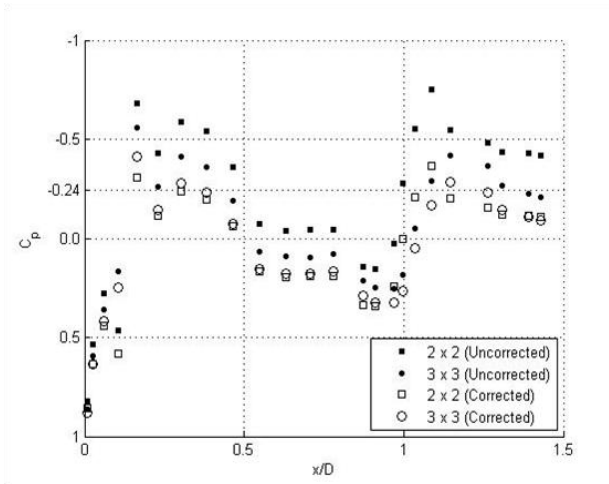

Figure A.1. Pressure distribution for 20° lookback angle with a regular fence height showing that the blockage correction converges to a similar solution for both wind tunnels (Crahan 2011).

To verify that the correction equation is correct, pressure measurements from the three foot by three foot test section are compared to that of the two foot by two foot test section. Since each run was done using the same model and at the same flow speed, the result converges to a similar solution as shown in Figure A.1. Looking at the 4th and 5th points, they do not follow the trend of the data. This is due to the boundary layer trip that was placed in this region to make sure the flow is turbulent over the sphere. These experimentally found pressure distributions are shown for a 20° lookback

configuration with a regular fence height. These tests were conducted in a slightly different configuration and are presented only to prove the convergence of the blockage correction equation. The experimental data presented in Chapter 2 is for a corrected configuration that has the stagnation point on the nose of the turret ball.

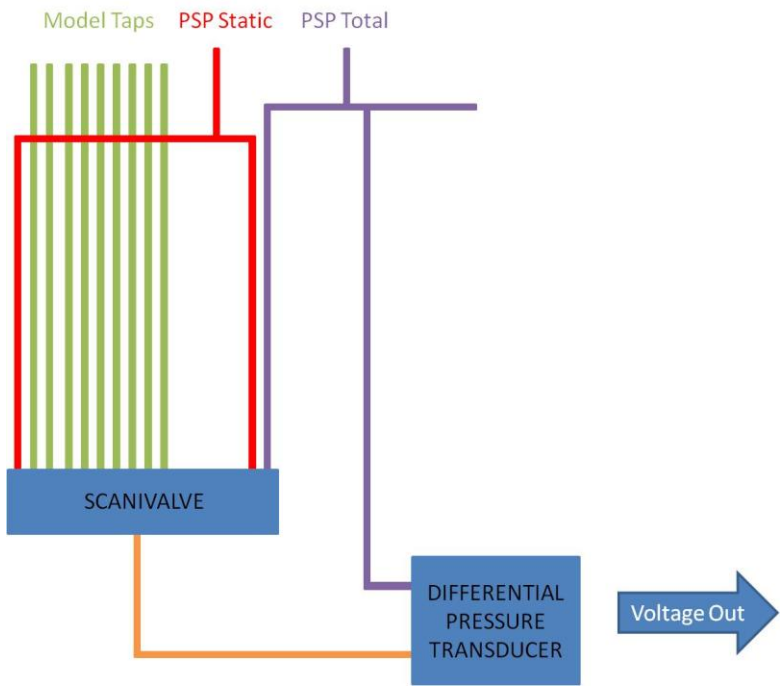

Figure A.2. Overview of pressure measurement based on the pressure taps on the model and the pressure values measured with a pitot static probe.

A.2 Pressure Calibration

The voltage output from the differential pressure transducer is used in combination with a scanivalve to calibrate to transducer to calculate the coefficient of pressure at each tap location. To complete this a scanivalve, a pressure transducer, and a pitot static probe (PSP) are used following the set-up shown in Figure A.2. The

scanivalve is set-up so that the first port is connected to the static tap on the PSP, then each model tap is connected to the scanivalve in order. Once all model taps are connected, the static tap from the PSP is connected again followed by the total pressure tab. The output of the Scanivalve is connected to one side of the differential pressure transducer and compared to the total pressure from the PSP. As such, the output from the pressure transducer has N+3, where N is the number of model taps, voltage readings. To calibrate the voltage reading to a pressure coefficient, the voltage reading is turned into a pressure value by:

$$Voltage = \alpha(\Delta P) + \beta \tag{A.5}$$

where α and β are arbitrary calibration constants. Therefore the pressure measurements comparing the total pressure to the model taps is:

$$Voltage_{Total-N} = \alpha(P_{Total} - P_N) + \beta \tag{A.6}$$

where N represents the model tap number. The pressure measurements comparing the total pressure from the PSP to the static pressure from the PSP is:

$$Voltage_{Total-Static} = \alpha(P_{Total} - P_{Static}) + \beta. \tag{A.7}$$

The pressure measurements comparing the total pressure from the PSP to the total pressure from the PSP is:

$$Voltage_{Total-Total} = \alpha(P_{Total} - P_{Total}) + \beta. \tag{A.8}$$

This difference in this last value is the total pressure through the scanivalve compared to the total pressure connected directly to the transducer.

To calculate the pressure coefficient, the readings are set-up as:

$$C_P = \frac{Voltage_{Total-Static} - Voltage_{Total-N}}{Voltage_{Total-Static} - Voltage_{Total-Total}} \tag{A.9}$$

and substituting Equations (A.6)-(A.8) into Equation (A.9):

$$C_P = \frac{\alpha(P_{Total} - P_{Static}) + \beta - [\alpha(P_{Total} - P_N) + \beta]}{\alpha(P_{Total} - P_{Static}) + \beta - [\alpha(P_{Total} - P_{Static}) + \beta]}. \tag{A.10}$$

Rearranging and canceling out the arbitrary calibration constants simplifies the C_P to be

$$C_P = \frac{P_{Total} - P_{Static} - P_{Total} + P_N}{P_{Total} - P_{Static} - P_{Total} + P_{Total}} = \frac{P_N - P_{Static}}{P_{Total} - P_{Static}}, \tag{A.11}$$

which is equal to the pressure coefficient (Schlicting 1979):

$$C_P = \frac{P - P_\infty}{{}^1/_2\, \rho_\infty v_\infty^2}. \tag{A.12}$$

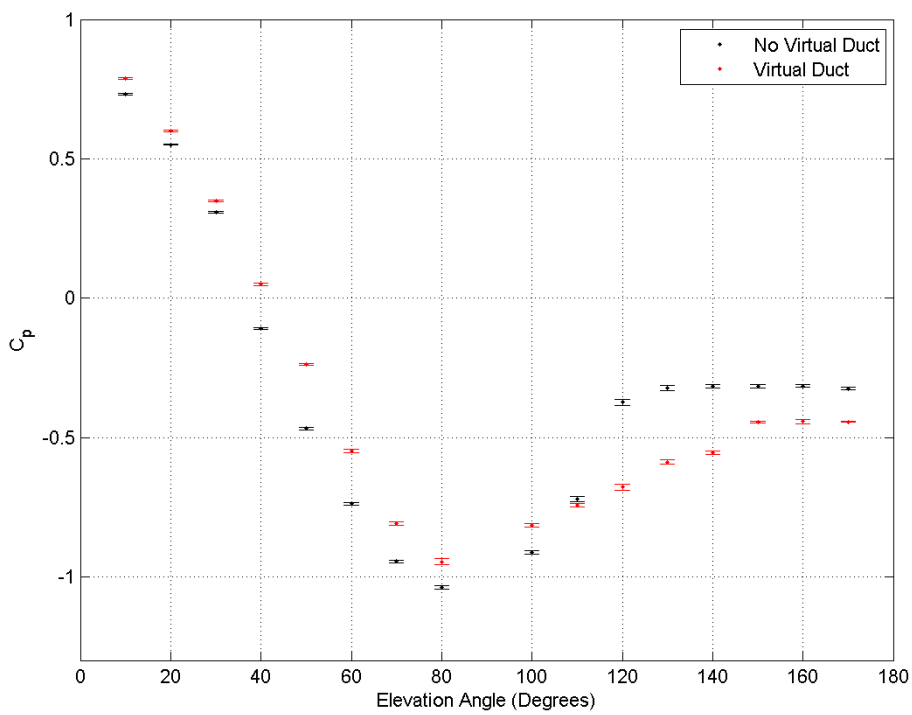

Figure A.3. Data in Figure 3.6 showing the 95% confidence intervals.

A.3 95% Confidence Intervals

In order to understand the repeatability of the pressure measurements, 95% confidence interval bars are shown for Figure 3.6 where the experimental pressure data is shown for a low-curvature virtual-duct compared to a turret without a virtual duct. The error bar measurements are calculated using

$$\bar{x} \pm z\frac{\sigma}{\sqrt{n}} \tag{A.13}$$

where z is 1.96 for a 95% confidence interval calculation. Each average tap measurement, i.e. values shown Figure 3.6, consists of the average of 10 different measurements. As such the sample size, n, is 10 and the standard deviation is taken from these 10 values. It should be noted that each different measurement actually consists of 2050 samples over 0.5 seconds that are averaged while the experiment is taking place. Figure A.3 shows the error bars for the 2 different wind tunnel tests shown in Figure 3.6. These error bars are relatively small in that they do not overlap in the regions where the pressure is increasing and decreasing.

APPENDIX B:

OVERVIEW OF OPTIMIZATION

Optimization methods are categorized into several different types of problems beginning with the most basic single-variable optimization up to unconstrained and constrained multivariable optimization and even multi-objective optimization. Different types of global optimization techniques involve integer programming and genetic algorithms.

Most gradient-based optimization methods have a common structure. Each method involves an initial design, x_0, a search direction, d_0, and a step size, α_0. This way the next design location can be found by solving:

$$x_{k+1} = x_k + \alpha_k d_k, \tag{B.1}$$

where k represents the current iteration and k+1 is the next iteration. Gradient-based numerical methods are characterized by the different ways they determine the search direction, d_k (Tovar 2010). The step size, α_k, is found by solving a single-variable optimization problem. Methods for using the search direction include the steepest descent method (Cauchy 1847), conjugate gradient methods, and, if the Hessian matrix can be computed, Newton methods. Even if the Hessian cannot be found, the Davidon-Fletcher-Powell (DFP) formula has been developed to estimate the Hessian matrix (Davidon 1991, Fletcher 1963). A trust region method has also been developed that

does not use the step size, instead it uses only the search direction, d_k, and limits the solution to a certain region.

Constraints are added to the optimization problem to restrict the objective function to certain conditions. The standard form of an optimization problem is stated as:

$$\min_{x} f(x)$$
$$\textit{subject to} \quad g(x) \leq 0 \tag{B.2}$$
$$h(x) = 0$$

where *f(x)* is the objective function, *g(x)* is the inequality constraint, and *h(x)* is the equality constraint of the objective function.

For this investigation, a Sequential Quadratic Programming (SQP) algorithm was selected. SQP methods generate design improvements by solving quadratic programming (QP) subproblems. This approach can be used both in line search or trust-region frameworks (Nocedal 2006). SQP methods deliver a high order of convergence and are suitable for solving problems with significant nonlinearities (Tovar 2010).

The SQP method begins by formulating the non-linear problem in quadratic form. This is done by computing the derivative, $\nabla f(x_k)^T$ and the Hessian, $\nabla^2 f(x_k)^T$, of the objective function for each variable for the current point x_k. Then a new optimization problem is solved to find the search direction, d_k. The constraints are also put in a standard quadratic form by taking their values and derivatives at x_k. The new optimization problem to find the search direction, d_k, for the current point, x_k, in standard form is:

$$\min_{d_k} \nabla f(x_k)^T d_k + \frac{1}{2} d^T \nabla^2 f(x_k)^T d_k$$

$$s.t. \quad g(x_k) + \nabla g(x_k)^T d_k \leq 0 \qquad \text{(B.3)}$$

$$h(x_k) + \nabla h(x_k)^T d_k = 0$$

where "s.t." stands for "subject to." To decide the search distance, the Wolfe Condition (Wolfe 1969) is used. The Wolfe Condition forces a reduction in $f(x_k)$ that is proportional to both the step length, α_k, and the directional derivative $\nabla f(x_k)^T d_k$ where d_k is found from solving the optimization problem, Equation (B.3). In order for a new point to be considered more optimal it must produce a value of the optimization function that is

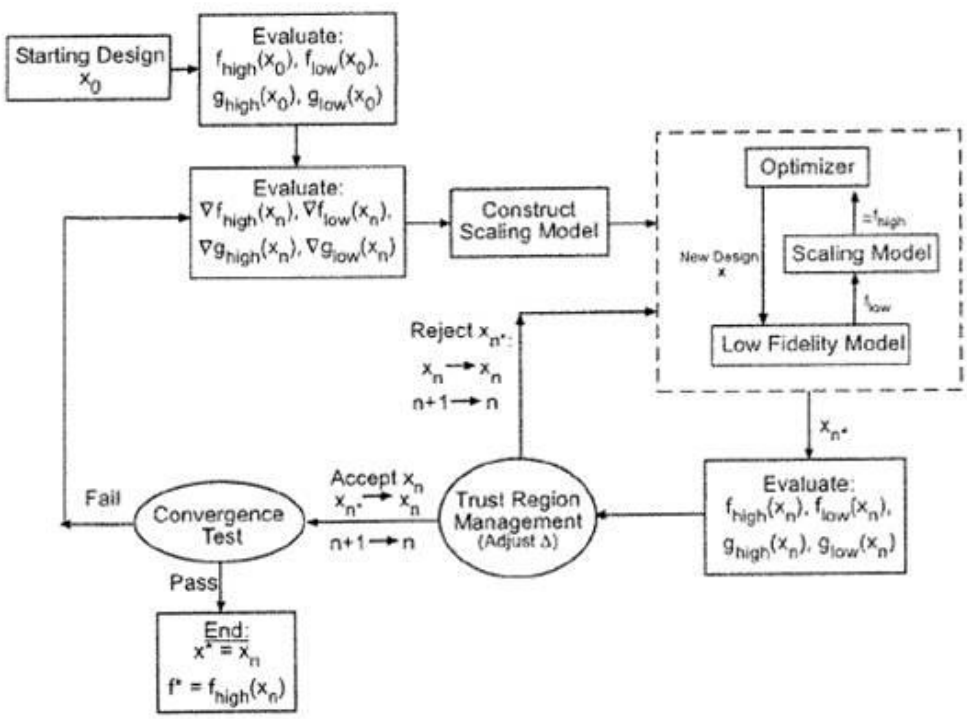

Figure B.1. Variable fidelity framework flowchart (Gano 2004).

less than the current value plus the directional derivative multiplied by a constant:

$$f(x_k + \alpha_k d_k) \leq f(x_k) + c_1 \alpha_k \nabla f(x_k)^T d_k \,. \tag{B.4}$$

The value of c_1 is recommended to be very small, in the present study, it was set to 10^{-4} (Nocedel 2006). The step size, α_k, was set to 0.5^k so that the step size is constantly decreasing with each iteration. Once the equality in Equation (B.4) is satisfied the new point is:

$$x_{k+1} = x_k + \alpha_k d_k \,, \tag{D.5}$$

and the process is repeated until an optimal design is found.

B.1 Variable-Fidelity Optimization

The optimization process can involve a large number of function calls to converge to a solution, therefore to converge to an optimum more rapidly; a variable fidelity method can be used. Variable-fidelity methods have been developed to solve optimization problems that involve simulations with extreme computational expense. A higher fidelity model is one that contains physics or details that are not accounted for in a lower fidelity model (Gano 2004). As an example, for the optimization of the virtual duct, a low-fidelity model might use the Euler equations while a higher-fidelity model might use DES CFD. In this case, the optimization can be performed more rapidly with the low-fidelity function calls which are periodically improved using a more computationally-expensive higher-fidelity simulation. Figure B.1 shows a sample flowchart of a variable-fidelity optimization routine.

To perform this variable-fidelity optimization, the initial values and derivatives are calculated at the initial point, x_k, using the high- and low-fidelity simulations. Then a scaling model is constructed to ensure matching between the different fidelity models and an optimization iteration is completed using the low fidelity model. Once a more optimal location is found, the new point, x_{k+1}, is evaluated for its value and its derivatives to construct a new scaling model. This process is repeated until an optimum location is found.

B.2 Sequential Quadratic Programming Code

The code used to perform the SQP algorithm for the optimization routine is shown below with comments.

```
clc
clear all
close all

Hessian = 'dfp';
iter(1).x(1,:)=[0.229 0.45 0.299 0.189]; %Initial Guess

delX = 10^-4;
i = 1;
errorOut = 1;
[R C] = size(iter(1).x(1,:));
qq = 1;
q = 1;
gamma = 10^-4;
iter(i).f(1) = objective_F(iter(i).x(1,:),delX,i); %Initial computation of objective function
while errorOut > 10^-10
        %Compute the derivative of each variable using forward Euler
        for jj = 1:C
           iter(i).x(jj+1,:) = iter(i).x(1,:);
           iter(i).x(jj+1,jj) = iter(i).x(1,jj) + delX;
                    iter(i).f(jj+1) = objective_F(iter(i).x(jj+1,:),delX,i);
```

```
        end
        iter(i).dF = objective_der_InputF(iter(i).f,delX)';

        %Compute the Hessian using the previously specified formula
        if strcmp(Hessian,'exact')
            iter(i).ddF = DDF(iter(i).x(1,:),delX);
        elseif strcmp(Hessian,'dfp')
            if i == 1
                iter(i).ddF = eye(C);
                iter(i).ddFInv = eye(C);
            else
                iter(i).y = iter(i).dF - iter(i-1).dF;
                iter(i).yT = transpose(iter(i).y);
                iter(i).sT = iter(i).x(1,:) - iter(i-1).x(1,:);
                iter(i).s = transpose(iter(i).sT);
                iter(i).ddFInv = iter(i-1).ddFInv - ((iter(i-1).ddFInv * iter(i).y * iter(i).yT *
iter(i-1).ddFInv)/(iter(i).yT * iter(i-1).ddFInv * iter(i).y)) + ((iter(i).s * iter(i).sT)/(iter(i).sT *
iter(i).y));
                iter(i).ddF = inv(iter(i).ddFInv);
            end
        elseif strcmp(Hessian,'bfgs')
            if i == 1
                iter(i).ddF = eye(C);
                iter(i).ddFInv = eye(C);
            else
                iter(i).y = iter(i).dF - iter(i-1).dF;
                iter(i).yT = transpose(iter(i).y);
                iter(i).sT = iter(i).x(1,:) - iter(i-1).x(1,:);
                iter(i).s = transpose(iter(i).sT);
                iter(i).ddFInv = iter(i-1).ddFInv - (((iter(i).s * iter(i).yT * iter(i-1).ddFInv) +
(iter(i-1).ddFInv * iter(i).y * iter(i).sT))/(iter(i).sT * iter(i).y)) + (1 + ((iter(i).yT * iter(i-
1).ddFInv * iter(i).y)/(iter(i).sT * iter(i).y)))*((iter(i).s * iter(i).sT)/(iter(i).sT * iter(i).y));
                iter(i).ddF = inv(iter(i).ddFInv);
            end
        end
        iter(i).g = Constraints_H(iter(i).x(1,:),delX)
        iter(i).dg = Constraints_DH(iter(i).x(1,:),delX)

        %Solve the quadratic programming problem for the quadratic approximation of
the objective function
        options = optimset('Algorithm','active-set')
        iter(i).dQ = quadprog(iter(i).ddF,iter(i).dF,iter(i).dg,-iter(i).g,[],[],[-20 -20 -
20],[20 20 20],transpose(iter(i).x(1,:)),options);
```

```
%Check if new location is more optimal using Wolfe Condition
 q = i;
 iter(i).dQNorm = 0;
 for j = 1:C
    iter(i).dQNorm = (iter(i).dQ(j))^2 + iter(i).dQNorm;
 end
 iter(i).WolfeRHS = iter(i).f(1) - gamma*(0.5^q)*sqrt(iter(i).dQNorm);

 WolfeCond = 1;
 while WolfeCond == 1 && q < 10;
    for j = 1:C
       iter(i).WolfeTest(j) = iter(i).x(1,j) + (0.5^q)*iter(i).dQ(j);
    end
    %Compute at new location until Wolfe Condition is satisfied
    iter(i).WolfeLHS(q) = objective_F(iter(i).WolfeTest,delX,i)
    if iter(i).WolfeLHS(q) < iter(i).WolfeRHS
       WolfeCond = 0
    else
       q = q+1
    end
 end

 if q == 10
        %If not satisfy Wolfe Condition, optimum is found!
        [iter(i+1).f(1) ind] = min(iter(i).f);
        iter(i+1).x(1,:) = iter(i).x(ind,:);
 else
        %If Satisfy Wolfe Condition, Set new guess and iterate
         iter(i+1).f(1) = iter(i).WolfeLHS(q);
        iter(i+1).x(1,:) = iter(i).WolfeTest;
 end

 error = 0;

 for j = 1:C
    error = (iter(i+1).x(1,j) - iter(i).x(1,j))^2 + error;
 end

 qq = qq + 1;
 i = i + 1;
 x1x2(i,:) = iter(i).x(1,:);
 errorVec(i-1) = error;
```

```
    errorOut = error
end

qq
fVal = iter(i-1).f
```

APPENDIX C:

PRELIMINARY STUDY OF VIRTUAL DUCT

C.1 Investigation of the Design Space

Prior to the optimization, an initial study was completed to understand the virtual duct design space for flows around a hemispherical-turret-on-cylindrical-base configuration, where the two main causes of optical aberrations are shock waves and flow separation (Crahan 2010). As discussed above, shock formation on the turret can be avoided by keeping the minimum C_{P0} on the turret as large as possible. Since the adverse pressure gradient is a major factor in determining boundary-layer separation, a closer look into the adverse pressure gradient was completed as a preliminary study to understand how different fence shapes affect separation. The region of interest for the adverse pressure gradient was chosen to begin at x/D = 0.4 (elevation angle of 78°), and to extend sufficiently far downstream to enable a maximum lookback angle of 40°. For a typical turret design in which the aperture is $1/3^{rd}$ the diameter of the turret, Figure C.1 shows that this criterion means that the boundary layer must remain attached up to x/D = 0.91 (elevation angle of 145°). It should be noted that the maximum lookback angle of 40° was chosen arbitrarily; however, since flow separation on a spherical turret normally occurs at only 30° past vertical, Figure C.1 shows that minimizing the adverse pressure

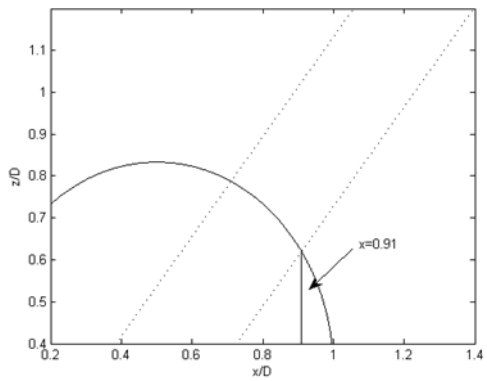

Figure C.1. Side view of turret showing lookback angle of 40° (Crahan 2010).

gradient in an attempt to prevent boundary-layer separation over the range *x/D* = 0.4 to 0.91 would represent a significant improvement over the canonical hemisphere-on-cylinder turret case.

Based on the above discussion, the pressure gradient is defined as

$$\sum\left\{\left|\frac{d}{dx}C_P\left(\frac{x}{D}\right)\right|\right\} \tag{C.1}$$

where C_P is the pressure coefficient. To deal with CFD data at discrete points, x_i/D, the adverse pressure gradient was re-written as

$$\sum\left\{\left|\frac{C_P\left(\frac{x_i}{D}\right)-C_P\left(\frac{x_{i-1}}{D}\right)}{x_i-x_{i-1}}\right|\right\}. \tag{C.2}$$

C.2 Design Variables

The objective of the initial work was to understand how the shape of the fence affects the pressure gradient on the rear of the turret by trying different combinations

for the locations of the points 1, 2, and 3 shown in Figure 4.10. From the underwing pod study, it is known that higher fence heights increase the critical Mach number; however, to simplify the CFD computations for this study, the height was set to a constant at 1.2D. In summary, six design variables were used: x_1, y_1, x_2, y_2, x_3, and y_3.

C.3 Constraints

The main constraint on the system is the lower limit on the pressure coefficient; that is, to obtain a critical Mach number of 0.8 the minimum C_{P0} must be no less than -0.24 (as shown in Figure 1.5). However, to ensure that at least some turret configurations would meet the constraint, for this investigation, the constraint on minimum C_{P0} was relaxed to -0.5 (i.e. $M_{crit} = 0.7$). Geometric constraints on the reference points of the fence were also imposed to avoid fence shapes that would lie on the optical aperture of the turret. For this constraint, all points on the fence must have a y-coordinate that is greater than or equal to 0.17*D* away from the centerline of the pod (again, assuming a typical turret configuration with an aperture diameter that is 1/3rd the diameter of the turret). Other constraints included an upper limit on the y-coordinates of the fence of 0.45*D,* and x-coordinates between 0 and *D*. Finally, the fence thickness was set to 0.03*D*. In summary, these constraints can be formulated as:

$$\sqrt{(x_i - 0.5)^2 + y_i^2} \leq 0.45 \quad \text{for i = 1, 2, 3,} \tag{C.3}$$

$$0 \leq x_i \leq 1 \quad \text{for i = 1, 2, 3, and} \tag{C.4}$$

$$0.17 \leq y_i \leq 0.45 \quad \text{for i = 1, 2, 3.} \tag{C.5}$$

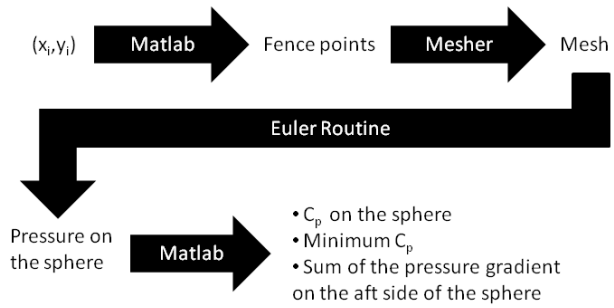

Figure C.2. Flow chart showing the optimization function call (Crahan 2010).

A further constraint on the design is to make sure that no point overlaps or gets too close to another point, e.g. point 2 must be located further downstream than point 1. This preliminary study did not restrict the curvature ratio of the fence, discussed in the Chapter 4, in order to look at the complete design space. In the optimization routine, described in the Chapter 5, a restriction was placed on the curvature ratio.

C.4 Methodology for Design Optimization

A flow chart of the function call is shown in Figure C.2. In general, the three points from Figure 5.2 that define the fence are selected and used to generate the fence coordinates. Once the fence coordinates are determined, the CFD mesh is generated and solved by the CFD routine. The minimum C_{P0} on the sphere along with the pressure gradient on the rear of the turret are then evaluated.

C.5 Survey of Design Space

The results of this investigation are shown in Figure C.3. In Figure C.3a, the center and trailing-edge points of the virtual duct, points 2 and 3, were held constant at $(x_2, y_2) = (0.5, 0.31)$ and $(x_3, y_3) = (0.85, 0.17)$, while the leading-edge points x_1 and y_1 were varied from 0.1 to 0.4 and 0.17 to 0.27 respectively. The white line delineates the region, denoted as region "I", where the minimum C_{P0} is greater than -0.5, thus fulfilling the critical Mach number constraint for the problem. Figure C.3a shows that the location of the leading edge of the virtual duct has a moderate influence on the objective function (i.e. the rear pressure gradient). More significantly, the small extent of the region "I" in Figure C.3a shows that there is only a limited range of positions for the front fence point that will satisfy the constraint on C_{P0}. It should be noted, however, that Figure C.3a shows the feasible range of the point 1 for only one selection of the points 2 and 3, and that a larger feasible range for point 1 would likely result from different values of the other fence points. Despite this limitation, Figure C.3a still gives insight into the kind of fence shape that would improve the performance of the virtual duct. For example, the fact that the feasible range for point 1 shown in Figure C.3a occurs at small values of *y/D* gives an indication of how much the fence must diffuse from point 1 to point 2 in order to maintain the C_{P0} at point 2 within the -0.5 constraint.

Figure C.3b illustrates the effect that the location of the middle fence point (point 2 in Figure 5.2) has on the objective function. In this case (x_1, y_1, x_3, y_3) were held constant at (0.25, 0.25, 0.85, 0.17) while x_2 and y_2 were varied from 0.37 to 0.69 and 0.28 to 0.44 respectively. Figure C.3b shows that the feasible range for point 2 is

significantly larger than for point 1. This result can be explained in that, for the selected locations of the points 1 and 3, there is a wide range of locations for the point 2 that will satisfy the critical Mach number criterion. In this case, the optimum location for the point 2 would be determined primarily by the minimum pressure-gradient; from Figure C.3b, this appears to occur at approximately $(x_2, y_2) = (0.5, 0.38)$.

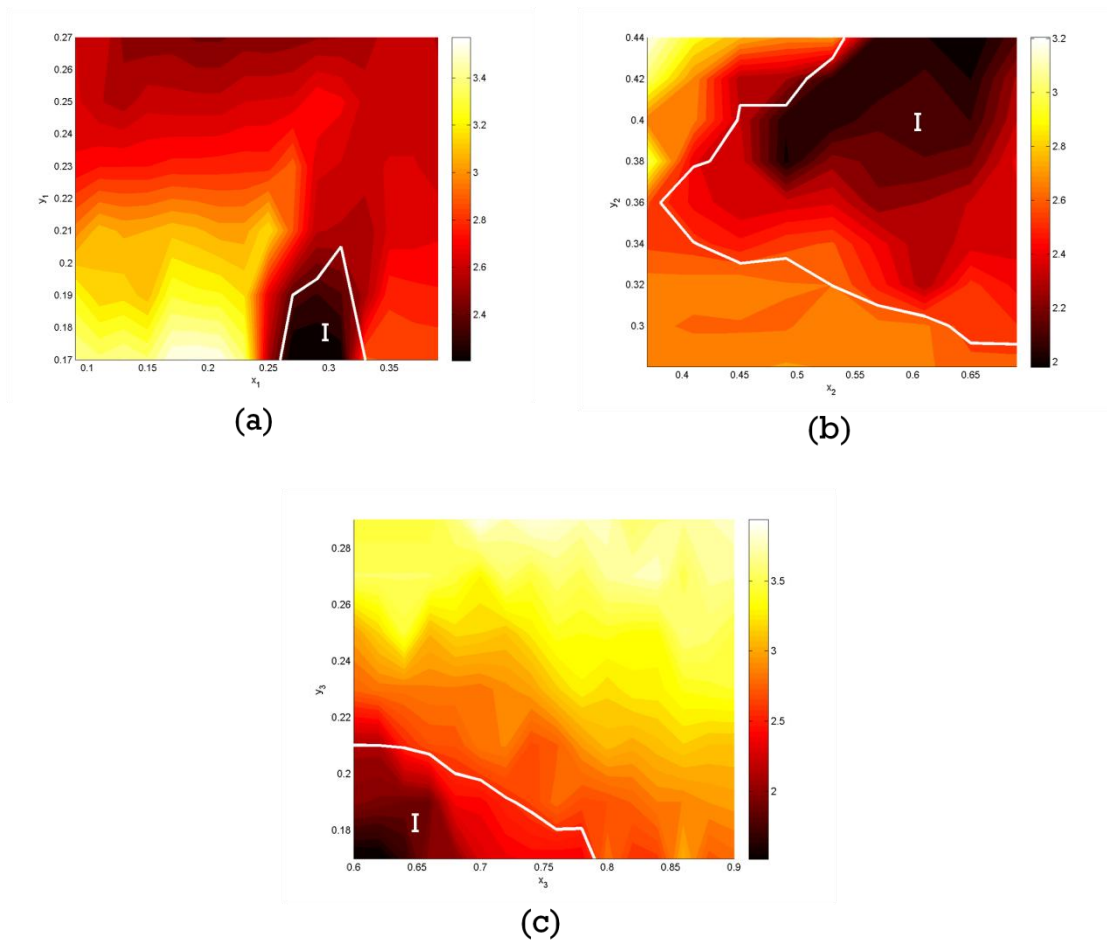

Figure C.3. Contour plots of the pressure gradient for different fence shapes on a turret by changing (a) x_1 and y_1, (b) x_2 and y_2, or (c) x_3 and y_3 with the unchanging fence points (x_1, y_1, x_2, y_2, x_3, y_3) being set at (0.25, 0.25, 0.5, 0.31, 0.85, 0.17). The region donated with the roman numeral "I" is the region of the design space where the minimum critical mach number is greater than 0.7 (Crahan 2010).

Figure C.3c illustrates the effect that the location of the trailing-edge point (point 3 in Figure 5.2) has on the pressure gradient. In this case (x_1, y_1, x_2, y_2) were held constant at (0.25, 0.25, 0.5, 0.31) while x_3 and y_3 were varied from 0.6 to 0.9 and 0.17 to 0.29 respectively. Figure C.3c shows that the location of point 3 has the strongest influence on the rear pressure gradient; this result makes sense if it is recognized that point 3 determines the amount of flow contraction at the rear of the fence. The small feasible range, located at small values of y, shows that the critical Mach number criterion is also better satisfied when the point 3 is inboard of the fence point 2. Figure C.3c indicates that the optimum location of the point 3 is in the vicinity of (x_3,y_3)= (0.6, 0.17).

C.6 Summary of Preliminary Study of Design Space

In summary, the examination of the pressure gradient over the feasible range of the points 1 to 3 (i.e. the design space) gives insight into the way in which the performance of the virtual duct is affected by basic design parameters. This section also shows the kinds of investigations that are necessary to improve the performance of the optimization approach.

BIBLIOGRAPHY

Achenbach, E., "Experiments on the Flow Past Spheres at Very high Reynolds Numbers," *J Fluid Mech.* (1972) 54: 565-575.

Anderson, J., *Modern Compressible Flow*, 3rd Edition, McGraw Hill, 2003.

Bagai, A., and Leishman, G.J., "Flow visualization of compressible vortex structures using density gradient techniques," (1993) 15:431-442.

Blanckaert, K., and Graf, W., "Outer-bank cell of secondary circulation and boundary shear stress in open-channel bends," Proc., 1st River, Coastal, and Estuarine Morphodynamics (RCEM), Univ. of Genova 1 (1999): 533-543.

Blanckaert, K., and De Vriend, H., "Secondary Flow in Sharp Open-Channel Bends," J Fluid Mechanics 498: 353-380 (2004).

Booij, Robert. "Measurements and large eddy simulations of the flows in some curved flumes." *J. Turbuence* (2003), 4(8): 1-17.

Buckner, A., Gordeyev, S. and Jumper, E.J., "Optical Aberrations Caused by Transonic Attached Boundary Layers: Underlying Flow Structure," AIAA Paper 2005-0752, Jan, 2005

Carroll, D., "Overview of High Energy Lasers: Past, Present, and Future?," AIAA 2011-3102, June 2011.

Cauchy, A., "Méthode générale pour la résolution des systemes d'équations simultanées," Comp. Rend. Sci. Paris (1847) 25: 536-538.

Cavalieri, D., Wittich, D., Gordeyev, S., Cheung, K., and Jumper, E. "Aero-optical Measurements using a High-Bandwidth Two-Dimensional Wavefront Sensor Array," J Directed Energy (2007), 2(4): 285-296.

Constantinescu, G., Koken, M., and Zeng, J., "The structure of turbulent flow in an open channel bend of strong curvature with deformed bed: Insight provided by detached eddy simulation," Water Resources Research (2011) 47 (5).

Crahan, G., Rennie, R. M., Jumper, E. J., Tovar, A., Mejia-Rodriguez, G., and Renaud, J. E., “Optimum Design of an Aircraft-Mounted Pod for Improved Aero-Optic Performance,” AIAA Paper 2010-9197, Sep. 2010.

Crahan, G., Rennie, R.M., and Jumper, E.J., “Experimental Measurements of an Aircraft-Mounted Pod Concept for Improved Aero-Optic Performance,” AIAA Paper 2011-1329, Jan. 2011.

Davidon, W., "Variable metric method for minimization," SIAM Journal on Optimization (1991) 1 (1): 1-17.

De Lucca, N., Gordeyev, S., and Jumper, E., "Comparison of Aero-Optical Measurements from the Flight Test of Full and Hemispherical Turrets on the AAOL," AIAA 2012-2985.

Duffin, D, “Feedforward Adaptive-Optic Correction of a Weakly Compressible High Subsonic Shear Layer,” Ph.D. Dissertation, Dept Aero and Mech Eng, Univ Notre Dame, Notre Dame, IN, 2009.

Duffner, R. W., *Airborne Laser, Bullets of Light*, Plenum Press, New York, 1997.

Fitzgerald, E., and Jumper, E., “The Optical Distortion Mechanism in a nearly incompressible free shear layer,” *J Fluid Mech* (2004) 512: 153-189.

Fletcher, R., and Powell, M., "A rapidly convergent descent method for minimization," The Computer Journal (1963) 6 (2): 163-168.

Forden, G., "Ballistic Missile Defense: The Airborne Laser," IEEE Spectrum, Sept 1997 (p. 40-49)

Gano, S., Renuad, J., and Sanders, B., “Variable fidelity optimization using a kriging based scaling function,” In *Proceedings of the 10th AIAA/ISSMO Multidisciplinary Analysis & Optimization Conference*, AIAA Paper 2004-4460, August 2004.

Gilbert, K., Otten, L., and Rose, W., Atmospheric propagation of radiation in the infrared spectrum. *The Infrared & Electro-Optical Handbook*, 1993.

Gordeyev, S. and Jumper, E.J., “Aero-Optical Characteristics of Compressiblle, Subsonic Turbulent Boundary Layers,” AIAA Paper 2003-3606, June, 2003.

Gordeyev, S. and Jumper, E.J., “Fluid dynamics and aero-optics of turrets,” *Prog Aero Sci* (2010) 46: 388-400.

Gordeyev, S., Cress, J., and Jumper, E.J., “Far-Field Laser Intensity Drop-Outs Caused by Turbulent Boundary Layers,” J Directed Energy (2011).

Gordeyev, S., Jumper, E., and Hayden, T., "Aero-optical effects of supersonic boundary layers." *AIAA Journal* 50 (3) (2012).

Gordeyev, S., Personal Communication, February 11, 2014.

Hille, P., Vehrenkamp, R., and SchulzDubois, E., "The development and structure of primary and secondary flow in a curved square duct," J Fluid Mechanics (1985) 151: 219-241.

Hugo, R., Jumper, E., Havener, G., and Stepanek, C., "Time-resolved wave front measurements through a compressible free shear layer," AIAA Journal (1997) 35: 671-677.

Jumper, E.J. and Fitzgerald, E. J., "Recent Advances in Aero-Optics." *Progress in Aerospace Sciences*, Vol. 37, 2001, pp. 299-339.

Karman, T., "Compressibilty Effects in Aerodynamics," J of Aeronautical Sciences (1941) Vol. 8, No 9, p.337-356.

Kashyap, S., Constantinescu, G., Rennie, C., Post, G., and Townsend, R., "Influence of Channel Aspect Ratio and Curvature on Flow, Secondary Circulation, and Bed Shear Stress in a Rectangular Channel Bend," J Hydraulic Engineering 138: 1045-1059 (2012).

Katz, J., and Plotkin, A., *Low-Speed Aerodynamics,* 1st Edition, McGraw-Hill, 1991.

Klein, M.V., *Optics*, 1st Edition, Wiley, New York, 1970.

Ladd, J., Mani, M., and Bower, W., "Validation of aerodynamic and optical computations for the flow about a cylindrical/hemispherical turret," AIAA Paper 2009-4118.

Lundstedt, T., Seifert, E., Abramo, L., Thelin, B., Nyström, A., Pettersen, J., and Bergman, R., "Experimental Design and Optimization," Chemometrics and Intelligent Laboratory Systems (1998) 42: 3-40.

Maskell, E. C., "A Theory of the Blockage Effects on Bluff Bodies and Stalled Wings in a Closed Wind Tunnel," ARC R&M No. 3400, Nov. 1963.

Montgomery, D., *Design and Analysis of Experiments*, 7th Edition, John Wiley & Sons, 2009.

Morgan, P, and Visbal, M., "Numerical Simulations Investigating Control of Flow over a Turret," AIAA 2009-574, Jan 2009.

Nightingale, A., Gordeyev, S., Jumper, E., Goodwine, B., and Siegenthaler, J., "Regularized Shear Layer for Adaptive Optics Control Applications," AIAA 2005-4774, June 2005.

Nightingale, A., Gordeyev, S., and Jumper, E., "Optical Characterization of a Simulated Weakly Compressible Shear Layer: Unforced and Forced," AIAA Journal (2009) 47 (10): 2298-2305.

Nocedal, J. and Wright, S., *Numerical Optimization*, 2nd Edition, Springer, 2006.

Porter, C., Rennie, M., and Jumper, E., "Aero-Optic Effects of a Wing Tip Vortex," AIAA 2010-435, Jan 2010.

Porter, C., Gordevev, S., Zenk, M., and Jumper, E., "Flight Measurements of Aero-Optical Distortions from a Flat-Windowed Turret on the Airborne Aero-Optics Laboratory (AAOL)," AIAA 2011-3280, June 2011a.

Porter, C., "The Optical Environment From the Tip Vortices of a Helicopter in Different Flight Regimes," Ph.D. Dissertation, Dept of Aero and Mech Eng, Univ of Notre Dame, Notre Dame, IN, 2011b.

Rennie, R.M., Duffin, D.A., and Jumper, E.J., “Characterization and aero-optic correction of a forced two-dimensional, weakly compressible subsonic shear layer,” *AIAA Journal* (2008) 46: 2787-2795.

Rennie, R. M., Crahan, G., and Jumper, E. J., “Aerodynamic Design of an Aircraft-Mounted Pod for Improved Aero-Optic Performance,” AIAA Paper 2010-0437, Jan. 2010.

Rennie, R.M., Goorskey, D., Whiteley, M.R., Cavalieri, D., and Jumper, E.J., “Evaluation of Laser Beacon for Adaptive-Optic Correction of a Compressible Shear Layer,” Accepted for publication in *AIAA Journal*, June 2012.

Roggemann, M., and Welsh, B., *Imaging through Turbulence*, CRC Press, 1996.

Ross, T., "Limitations and Applicability of the Marechal Approximation," Applied Optics (2009) 48 (10): 1812-1818.

Rozovski, I., “Flow of Water in Bends of Open Channels,” Program for Sci. Transl. Jerusalem (1957).

Saric, W.S., and Reshotko, E., “Review of Flow Quality Issues in Wind Tunnel Testing,” AIAA Paper 1998-2613, June, 1998.

Schlichting, H., *Boundary-layer Theory*. New York: McGraw-Hill 7th Edition (1979).

Settles, G.S., *Schlieren and Shadowgraph Techniques*, 1st Edition, 2nd Printing(corrected), Springer, 2001.

Shapiro, A., *The Dynamics and Thermodynamics of Compressible Fluid Flow*, John Wiley & Sons, Vol 1, 1953.

Siegenthaler, J., Jumper, E., and Gordeyev, S., "Atmospheric Propagation Vs. Aero-Optics," AIAA 2008-1076, Jan. 2008.

Smith, A., "Evaluation of Passive Boundary Layer Flow Control Techniques for Aero-Optic Mitigation," Ph.D. Prospectus, Dept of Aero and Mech Eng, Univ of Notre Dame, Notre Dame, IN, 2013.

Stoesser, T., Ruether, N.,and Olsen, N., "Calculation of primary and secondary flow and boundary shear stresses in a meandering channel," Advances in Water Resources (2010) 33 (2): 158-170.

Strang, W.Z., Tomaro, R.F., and Grismer, M.J., "The Defining Methods of $Cobalt_{60}$: A Parallel, Implicit, Unstructured Euler/Navier-Stokes Flow Solver," AIAA Paper 1999-0786, Jan. 1999.

Stratford, B., "Prediction of separation of the turbulent boundary layer," *J Fluid Mech* (1959) 5:1-16.

Thomson, W., "On the Origin of Windings of Rivers in Alluvial Plains, with Remarks on the Flow of Water Round Bends in Pipes," Proc. R. Soc. London 25: 5-8 (1876).

Tovar, A. and Renaud, J., *Optimum Design of Mechanical Elements: Class notes for AME60661*, University of Notre Dame, 2010.

Tsien, H., "Two-Dimensional Subsonic Flow of Compressible Fluids," J of Aeronautical Sciences (1939) Vol. 6, No 10, p.399-407.

Tutkun, M., Johansson, P., and Reif, B., "Visualization and Measurement of Flow over a Cylindrical Surface with a Bump," AIAA Journal, 45 (7), July 2007.

Tyson, R.K., *Principles of Adaptive Optics*, Academic Press, Inc., San Diego, 1991.

Tyson, R.K., *Adaptive Optics Engineering Handbook*, Marcel Dekker, Inc., New York, 2000.

Van Balen, W., Uijttewaal, W., and Blanckaert, K., "Large-Eddy Simulation of a Mildly Curved Open-Channel Flow," J. Fluid mech (2009) vol 630, 413-442.

Van Balen, W., "Curved Open-Channel Flows: A Numerical Study," Ph.D. Dissertation, Delft University of technology, Delft, Netherlands (2010).

White, F.M., *Fluid Mechanics, 3rd Ed*., McGraw-Hill, New York, 1994.

Wolfe, P., "Convergence conditions for ascent methods," Siam Review (1969) 11 (2): 226-235.